



HAL
open science

A sensitive survey for ^{13}CO , CN, H_2CO and SO in the disks of T Tauri and Herbig Ae stars

S. Guilloteau, E. Di Folco, Anne Dutrey, M. Simon, N. Grosso, V. Piétu

► **To cite this version:**

S. Guilloteau, E. Di Folco, Anne Dutrey, M. Simon, N. Grosso, et al.. A sensitive survey for ^{13}CO , CN, H_2CO and SO in the disks of T Tauri and Herbig Ae stars. *Astronomy and Astrophysics - A&A*, 2013, 549, pp.id.A92. 10.1051/0004-6361/201220298 . hal-00804432

HAL Id: hal-00804432

<https://hal.science/hal-00804432v1>

Submitted on 24 Jul 2023

HAL is a multi-disciplinary open access archive for the deposit and dissemination of scientific research documents, whether they are published or not. The documents may come from teaching and research institutions in France or abroad, or from public or private research centers.

L'archive ouverte pluridisciplinaire **HAL**, est destinée au dépôt et à la diffusion de documents scientifiques de niveau recherche, publiés ou non, émanant des établissements d'enseignement et de recherche français ou étrangers, des laboratoires publics ou privés.

A sensitive survey for ^{13}CO , CN, H_2CO , and SO in the disks of T Tauri and Herbig Ae stars^{★,★★}

S. Guilloteau^{1,2}, E. Di Folco^{1,2}, A. Dutrey^{1,2}, M. Simon³, N. Grosso⁴, and V. Piétu⁵

¹ Univ. Bordeaux, LAB, UMR 5804, 33270 Floirac, France

² CNRS, LAB, UMR 5804, 33270 Floirac, France

e-mail: [guilloteau; difolco; dutrey]@obs.u-bordeaux1.fr

³ Department of Physics and Astronomy, Stony Brook University, Stony Brook, NY 11794-3800, USA

⁴ Observatoire Astronomique de Strasbourg, Université de Strasbourg, CNRS, UMR 7550, 11 rue de l'Université, 67000 Strasbourg, France

⁵ IRAM, 300 rue de la piscine, 38406 Saint Martin d'Hères, France

Received 28 August 2012 / Accepted 8 November 2012

ABSTRACT

Aims. We investigate the suitability of several molecular tracers, in particular CN $N = 2-1$ line emission, as a confusion-free probe of the kinematics of circumstellar disks.

Methods. We use the IRAM 30-m telescope to perform a sensitive search for CN $N = 2-1$ in 42 T Tauri or Herbig Ae systems located principally in the Taurus-Auriga region. ^{13}CO $J = 2-1$ is observed simultaneously to provide an indication of the level of confusion with the surrounding molecular cloud. The bandpass also contains two transitions of ortho- H_2CO , one of SO and the C^{17}O $J = 2-1$ line which provide complementary information on the nature of the emission.

Results. While ^{13}CO is in general dominated by residual emission from the cloud, CN exhibits a high disk detection rate $>50\%$ in our sample. We even report CN detection in stars for which interferometric searches failed to detect ^{12}CO , presumably because of obscuration by a foreground, optically thick, cloud. Comparison between CN and o- H_2CO or SO line profiles and intensities divide the sample in two main categories. Sources with SO emission are bright and have strong H_2CO emission, leading in general to $[\text{H}_2\text{CO}/\text{CN}] > 0.5$. Furthermore, their line profiles, combined with a priori information on the objects, suggest that the emission is coming from outflows or envelopes rather than from a circumstellar disk. On the other hand, most sources have $[\text{H}_2\text{CO}/\text{CN}] < 0.3$, no SO emission, and some of them exhibit clear double-peaked profiles characteristics of rotating disks. In this second category, CN is likely tracing the proto-planetary disks. From the line flux and opacity derived from the hyperfine ratios, we constrain the outer radii of the disks, which range from 300 to 600 AU. The overall gas disk detection rate (including all molecular tracers) is $\sim 68\%$, and decreases for fainter continuum sources.

Conclusions. The current study demonstrates that gas disks, like dust disks, are ubiquitous around young PMS stars in regions of isolated star formation, and that a large fraction of them have $R_{\text{out}} \geq 300$ AU. It also shows the potential of the CN $N = 2-1$ transition to probe the kinematics of these disks, thereby measuring the stellar mass, using high resolution observations with ALMA.

Key words. radio lines: planetary systems – stars: pre-main sequence – circumstellar matter – protoplanetary disks

1. Introduction

Masses of young stars are a fundamental property with impacts on theories of the stars' formation, calculations of their evolution to the main sequence, and the chronology of the planets that may be, or will be, associated with them. Dynamical techniques provide the only absolutely reliable measurements of mass. Because most binary orbits are at least a few years long, the quickest way to accomplish a dynamical measurement is by mapping the Keplerian rotation of the circumstellar disk of a young star (Guilloteau & Dutrey 1998; Simon et al. 2000). These early studies, and especially the more recent observations by Schaefer et al. (2009), were all carried out by mm-wave interferometry in the $J = 1-0$ and $J = 2-1$ transitions of ^{12}CO and revealed two limitations of the method. The first is intrinsic: Young stars with disks are generally located in molecular clouds whose

optically thick ^{12}CO emission may mask the disk emission of the star. The second limitation was technical: it was difficult to find young stars with masses smaller than $0.5 M_{\odot}$ that have detectable gaseous circumstellar disks. A possible solution to the first problem could be observation in the lines of ^{13}CO or C^{18}O because the optical depth of the molecular cloud would be less in these transitions than in ^{12}CO . However, the disk emission in the lines of the CO isotopologues would of course be less than that of the ^{12}CO lines. We judged that, at the time of our observations, the instrumentation available to us had insufficient sensitivity to obtain mass measurements to the required precision, $\leq 5\%$. The commissioning of the Atacama Large Millimeter/Submillimeter Array (ALMA) offers the promise to remove both obstacles to mass measurement of young low mass stars by mapping the rotation of their disks.

Our goal in this work is to assess the applicability of several molecular tracers for confusion-free and high sensitivity measurements of disk kinematics using ALMA. After ^{12}CO , the strongest lines in disks are the rotational transitions of ^{13}CO $J = 2-1$ or $3-2$, HCO^+ $J = 3-2$ and the hyperfine split lines of CN $N = 2-1$ (Dutrey et al. 1997; Öberg et al. 2010).

* Based on observations carried out with the IRAM 30-m telescope. IRAM is supported by INSU/CNRS (France), MPG (Germany) and IGN (Spain).

** Appendices are available in electronic form at <http://www.aanda.org>

However, ^{13}CO line emission can also be affected by confusion (e.g. Dutrey et al. 2003, for BP Tau). The situation is less clear for $\text{HCO}^+ J = 3-2$, but this transition can still have substantial optical depth and be excited in clouds (see for example CW Tau in Salter et al. 2011); furthermore, its relatively high frequency requires better observing conditions. Other previous searches for molecular tracers in disks were conducted with the single-dishes (principally the IRAM 30-m and JCMT) or mm/sub-mm arrays (IRAM PdBI, SMA and CARMA). The former were limited in sensitivity (e.g. Salter et al. 2011, for a study of CN $N = 2-1$ and $\text{HCO}^+ J = 3-2$), while, because of the need for sufficient UV coverage, the latter could only observe a few stars (e.g. Öberg et al. 2010).

Recent advances in receiver and back-end technology at the IRAM 30-m telescope encouraged us to carry out a new assessment of molecular line tracers in circumstellar disks, particularly the CN $N = 2-1$ line hyperfine split lines. We report here our systematic search for CN $N = 2-1$ emission in 40 young stars located in the Taurus/Auriga star forming region (SFR). Together with previous observations, 46 stars in this SFR have now been observed with high sensitivity in this transition, a gain of a factor almost four in sample size. Section 2 describes our sample, the observations, and their analysis. Section 3 presents our results for the CO isotopologues, CN, H_2CO , and SO molecules. Section 4 discusses our assessment of CN as a disk tracer and comments on stars with outflows and on general properties of the observed line emission. Section 5 summarizes our results. An Appendix shows all the observed spectra and provides details for many of the stars.

2. Observations and data analysis

2.1. Source sample

We focus here principally on the Taurus Aurigae region, to which we add CB26, an embedded source in an isolated Bok globule, and HD 163296, an isolated HAe star. Our study is thus only relevant to regions of isolated star formation. Table 1 lists the stars involved in this study; the 40 stars observed anew at the IRAM 30-m radiotelescope appear without specific symbols. This sub-sample was observed in a homogeneous way. It is completed by observations on a few sources (marked by specific symbols in the Table) obtained independently, also with the IRAM 30-m. ^{13}CO , CN and the ortho- H_2CO $3_{13}-2_{12}$ transitions were observed towards the Herbig Ae star HD 163296, together with the SO 6_5-5_4 line. Data from DM Tau is from Dutrey et al. (1997). The intensity reported for LkCa 15 is from a noisy IRAM 30-m spectrum, but is consistent with the interferometric data of Chapillon et al. (2012). CI Tau, CY Tau and GO Tau were detected with the IRAM 30-m, and later imaged at the IRAM Plateau de Bure array (Guilloteau et al., in prep.). The overall sample covers a wide range of spectral types (from M5.5 to A0, taken from Luhman et al. 2010), luminosities (0.2 to $45 L_\odot$), and 1.3 mm continuum flux densities (from <4 to ~ 800 mJy), but is not complete with respect to these quantities. No specific account about extinction and location with respect to molecular clouds was made when selecting sources. Sources with outflows were deliberately included. The epoch 2000 coordinates are from interferometric mm continuum images (Guilloteau et al. 2011) when available, or SIMBAD otherwise.

2.2. Observations

Most observations were carried out with the IRAM 30-m telescope from Dec. 4 to Dec. 8 2011, under excellent weather

conditions (precipitable water vapor content below 1 mm). A few additional sources were observed on the afternoon of May 1st, 2012 using the same instrumental setup. The weather was good (water vapor content about 3 mm), but a few clouds occasionally produced anomalous refraction. The absolute calibration of this second set is thus more uncertain.

The dual-polarization, sideband separating receivers were tuned to cover approximately 7.8 GHz of bandwidth around 224.3 GHz in the upper sideband (USB) and 208.7 GHz in the lower sideband (LSB). The 8 units of the FTS back-end (each of them being made of 3 adjacent sub-units) covered more precisely 4 frequency ranges (with 2 polarization each) at [220.325, 224.365] and [224.055, 228.105] GHz in USB, and [204.655, 208.695] and [208.375, 212.425] GHz in LSB. The back-end provides a spectral resolution of 195 kHz, which translates into $0.25-0.28 \text{ km s}^{-1}$ in this frequency range. The spectral setup includes several lines (listed in Table 2) which can be relevant for disks, in particular all 19 hyperfine components of CN $N = 2-1$. The sideband separating mixers provide a mean rejection around 13 dB. However, the presence of strong lines spread over the band indicate some variation across the band. A fortunate case is the SO (5_4-4_3) transition at 206.176062 GHz, which appears at 226.572 GHz in the image sideband and permits a control of the rejection near the CN $N = 2-1$ lines, whose strongest hyperfine components are at 226.874 and 226.657 GHz. Single sideband system temperatures were in the range 170–190 K in December, and 170–250 K in May.

In December 2011, the exceptionally dry weather and clear sky produced rapid cooling a few hours after sunset, which could not be compensated by the thermal regulation of the telescope, and resulted in significant pointing changes. This also presumably affected the telescope efficiency. In May, anomalous refraction clearly occurred occasionally. As a result, the absolute calibration is in general accurate to 10–15% but on several sources is not better more than about 25%. However, since we control the receiver sideband rejection, the relative intensities of the detected lines are expected to be accurate to within 5% or better, noise being in general a more severe limitation. Given the absolute calibration issues, we did not correct for the elevation dependent antenna gain, and simply use a uniform conversion factor from antenna temperature (T_A^*) to flux density of 9 Jy/K.

Since our targets should be unresolved by the IRAM 30-m, the observations were performed in symmetric wobbler switching mode, with the two references $\pm 60''$ away at the same elevation. Together with the stable weather in December, this mode provided flat baselines, allowing clear detection of the continuum emission from the dust in most sources. Occasional baseline discontinuities between the 3 sub-units (“platforming”) were visible in the spectra, but none of the spectral lines we searched for were affected by this problem.

We observed the sample of 40 sources (see Table 1), for about 1 h each. For a typical linewidth of 2.6 km s^{-1} (2 MHz), representative of our sources, this gives a detection sensitivity of $0.08 \text{ Jy km s}^{-1}$ (1σ) on the integrated line flux.

2.3. Data analysis

We removed linear baselines in a window $\pm 60 \text{ km s}^{-1}$ wide around each spectral line. Spectra for all objects appear in Appendix B. Figures 1 and 2 show spectra for two objects: Haro 6–10 which exhibits bright lines in all molecules, and MWC 480, an isolated HAe star for which CN has already been imaged with the IRAM array (Chapillon et al. 2012), included

Table 1. Source sample.

Name	RA J2000.0	Dec J2000.0	Spectral type	L_* L_{\odot}	$S_{\nu}(1.3 \text{ mm})$ (mJy)	Incl. ($^{\circ}$)	A_V	References
FN Tau	04:14:14.59	28:27:58.1	M5	0.50	<18		1.35	a, A
CW Tau	04:14:17.0	28:10:56.51	K3	0.68	96		2.19	b,B
CIDA-1	04:14:17.6	28:06:11	M5.5		14		–	a, α
CY Tau (*)	04:17:33.729	28:20:46.86	M1.5	0.40	111	28 \pm 5	0.1	c, 1, B
BP Tau	04:19:15.834	29:06:26.98	K7	0.65	58	33 \pm 6	0.49	c, 1, B
DE Tau	04:21:55.6	27:55:05.55	M1	1.14	36		1.56	b,C, β
RY Tau	04:21:57.42	28:26:35.6	K1	6.59	229	66 \pm 3	1.84	b, 2, B
T Tau	04:21:59.435	19:32:06.36	K0	8.91	200	30	1.39	c, 3, C
Haro 6-5B	04:22:01.00	26:57:35.5	K5	0.05	134	80	9.96	d, 4, D, β
FT Tau	04:23:39.188	24:56:14.28	C	0.38	73	23 \pm 5		c, 1, C
DG Tau-B	04:27:02.56	26:05:30.4	C	>0.02	531	64 \pm 2		c, 1
DG Tau	04:27:04.67	26:06:16.9	K6	3.62	390	38 \pm 2	3.32	c, 1, D, β
Haro 6-10	04:29:23.729	24:33:01.52	K5	2.55	44			c, E
IQ Tau	04:29:51.56	26:06:44.9	M0.5	0.53	60		1.25	a, B
LkHa 358	04:31:36.15	18:13:43.1	K8	0.09	17	28 \pm 9	0.13	a, 5, A, γ
HH 30	04:31:37.468	18:12:24.21	M0	0.2–0.9	20	83 \pm 2	2.96	c, 6, F, β
HL Tau	04:31:38.413	18:13:57.55	K7	1.53	819	45 \pm 1	7.43	c, 1, D, β
HK Tau	04:31:50.58	24:24:17.9	M0.5	1.00	41	~90	3.41	b, 7, B
Haro 6-13	04:32:15.419	24:28:59.47	M0	2.11	114	40 \pm 3	11.9	c, 5, A, β
GG Tau	04:32:30.34	17:31:40.5	K7	0.64	593	37 \pm 1	0.76	b, 8, B
UZ Tau E	04:32:43.071	25:52:31.07	M1	0.9–1.6	150	56 \pm 2	1.49	c, 1, C+G
04302+2247	04:33:16.2	22:53:20.0	–		130	88 \pm 2		e, 9
DL Tau	04:33:39.077	25:20:38.10	K7	1.16	204	43 \pm 3	2.0	c, 1, H
DM Tau (\$)	04:33:48.70	18:10:10.6	M1	0.16	109	35 \pm 1	0.31	c, 1, B, α
CI Tau (*)	04:33:52.014	22:50:30.06	K7	0.96	125	44 \pm 3	1.77	c, 1, B
AA Tau	04:34:55.42	24:28:53.1	K7	0.66	73	70 \pm 5	0.49	b, 10, C
DN Tau	04:35:27.38	24:14:58.9	M0	0.68	89		1.89	a, D, β
DO Tau	04:38:28.59	26:10:49.5	M0	1.29	136		2.64	b, B
HV Tau C	04:38:35.31	26:10:38.5	K6	0.60	40	~90	2.42	b, 11, B
LkCa 15 (*)	04:39:17.76	22:21:03.7	K5	0.85	110	52 \pm 1	0.62	c, 1, B
Haro 6-33	04:41:38.827	25:56:26.68	M0	0.76	34	52 \pm 5	10.2	c, 5, D
GO Tau (*)	04:43:03.050	25:20:18.80	M0	0.22	53	52 \pm 1	1.18	a, 5, B
DQ Tau	04:46:53.064	17:00:00.09	M0	0.91	83		0.97	c, C
DR Tau	04:47:06.22	16:58:42.8	K5	1.97	159		2.0	b, B
DS Tau	04:47:48.6	29:25:10.96	K5	0.67	25		0.31	b, C
UY Aur	04:51:47.37	30:47:13.9	M0	1.41	29	42	2.05	b, 12, B
GM Aur (*)	04:55:10.98	30:21:59.5	K7	1.23	176	50 \pm 1	0.14	c, 1, B
AB Aur	04:55:45.80	30:33:04.0	B9	44.86	110	20-30	0.62	f, 13, I
SU Aur	04:55:59.4	30:34:01.39	G2	9.29	<30	62	0.90	b, 14, B
MWC 480	04:58:46.27	29:50:37.0	A2	11.50	289	37 \pm 1	0.25	c, 1, G, γ
VDA98 CB 26	04:59:50.74	52:04:43.8	–		190	~90		g, 15
CIDA-8	05:04:41.4	25:09:57	M3.5	0.26	8		0.83	a, A, α
CIDA-11	05:06:23.3	24:32:24	M3.5	0.22	<4		0.36	a, A
RW Aur	05:07:49.56	30:24:05.1	K3	1.72	42	45 \pm 5	0.32	b, 16, B
MWC 758	05:30:27.51	25:19:58.4	A3	11.00	55	21		c, 17, J
CQ Tau	05:35:58.485	24:44:54.19	A8/F2	12.00	162	29 \pm 2	0.96	c, 1, J, γ
HD 163296 (#)	17:56:21.31	-21:57:22.0	A1	37.70	670	45 \pm 4	0.25	h, K, γ

Notes. Data for sources marked with (*) are for CN only, and were obtained separately, (\$) no SO line, (#) different SO line. Flux references: (a) Schaefer et al. (2009); (b) Andrews & Williams (2005); (c) Guilloteau et al. (2011); (d) Osterloh & Beckwith (1995); (e) Graeffe et al. 2012; (f) Piétu et al. (2005); (g) Launhardt et al. (2009); (h) Qi et al. (2011). Inclination references: (1) Guilloteau et al. (2011); (2) Isella et al. (2010b); (3) Ratzka et al. (2009), (4) Krist et al. (1998); (5) Schaefer et al. (2009); (6) Pety et al. (2006); (7) McCabe et al. (2011); (8) Guilloteau et al. (1999); (9) Graeffe et al. (2012); (10) Bouvier et al. (1999); (11) Duchêne et al. (2010); (12) Duvert et al. (1998); (13) Piétu et al. (2005); (14) Akeson et al. (2002); (15) Launhardt et al. (2009); (16) Cabrit et al. (2006); (17) Isella et al. (2010a); (18) Isella et al. (2007). Luminosity references: (A) Schaefer et al. (2009); (B) Bertout et al. (2007); (C) Kenyon & Hartmann (1995); (D) White & Hillenbrand (2004); (E) Prato et al. (2009); (F) Pety et al. (2006); (G) Simon et al. (2000); (H) White & Ghez (2001); (I) Hernández et al. (2004); (J) Chapillon et al. (2008); (K) Tilling et al. (2012). Extinction references: Kenyon & Hartmann (1995), except (α) Briceño et al. (2002) (A_J for CIDA-8), (β) White & Hillenbrand (2004), (γ) van den Ancker et al. (1998).

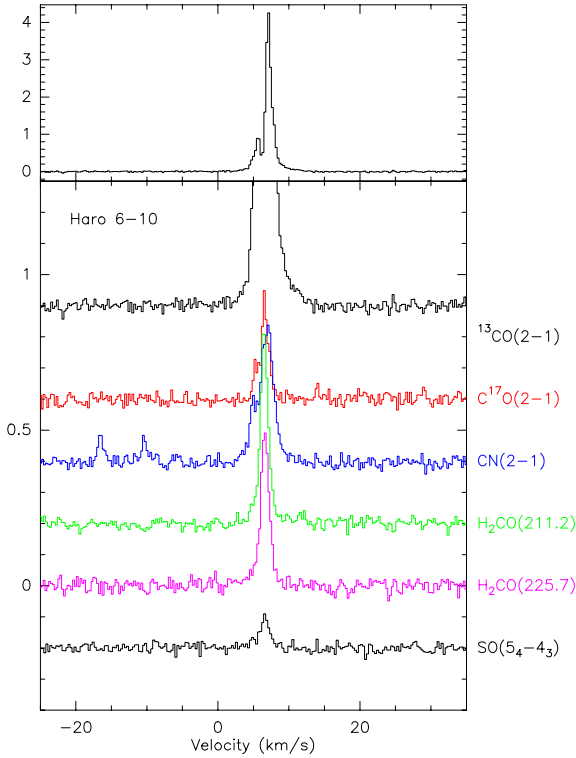


Fig. 1. Spectra of the observed transitions towards Haro 6-10. *Top panel:* $^{13}\text{CO } J = 2-1$ spectrum. *Bottom panels,* from top to bottom: spectra of $^{13}\text{CO } J = 2-1$, $\text{C}^{17}\text{O } J = 2-1$, $\text{CN } N = 2-1$, ortho $\text{H}_2\text{CO } 3_{13}-2_{12}$, ortho $\text{H}_2\text{CO } 3_{12}-2_{11}$, and $\text{SO } 5_4-4_3$ presented on a common scale. The Y axis scale is antenna temperature, T_A^* (the conversion factor to flux density is 9 Jy/K).

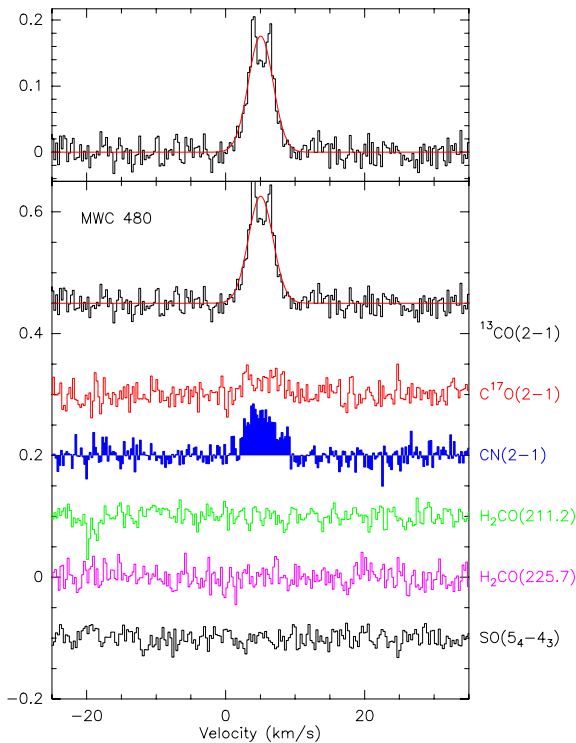


Fig. 2. As Fig. 1 but towards MWC 480. The red curve is a simple Gaussian fit to the disk emission in $^{13}\text{CO } J = 2-1$.

in our sample as a reference object. To derive line intensities, we fitted simple Gaussian profiles to the observed lines taking

Table 2. Frequencies of transitions.

Frequency (MHz)	Molecule and transition	Detection
206 176.062	$\text{SO } (5_4-4_3)$	Yes
209 230.201	$\text{HC}_3\text{N } J = 23-22$	No
209 419.15	$^{13}\text{C}^{18}\text{O } J = 2-1$	cloud only
211 211.455	ortho $\text{H}_2\text{CO } 3_{13}-2_{12}$	Yes
220 398.688	$^{13}\text{CO } J = 2-1$	Yes
224 714.385	$\text{C}^{17}\text{O } J = 2-1$	Yes
225 697.781	ortho $\text{H}_2\text{CO } 3_{12}-2_{11}$	Yes
226 287.4185	$\text{CN } N = 2-1 \ J = 3/2-3/2, \ F = 1/2-1/2$	
226 298.9427	$\text{CN } N = 2-1 \ J = 3/2-3/2, \ F = 1/2-3/2$	
226 303.0372	$\text{CN } N = 2-1 \ J = 3/2-3/2, \ F = 3/2-1/2$	
226 314.5400	$\text{CN } N = 2-1 \ J = 3/2-3/2, \ F = 3/2-3/2$	Yes
226 332.4986	$\text{CN } N = 2-1 \ J = 3/2-3/2, \ F = 3/2-5/2$	
226 341.9298	$\text{CN } N = 2-1 \ J = 3/2-3/2, \ F = 5/2-3/2$	
226 359.8710	$\text{CN } N = 2-1 \ J = 3/2-3/2, \ F = 5/2-5/2$	Yes
226 616.5714	$\text{CN } N = 2-1 \ J = 3/2-1/2, \ F = 1/2-3/2$	Yes
226 632.1901	$\text{CN } N = 2-1 \ J = 3/2-1/2, \ F = 3/2-3/2$	Yes
226 659.5584	$\text{CN } N = 2-1 \ J = 3/2-1/2, \ F = 5/2-3/2$	Yes
226 663.6928	$\text{CN } N = 2-1 \ J = 3/2-1/2, \ F = 1/2-1/2$	Yes
226 679.3114	$\text{CN } N = 2-1 \ J = 3/2-1/2, \ F = 3/2-1/2$	Yes
226 874.1908	$\text{CN } N = 2-1 \ J = 5/2-3/2, \ F = 5/2-3/2$	Yes
226 874.7813	$\text{CN } N = 2-1 \ J = 5/2-3/2, \ F = 7/2-5/2$	Yes
226 875.8960	$\text{CN } N = 2-1 \ J = 5/2-3/2, \ F = 3/2-1/2$	Yes
226 887.4202	$\text{CN } N = 2-1 \ J = 5/2-3/2, \ F = 3/2-3/2$	Yes
226 892.1280	$\text{CN } N = 2-1 \ J = 5/2-3/2, \ F = 5/2-5/2$	Yes
226 905.3574	$\text{CN } N = 2-1 \ J = 5/2-3/2, \ F = 3/2-5/2$	
227 191.8195	$\text{CN } N = 2-1 \ J = 5/2-1/2, \ F = 5/2-3/2$	

Notes. $\text{CN } N = 2-1$ line frequencies were measured in laboratory by Skatrud et al. (1983); we use here the fitted values from the CDMS Database (Müller et al. 2001).

into account the hyperfine structure of the $\text{C}^{17}\text{O } J = 2-1$ and $\text{CN } N = 2-1$ lines. We used the ‘‘HFS (hyperfine structure)’’ method of the CLASS data analysis program in the GILDAS¹ package for this purpose. This method assumes a common excitation temperature for all the hyperfine components, a likely situation at the high densities appearing in disks. For a Gaussian line, the emerging profile is then

$$T_A^*(v) = \eta \left(J_v(T_{\text{ex}}) - J_v(T_{\text{bg}}) \right) \times \sum_i \left(1 - \exp \left(-R_i \tau \exp \left(- \left(\frac{v - V_{\text{sys}} - v_i}{\delta V} \right)^2 \right) \right) \right) \quad (1)$$

where R_i are the relative intensities ($\sum_i R_i = 1$), v_i the velocity of each hyperfine component with respect to a common reference frequency, and τ the total line opacity (sum over all hyperfine components, as the R_i are normalized). V_{sys} is the source velocity, δV the line width at 1/e, and η a beam filling factor. The HFS method uses $X = \eta \tau (J_v(T_{\text{ex}}) - J_v(T_{\text{bg}}))$, V_{sys} , δV and τ as free parameters. The difference in saturation between the various hyperfine components allows determination of τ provided sufficient signal to noise. For CN, although all 19 hyperfine transitions were used for the fitting, the quoted integrated line flux includes only the 3 blended hyperfine components around 226.874 GHz and the two weak components at 226 887.399 & 226 892.151 MHz (which appear near $V_{\text{LSR}} - 11$ and -17 km s^{-1} in the brighter sources)². Given the line ratios, the total line flux

¹ See <http://www.iram.fr/IRAMFR/GILDAS> for more information about GILDAS softwares.

² This is essentially the flux in the $J = 5/2-3/2$ fine structure line, as the only missing hyperfine component has much smaller intensity.

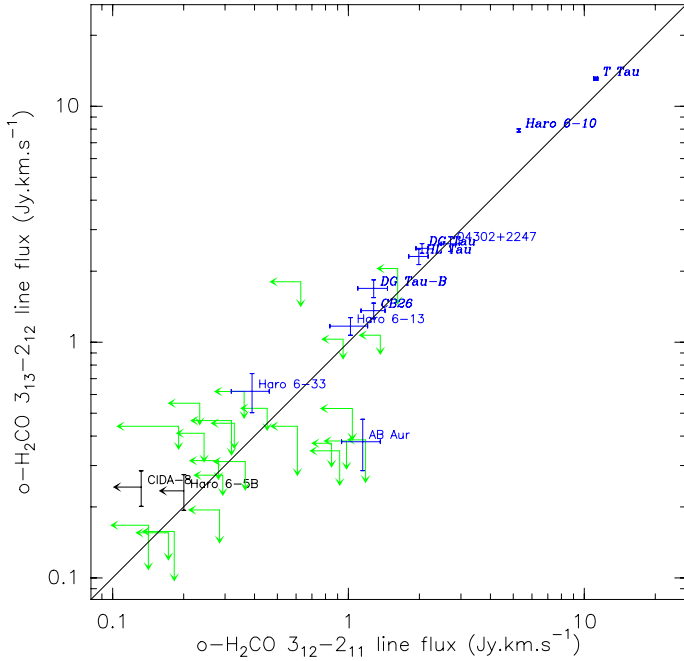


Fig. 3. Integrated line flux of the $3_{12}-2_{11}$ line of H_2CO vs that of the $3_{13}-2_{12}$ transition. Color codes indicate detected vs. non-detected lines: blue for detection of both lines, black for detection of the $3_{13}-2_{12}$ line, green for non-detections. The detection threshold is set at 4σ . For detected lines, the errorbars are 1σ . For non-detected lines, the limit is the 2σ value, and the arrow length is 1σ . Sources in italics are those with known molecular outflows.

including all hyperfine components would be 1.67 times larger in the optically thin limit.

The two transitions of ortho- H_2CO exhibit a strong correlation (see Fig. 3) because they arise in the same rotational levels and differ only by the small K splitting, with the 211.2 GHz line on average 20% stronger than the 225.2 GHz line. We therefore computed an average spectrum and line intensity using this ratio. For the several lines we analyzed, Tables 3 and 4 list the derived line intensity, V_{LSR} and line width, ΔV . Figures 4 through 7 display relationships of the line intensities. The color coding in these plots is as follows: blue designates detection of both lines, red designates detection only of the line plotted on the x-axis, and black detection only of the line plotted along the y-axis, and green is for non detection of both lines. Sources in italics are those with known molecular outflows.

The ^{13}CO results are seriously affected by confusion. In many cases, we attempted to fit only a putative disk component, by masking the channels in which confusion seemed likely, either because they appear negative or exceedingly strong, or because of strong C^{17}O emission at the same velocity. A summary of disk detection is given in Table 5. The fits are displayed on top of the ^{13}CO spectra in the figures of Appendix B. The fit results can be found in Table 3. These derived line intensities are presented as a function of CN line flux in Fig. 9. Because of the masking process to ignore confused parts of the spectrum, the errorbars can be large. However, in sources where both ^{13}CO and CN are detected, they in general display similar intensities, within a factor 2.

3. Results

Line emission from these objects can come a priori from 4 distinct regions: molecular cloud(s) along the line of sight, the circumstellar disk, a molecular outflow and (specially for the

youngest objects) a remnant envelope. Molecular cloud will exhibit narrow lines, and because of our observing technique which differentiate the emission with that $1'$ away, may appear in emission or absorption. Disks should lead to symmetric, in general double-peaked, line profiles, and line widths $\propto \sin i$ (with typical values $2-4 \text{ km s}^{-1}$, face-on objects being rare). Contribution from outflows or envelopes may vary considerably, and may be difficult to distinguish from disk emission. Most of the stars in Table 1 have a rich observational history from optical, infrared and radio molecular line observations which can help interpreting the line profiles. We have compiled the relevant information and comment on the observational results for each source in Appendix A.

3.1. Confusion in ^{13}CO

The ^{13}CO spectra are in general complex. Out of the 42 sources, the only two in which ^{13}CO exhibits the expected double-peaked profile which is a clear signature of emission from Keplerian disk are the previously studied objects GG Tau and MWC 480 (see Fig. 2), included here as reference objects. CQ Tau and MWC 758 also exhibit ^{13}CO spectra which can be attributed solely to disk emission. These 4 sources had been previously studied specifically because they are relatively far from the molecular clouds.

For the other sources, the spectrum complexity has two main origins. Narrow features appear in emission or apparent absorption. These narrow features result from small velocity and intensity gradients in the molecular cloud which are on the same line of sight. Our beam-switching observing procedure reveals such gradients on the arcminute scale. Note that, as the switching was made at constant elevation, the gradient direction rotates on the plane of the sky, so that the observed features actually depend on when the observations were performed. A comparison between the spectra of BP Tau obtained here and that published by Dutrey et al. (2003) illustrates this effect. The BP Tau case also demonstrates that the lack of apparent confusion does not imply the source is unaffected by the cloud: a sufficiently optically thick and homogeneous cloud will hide any disk emission situated behind.

Besides contamination by molecular clouds, many sources also exhibit strong, relatively wide profiles in ^{13}CO . Based on prior knowledge about these sources, this emission is in general coming from outflows or envelopes, as in HL Tau, T Tau, Haro 6-10, CB26, DG Tau and DG Tau B, which are all known to drive powerful jets and CO outflows (see Appendix A). This interpretation is corroborated by the emission lines from other molecules (see below). However, the line widths are not very large, so this emission can also contain a substantial contribution from the disk, specially for edge-on disks. An example is IRAS 04302+2247 (hereafter 04302+2247, the Butterfly star, see Wolf et al. 2003), for which IRAM interferometric observations reveal that the detected lines clearly trace the disk (Dutrey et al., in prep.).

Despite confusion with molecular clouds, many other sources exhibit line wings which are potential signatures of disk emission. As mentioned in Sect. 2.3, these sources are identified in Table 5, and appear in Fig. 9.

3.2. CN as a confusion-free disk tracer

There is essentially no evidence for confusion with molecular clouds in CN, except for a few (4 or 5) sources. This can be seen

Table 3. Fit results: CN and ^{13}CO .

Source	CN			^{13}CO			
	Area Jy km s $^{-1}$	V_{LSR} km s $^{-1}$	ΔV km s $^{-1}$	Area Jy km s $^{-1}$	V_{LSR} km s $^{-1}$	ΔV km s $^{-1}$	
FN Tau	<0.38			<i>-1.40 ± 0.09</i>	<i>7.44 ± 0.03</i>	<i>0.84 ± 0.05</i>	<i>Cloud</i>
CW Tau	-0.66 ± 0.07	6.80 ± 0.07	0.85 ± 0.07	2.69 ± 0.45	6.20 ± 0.10	3.25 ± 0.38	
CIDA-1	-0.82 ± 0.09	6.93 ± 0.02	0.42 ± 0.03	1.14 ± 0.75	8.23 ± 0.19	0.56 ± 0.27	
BP Tau	<0.59			<i>0.26 ± 0.14</i>	<i>3.65 ± 0.39</i>	<i>1.06 ± 0.60</i>	<i>Cloud</i>
DE Tau	<0.39			0.20 ± 0.15	11.43 ± 0.99	[3.00]	
RY Tau	3.91 ± 0.86	5.06 ± 1.58	14.22 ± 2.19	2.54 ± 0.51	7.24 ± 0.29	[3.00]	
T Tau	18.62 ± 0.31	7.96 ± 0.03	3.12 ± 0.05	<i>170.37 ± 0.20</i>	<i>8.02 ± 0.00</i>	<i>2.50 ± 0.00</i>	<i>Cloud</i>
Haro 6-5B	0.61 ± 0.13	7.67 ± 0.42	3.61 ± 0.73	<i>14.94 ± 0.30</i>	<i>7.88 ± 0.01</i>	<i>0.80 ± 0.02</i>	<i>Cloud</i>
FT Tau	0.63 ± 0.12	6.95 ± 0.28	2.21 ± 0.42	0.15 ± 0.07	9.38 ± 0.20	0.78 ± 0.34	
DG Tau-B	1.33 ± 0.15	6.18 ± 0.18	2.34 ± 0.22	<i>40.59 ± 0.11</i>	<i>6.43 ± 0.00</i>	<i>2.03 ± 0.00</i>	<i>Cloud</i>
DG Tau	6.62 ± 0.16	6.52 ± 0.03	2.28 ± 0.07	<i>42.08 ± 0.14</i>	<i>6.61 ± 0.00</i>	<i>2.20 ± 0.01</i>	<i>Cloud</i>
Haro 6	11.05 ± 0.22	6.70 ± 0.02	1.97 ± 0.05	<i>41.64 ± 0.47</i>	<i>7.15 ± 0.01</i>	<i>1.07 ± 0.02</i>	<i>Cloud</i>
IQ Tau	2.28 ± 0.21	6.22 ± 0.25	5.07 ± 0.35	0.45 ± 0.14	4.70 ± 0.24	1.45 ± 0.60	
LkHa 358	<0.27			6.91 ± 1.31	6.82 ± 0.04	1.43 ± 0.12	
HH 30	<0.41			8.21 ± 2.97	7.18 ± 0.07	2.34 ± 0.29	
HL Tau	0.81 ± 0.13	5.00 ± 0.20	1.91 ± 0.37	<i>54.88 ± 0.76</i>	<i>5.88 ± 0.01</i>	<i>1.46 ± 0.03</i>	<i>Cloud</i>
HK Tau	1.33 ± 0.22	4.49 ± 0.76	9.25 ± 1.14	1.40 ± 0.62	5.25 ± 0.62	3.12 ± 0.77	
Haro 6-13	0.30 ± 0.08	5.37 ± 0.14	0.69 ± 0.16	10.05 ± 7.19	5.03 ± 0.06	1.67 ± 0.12	
GG Tau	3.20 ± 0.34	6.31 ± 0.17	2.40 ± 0.22	5.01 ± 0.34	6.49 ± 0.09	2.66 ± 0.17	
UZ Tau E	1.21 ± 0.19	5.96 ± 0.47	5.75 ± 0.66	2.61 ± 0.29	5.90 ± 0.18	4.47 ± 0.46	
04302+2247	1.53 ± 0.24	5.92 ± 0.48	5.37 ± 0.55	33.71 ± 1.78	5.62 ± 0.02	2.92 ± 0.06	
DL Tau	1.82 ± 0.15	6.70 ± 0.10	1.41 ± 0.18	0.53 ± 0.24	6.62 ± 0.29	1.29 ± 0.64	
DM Tau	5.90 ± 0.34	6.04 ± 0.07	1.86 ± 0.12	6.84 ± 0.17	6.07 ± 0.02	1.58 ± 0.04	
AA Tau	0.74 ± 0.10	7.36 ± 0.11	0.96 ± 0.15	1.72 ± 0.28	6.38 ± 0.53	6.16 ± 1.03	
DN Tau	1.54 ± 0.17	6.61 ± 0.20	3.17 ± 0.29	0.24 ± 0.09	7.79 ± 0.22	0.98 ± 0.44	
DO Tau	0.84 ± 0.20	5.91 ± 0.22	1.44 ± 0.54	1.18 ± 0.35	3.61 ± 0.85	4.96 ± 1.65	
HV Tau C	1.22 ± 0.20	6.95 ± 0.59	6.51 ± 0.67	2.14 ± 0.61	6.08 ± 0.34	5.02 ± 0.87	
Haro 6-33	0.91 ± 0.17	5.88 ± 0.33	2.98 ± 0.53	1.59 ± 0.60	4.95 ± 0.55	4.52 ± 0.98	
DQ Tau	<0.34			<i>-13.78 ± 0.14</i>	<i>9.62 ± 0.01</i>	<i>1.62 ± 0.01</i>	<i>Cloud</i>
DR Tau	<0.75			6.73 ± 10.82	9.79 ± 1.95	1.80 ± 1.42	
DS Tau	<0.28			<i>0.13 ± 0.08</i>	<i>8.13 ± 0.22</i>	<i>0.64 ± 0.45</i>	<i>Cloud</i>
UY Aur	<0.69			24.09 ± 0.48	6.30 ± 0.01	1.41 ± 0.02	
AB Aur	0.42 ± 0.13	6.87 ± 0.08	0.47 ± 0.09	36.43 ± 0.17	5.89 ± 0.00	1.56 ± 0.01	
SU Aur	<0.27			1.75 ± 0.36	7.09 ± 0.33	3.05 ± 0.47	
MWC 480	3.58 ± 0.23	5.04 ± 0.16	4.44 ± 0.22	7.42 ± 0.21	5.04 ± 0.06	4.18 ± 0.13	
CB26	0.82 ± 0.14	6.20 ± 0.35	3.35 ± 0.45	<i>48.36 ± 0.15</i>	<i>5.68 ± 0.00</i>	<i>1.39 ± 0.00</i>	<i>Cloud</i>
CIDA-8	<0.26			0.46 ± 0.23	7.69 ± 0.68	[3.00]	
CIDA-11	<0.23			<i>0.11 ± 0.05</i>	<i>9.04 ± 0.11</i>	<i>0.30 ± 0.33</i>	<i>Cloud</i>
RW Aur	<0.60			0.84 ± 0.31	2.46 ± 0.59	2.86 ± 1.70	
MWC 758	<0.86			0.82 ± 0.25	6.27 ± 0.39	2.28 ± 0.61	
CQ Tau	<0.28			1.54 ± 0.18	6.01 ± 0.34	5.65 ± 0.70	
HD 163296	10.91 ± 0.23	5.85 ± 0.05	4.28 ± 0.07	6.87 ± 0.68	6.05 ± 0.20	4.02 ± 0.45	

Notes. Integrated line flux of CN (main group of hyperfine components) and ^{13}CO . For ^{13}CO , results in *italics* include cloud (or outflow) emission, while the others were obtained by masking confused channels and trace the disk emission only.

by the lack of narrow features corresponding to those detected in ^{13}CO .

Only two sources exhibit clear evidence of confusion in CN: CW Tau and CIDA-1 (see Figs. B.2 and B.3) in which the CN lines appear in absorption. These two sources are separated by a few arcmin only, and all other lines also display the same behaviour, clearly demonstrating the confusion along this line of sight. The lines are very narrow, 0.44 ± 0.04 km s $^{-1}$, a further indication that this comes from a cold molecular cloud. More detailed arguments about the properties of the molecular cloud and its impact as a confusing signal for disk emission are given in Appendix C.

A closer examination reveals confusion in two other sources, AA Tau and AB Aur, and an unclear situation for Haro 6-13, which exhibit emission with relatively narrow lines (see Table 3

and Appendix A for details). Finally, like for ^{13}CO , a lack of apparent confusion does not indicate an absence of confusion.

CN emission is compatible with optically thin emission in most sources ($\tau_p < 0.5$, where τ_p is the peak line opacity). The HFS method yields τ , the sum of opacities of all hyperfine components. The main group of components accounts for a little more than half of this sum, but with local linewidths in the range 0.2–0.5 km s $^{-1}$, the peak opacity is $\tau_p \sim 0.27\text{--}0.4\tau$, because the hyperfine components overlap only very moderately, being separated by 0.77 and 1.50 km s $^{-1}$. The opacity is constrained in the brightest sources: T Tau has optically thin emission ($\tau = 0.53 \pm 0.06$) but Haro 6-10 exhibits substantial optical depth ($\tau = 3.0 \pm 0.3$, i.e. $\tau_p \approx 1$). The next brightest source, DG Tau, is marginally thick ($\tau = 0.9 \pm 0.3$). The spectra also suggest CN could be optically thick in the Butterfly star

Table 4. Fit results: H₂CO and C¹⁷O.

Source	H ₂ CO			C ¹⁷ O		
	Area Jy km s ⁻¹	V _{LSR} km s ⁻¹	ΔV km s ⁻¹	Area Jy km s ⁻¹	V _{LSR} km s ⁻¹	ΔV km s ⁻¹
FN Tau	0.24 ± 0.06	-0.53 ± 0.14	1.10 ± 0.31	<0.20		
CW Tau	-0.27 ± 0.03	6.80 ± 0.03	0.51 ± 0.05	0.21 ± 0.05	6.28 ± 0.06	0.43 ± 0.11
CIDA-1	-0.25 ± 0.04	6.98 ± 0.03	0.43 ± 0.09	-0.87 ± 0.07	6.91 ± 0.02	0.43 ± 0.01
BP Tau	<0.36			<0.34		
DE Tau	<0.26			<0.56		
RY Tau	<0.28			<1.68		
T Tau	12.68 ± 0.14	7.87 ± 0.01	2.51 ± 0.03	6.07 ± 0.27	7.96 ± 0.04	2.03 ± 0.11
Haro 6-5B	0.19 ± 0.04	8.40 ± 0.21	1.49 ± 0.29	<0.84		
FT Tau	<0.25			<1.08		
DG Tau-B	1.54 ± 0.12	6.43 ± 0.05	1.61 ± 0.19	4.01 ± 0.21	6.44 ± 0.02	0.98 ± 0.06
DG Tau	2.37 ± 0.08	6.43 ± 0.03	1.50 ± 0.06	1.34 ± 0.22	5.87 ± 0.15	2.24 ± 0.48
Haro 6	7.70 ± 0.09	6.59 ± 0.01	1.44 ± 0.02	4.39 ± 0.18	6.39 ± 0.02	0.98 ± 0.05
IQ Tau	<0.25			<0.23		
LkHa 358	0.12 ± 0.03	7.14 ± 0.03	0.28 ± 0.57	1.09 ± 0.10	7.05 ± 0.02	0.45 ± 0.04
HH 30	0.18 ± 0.04	6.06 ± 0.11	0.78 ± 0.15	1.81 ± 0.06	6.52 ± 0.01	0.43 ± 0.00
HL Tau	2.25 ± 0.12	6.66 ± 0.12	4.25 ± 0.28	5.27 ± 0.23	6.35 ± 0.11	5.08 ± 0.28
HK Tau	<0.21			<0.18		
Haro 6-13	1.13 ± 0.10	5.81 ± 0.17	3.85 ± 0.43	2.63 ± 0.30	5.60 ± 0.01	0.43 ± 0.01
GG Tau	0.91 ± 0.19	6.40 ± 0.24	2.02 ± 0.46	<0.50		
UZ Tau E	<0.25			<1.11		
04302+2247	2.82 ± 0.15	5.73 ± 0.13	4.88 ± 0.27	2.23 ± 0.24	6.24 ± 0.20	3.77 ± 0.51
DL Tau	0.65 ± 0.11	6.59 ± 0.26	2.98 ± 0.54	<0.21		
DM Tau	0.54 ± 0.05	6.21 ± 0.06	1.22 ± 0.13			
AA Tau	<0.46			<0.22		
DN Tau	0.26 ± 0.08	5.73 ± 0.28	1.62 ± 0.56	<0.21		
DO Tau	0.33 ± 0.11	5.35 ± 0.39	2.15 ± 0.54	<0.68		
HV Tau C	<0.18			<0.31		
Haro 6-33	0.36 ± 0.05	5.82 ± 0.05	0.67 ± 0.12	<0.24		
DQ Tau	<0.20			<0.46		
DR Tau	<1.36			<1.61		
DS Tau	0.49 ± 0.12	6.08 ± 0.44	3.46 ± 0.80	<0.22		
UY Aur	0.78 ± 0.17	5.92 ± 0.21	1.79 ± 0.40	<0.50		
AB Aur	0.90 ± 0.12	6.11 ± 0.19	2.56 ± 0.29	2.61 ± 0.28	6.02 ± 0.10	2.03 ± 0.25
SU Aur	<0.16			<0.26		
MWC 480	<0.14			1.66 ± 0.26	5.51 ± 0.46	5.60 ± 0.88
CB26	1.56 ± 0.09	5.78 ± 0.06	2.45 ± 0.20	5.77 ± 1.39	5.59 ± 0.04	0.82 ± 0.11
CIDA-8	0.16 ± 0.03	6.75 ± 0.02	0.28 ± 0.58	0.77 ± 0.07	6.77 ± 0.02	0.43 ± 0.00
CIDA-11	<0.19			<0.18		
RW Aur	<0.43			<0.73		
MWC 758	<0.51			2.51 ± 0.77	-0.31 ± 3.07	17.47 ± 4.84
CQ Tau	0.51 ± 0.10	6.15 ± 0.49	4.41 ± 0.77	<2.47		
HD163296	1.38 ± 0.20	5.50 ± 0.37	5.12 ± 0.79			

Notes. Integrated line flux of H₂CO (average of both transitions) and C¹⁷O.

04302+2247, but because of limited signal-to-noise ratio, the significance is low ($\tau = 10 \pm 3$). Spectra of these sources are displayed in Fig. 10, together with the best fit profiles.

Non zero optical depth ($\tau \approx 1$) is also suggested for some of the other strong sources, such as DL Tau, and also DM Tau and LkCa 15, but the error bars remain large. The interferometric study performed by Chapillon et al. (2012) however confirms that CN is not completely optically thin in the latter two sources. Apart from Haro 6-10 and 04302+2247, we found no other source in our sample with optical depth larger than ~ 1 ; the weighted mean opacity is $\sim 0.6^3$.

In summary, we detected CN $N = 2-1$ in 24 out of the 42 stars in our sample, and have only 4 cases of confusion, and essentially all spectra are consistent with total optical depth $\sim 0.3-0.6$.

³ The same value is obtained with or without T Tau.

3.3. SO and H₂CO as outflow or envelope tracers

Strong SO emission is found in 7 out of the 41 stars in which it has been observed (see Fig. 6). All these sources also display relatively strong H₂CO emission (see Fig. 7). All of them, except 04302+2247, are driving well-known jets and outflows. In these sources, CN is either quite strong (DG Tau, T Tau, DG Tau B, Haro 6-10) or very weak (CB26, HL Tau). All these sources are also deeply embedded, and surrounded by an extended complex envelope. We also have a marginal detection of SO in Haro 6-5 B, another embedded, jet-driving object. The line profiles of SO and H₂CO are similar, and resemble those of C¹⁷O when detected. As the line widths are not very wide, this emission may be attributed to the envelope rather than the outflow itself. On the contrary, CN lines often display profiles which are quite different from those of SO, being either narrower (e.g. HL Tau, Fig. B.16) or with no narrow velocity

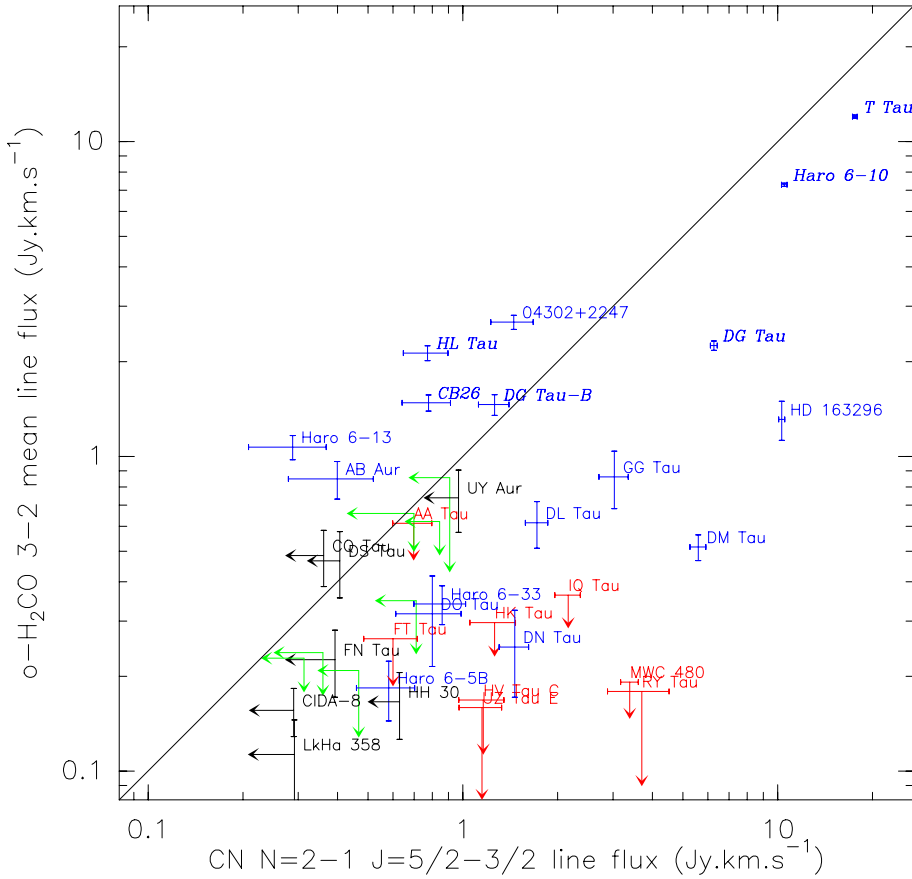


Fig. 4. Integrated line flux of H_2CO (combination of both transitions) vs. $\text{CN } N = 2-1$ (main group of hyperfine components). Color codes indicate detected vs. non-detected lines: blue for detection of both lines, red for detection of the x -axis line only (here CN), black for detection of the y -axis line only (here H_2CO), and green for non-detections. The detection threshold is set at 3σ . For detected lines, the errorbars are 1σ . For non-detected lines, the limit is the 2σ value (best fit + 2σ), and the arrow length is 1σ . Sources in italics are those with known molecular outflows.

component (DG Tau B, Fig. B.10), or (rarely) broader (DG Tau, see Fig. B.11).

The detection rate of H_2CO is rather high, with 20 out of 42 stars observed (not counting the dubious cases FN Tau and CIDA-8). However, cloud contamination appears more important in H_2CO (7 sources with narrow lines out of 42) than in CN . This can be explained by excitation considerations, because of the smaller critical densities of the observed transitions of H_2CO compared to $\text{CN } N = 2-1$. These transitions have similar Einstein coefficients, but the collisional rates of H_2CO with para- H_2 (Troscompt et al. 2009) are typically 5 to 10 times larger than those of CN with para- H_2 at 10 K (Kalugina et al. 2012). On average, CN is brighter than H_2CO (see Fig. 4), and the high detection rate of H_2CO is obtained because two lines of similar intensities could be observed simultaneously and added in this study. Strong H_2CO lines clearly correlates with SO detectability (see Fig. 7), i.e. in general outflow-driving sources.

3.4. C^{17}O and other lines

While ^{13}CO emission from disk is overwhelmed by confusion, C^{17}O is in general too faint to be a suitable tracer of disks (only 9 detections out of 40 observed sources, see Fig. 8). It is convincingly detected in the disks of AB Aur, MWC 480 and 04302+2227 only. On another hand, residual confusion from the cloud is still visible in many sources: CW Tau and CIDA-1, CIDA-8, Haro 6-13, HK Tau, Haro 6-33, Haro 6-5 B, HH 30, and LkHa 358. The strong emission from HL Tau and CB26 presumably comes from their outflows, as the lineshapes are complex and resemble those of SO . For other “outflow” sources, the linewidths are small enough to leave some doubt about the origin.

We also have a 5σ detection of $^{13}\text{C}^{18}\text{O}$ towards Haro 6-10, with a relatively narrow linewidth of $0.7 \pm 0.15 \text{ km s}^{-1}$. A line of similar width is also detected towards AB Aur, at the 4σ level. In the later source, as the disk emission spreads over $2-3 \text{ km s}^{-1}$, this must come from the molecular cloud, and implies that this cloud also contributes to the signal of the other isotopologues.

Finally, emission at the 3σ level appears towards Haro 6-10, MWC 480 and GG Tau near the expected frequency of the $\text{HC}_3\text{N } J = 23-22$ transition, but these features are either too broad, too narrow, or not at the right velocity. No other significant feature appears anywhere else in the observed bandwidth.

4. Discussion

4.1. Using CN as a disk tracer

Our main approach to test whether CN is a disk tracer is to assume that the (mean) CN surface density is independent of the disk properties. This assumption is sustained by several independent arguments. First, the imaging study of DM Tau, LkCa 15 and MWC 480 by Chapillon et al. (2012) give similar CN surface densities in the 3 objects. Second, chemical modeling performed to interpret these CN images predict that the CN surface density is rather insensitive to the disk mass, varying by only $\pm 30\%$ for masses differing a factor 3 in both directions. A similar result was found by Jonkheid et al. (2007) in their models for disk around HAe stars. Last, from an observational point of view, our analysis shows that the CN line optical depth does not appear to exhibit wide variations. We thus assume the CN line opacity to be constant (and relatively small), apart from the 3 sources in which it is clearly determined. Under this assumption, the total flux is directly related to the total number of CN molecules, i.e. principally by the disk outer radius ($S_\nu \propto R_{\text{out}}^2$).

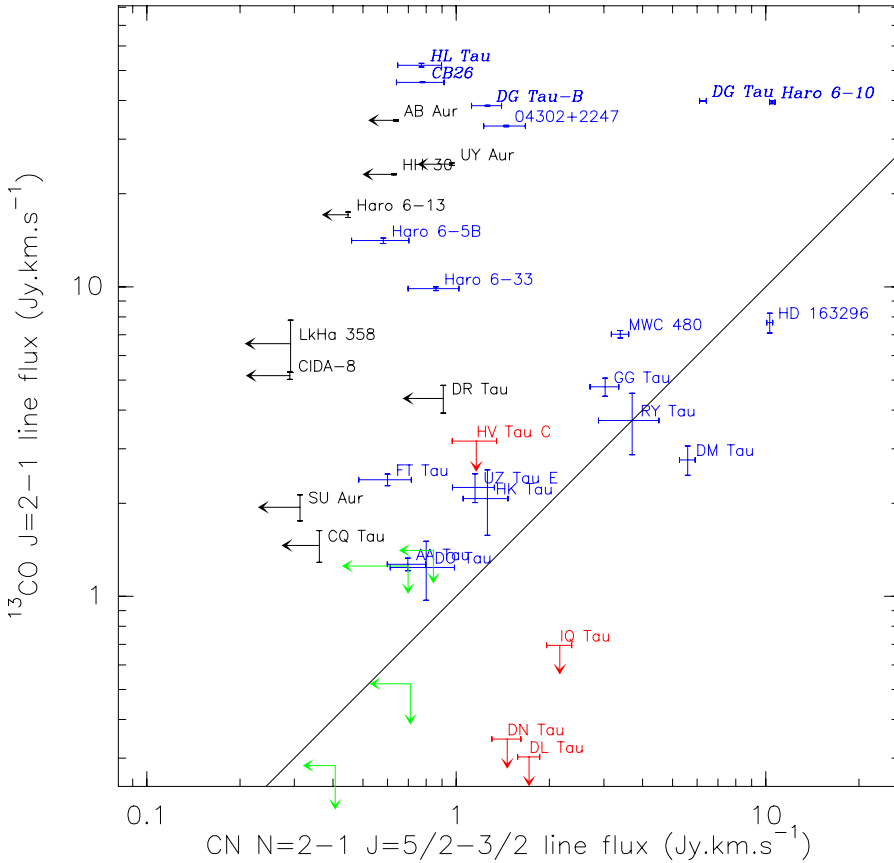


Fig. 5. As for Fig. 4 but for $^{13}\text{CO } J = 2-1$ (including contribution from the cloud) vs. CN $N = 2-1$. T Tau is out of scale here.

For a quantitative derivation of R_{out} , we use the approach of Guilloteau & Dutrey (1998) which shows that, at moderate inclinations ($20^\circ < i < 70^\circ$), the line flux from a Keplerian disk is related to local line width and disk outer radius:

$$R_{\text{out}} = D \left(\frac{\int S_\nu d\nu}{B_\nu(T_0)(\rho\Delta V)\pi\cos(i)} \right)^{1/2} \quad (2)$$

where D is the distance (140 pc), T_0 the excitation temperature, ΔV the local line width, i the inclination, and ρ a factor depending on line opacity along the line of sight. The rationale for and derivation of Eq. (2) are given in Appendix D. In the optically thin regime, ρ is proportional to the opacity, which is itself inversely proportional to $\cos(i)$, so the dependency on inclination disappears, and the flux just scales with the total number of molecules. In this optically thin case, Eq. (2) can be extrapolated to low inclinations $i < 20^\circ$. For nearby edge-on objects, where the above formula breaks, Beckwith & Sargent (1993) have shown that the expected flux is not a strong function of inclination. Hence the apparent dependence on i essentially vanishes. We thus use $\rho \cos(i) = 0.3 \cos(45^\circ)$ for all sources in which the opacity cannot be determined from our spectra, and, for the few sources in which τ is determined by the HFS fit, we use $\rho \cos(i) = \tau \cos(45^\circ)$. However, larger disks with smaller average line opacity can equally fit the data: in this respect, the derived radii are thus likely to be *lower limits* to the true CN disk size.

For the other parameters, we take $\Delta V = 0.2 \text{ km s}^{-1}$, a value consistent with the local line width determined in the disks of DM Tau, LkCa 15 and MWC 480 by Piétu et al. (2007) and Chapillon et al. (2012). For the temperature, Chapillon et al. (2012) derived 30 K for MWC 480, but values (10–15 K) for DM Tau and LkCa 15. We used 15 or 30 K according to our best

knowledge of source properties. Note that the derived disk radius will scale as $1/\sqrt{T_0}$ (Eq. (2)). The assumed temperatures and derived disk radii are given in Table 5 for a uniform disk distance of 140 pc. Given the uncertainty on the CN opacity, these radii should only be interpreted as estimates of the disk size. They range from <200 AU for non detection, to >1000 AU for the brightest sources. For MWC 480 and DM Tau, the derived radius is in good agreement with the more accurate determination from interferometric data of Chapillon et al. (2012), justifying a posteriori our choice of parameter values.

For T Tau and Haro 6-10, the CN line opacity is reasonably well constrained. The large disk radii which are derived make the disk interpretation very unlikely, as both objects contain multiple systems with strong evidence for tidal truncation of the embedded circumstellar disks to outer radii <60 AU (Akeson et al. 1998; Guilloteau et al. 2011). Both systems also display clear evidence for high velocity wings in CO, indicating powerful molecular jets. Hence, for these objects, CN may come from the outflows rather than from a circum-stellar/binary disk. As the line width are however limited, it is also possible that a substantial fraction of CN comes from the extended envelope in which these objects are embedded.

For DG Tau, although modeling performed by Salter et al. (2011) shows the CN line intensity can be produced by a large Keplerian disk, we suspect that a similar situation occurs because of the strong outflow and complex, clearly non Keplerian, circumstellar environment (see Appendix A for more details on this source).

For other sources, a disk origin for the CN emission is inferred from the following qualitative arguments:

- The line-width Δv derived from the Gaussian fit is of the order of 2–4 km s^{-1} , as expected for a Keplerian disk orbiting a star of $0.5-2 M_\odot$.

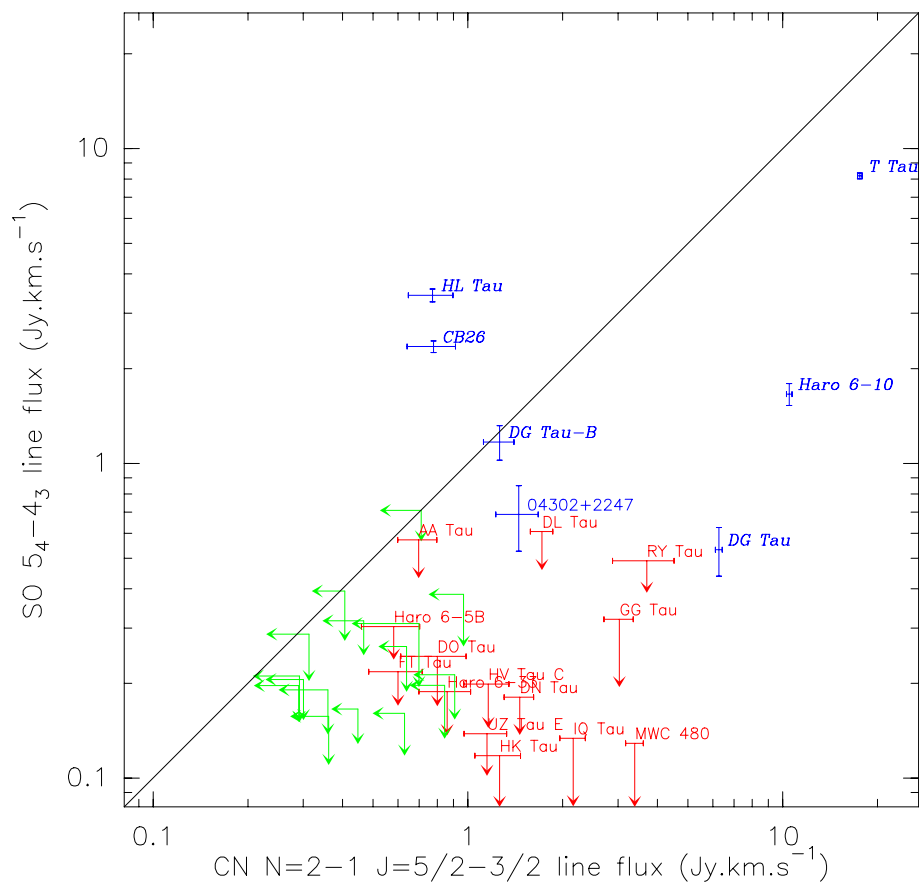


Fig. 6. As for Fig. 4 but for SO vs. CN $N = 2-1$.

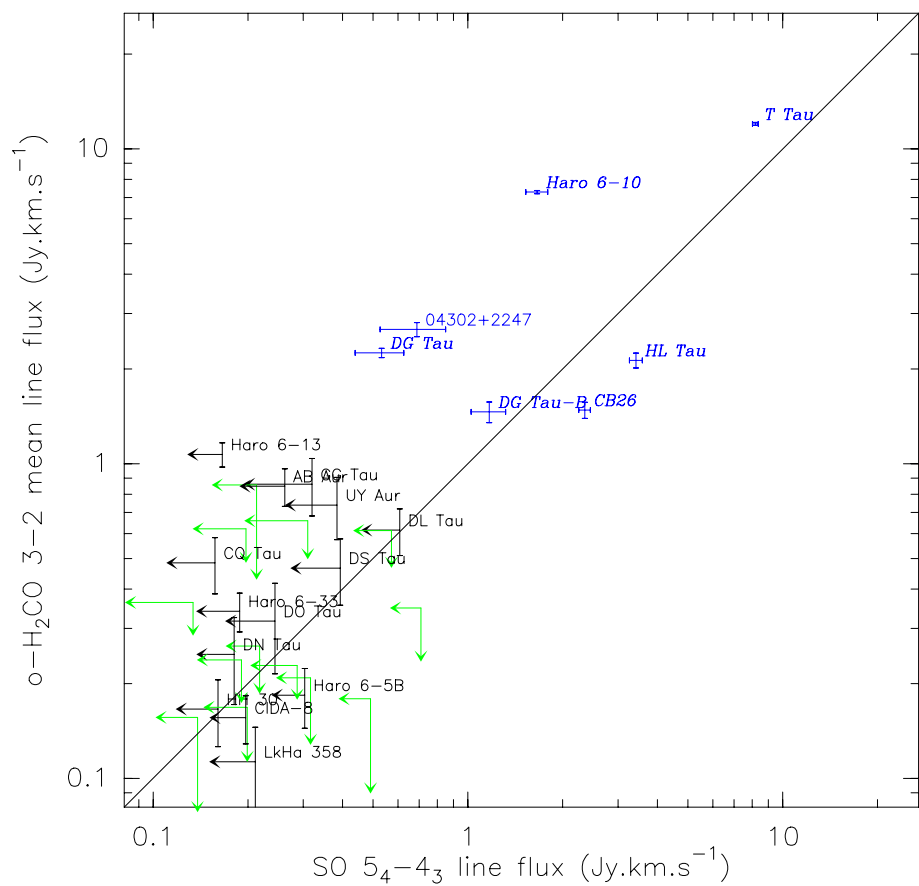


Fig. 7. As for Fig. 4 but for H₂CO vs. SO.

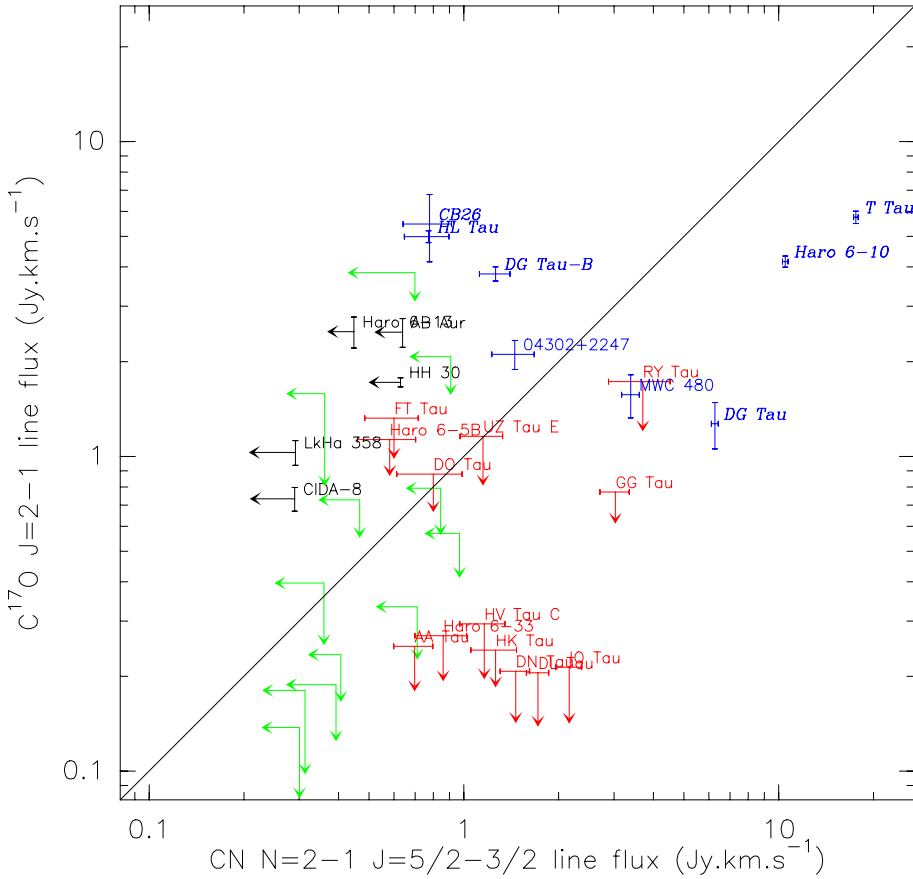


Fig. 8. As for Fig. 4 but for $C^{17}O$ $J = 2-1$ vs. CN $N = 2-1$.

- Larger line widths are found for the more inclined objects (see Fig. 11). This figure does not correct for stellar mass: doing so would improve the correlation between line width and inclination.
- The CN outer radius is within 300–600 AU, in good agreement with the range of interferometrically derived radii in previously imaged Keplerian disks.
- In objects which have already been imaged in CN, MWC 480, DM Tau, LkCa 15 (Chapillon et al. 2012), GM Aur and AA Tau (Öberg et al. 2010), CN unambiguously comes from the disk, even in the confused case of AA Tau.

Note that none of the main CN line profiles appears double peaked (e.g. compare CN and ^{13}CO in MWC 480 Fig. 2). This is a result of the overlap between the three strongest $J = 5/2-3/2$ hyperfine components which are separated by 0.77 and 1.50 $km\ s^{-1}$ respectively. These separations are smaller than the overall width due to Keplerian shear, significantly blurring the expected double peaked profiles emerging from such disks in (spatially) unresolved observations. However, the velocity separations are larger than the local line width (0.3–0.5 $km\ s^{-1}$), so that in resolved (interferometric) images, the patterns from each of the three components are spatially separated. Furthermore, the strongest $J = 3/2-1/2$ component, which is separated by 17 $km\ s^{-1}$ from the nearest one, is only 1.6 times weaker than the $J = 5/2-3/2$ $F = 5/2-3/2$ component. In practice, the hyperfine structure of CN is only a minor complication in the derivation of the kinematics from interferometric measurements, especially at the high densities encountered in disks, which ensures that all hyperfine components will have the same excitation temperature.

To the 24 sources detected in CN in our sample, we should add 5 more disks: GM Aur (Öberg et al. 2010), LkCa 15

(Chapillon et al. 2012), CI Tau, CY Tau, and GO Tau (Guilloteau et al., in prep.), leading to a total of 29 detections out of 47 objects. 3 (Haro 6-10, T Tau and DG Tau) are very unlikely to be disks, and, on the basis of the existence of outflows and SO detection, 2 more are perhaps outflows (HL Tau and CB26). This still leads to a disk detection rate of at least 24/47, i.e. $\geq 50\%$ at our sensitivity level of ~ 0.1 $Jy\ km\ s^{-1}$. Furthermore, in most disks, the CN $N = 2-1$ intensity is within a factor 2 of that of ^{13}CO $J = 2-1$ (see Fig. 9).

This demonstrates the ability of the CN 2–1 line to be a good tracer of disk kinematics for stars still embedded in molecular clouds whose CO and ^{13}CO line emission could confuse the disk emission profile.

4.2. Molecular disk properties

Our study is the first large, sensitive survey for ^{13}CO , CN, ortho- H_2CO , and SO towards disk around Class II PMS stars. Detailed sensitive studies of several molecules concerned only a few objects: in Taurus only GG Tau, DM Tau, LkCa 15 and MWC 480 (Dutrey et al. 1997; Guilloteau et al. 1999; Thi et al. 2004; Piétu et al. 2007; Chapillon et al. 2012; Dutrey et al. 2011). Previous multi-molecule surveys were limited to a dozen objects, and in general biased towards the brightest disks, either in CO (e.g. the DISCS survey of Öberg et al. 2011), or in continuum (Salter et al. 2011, used a minimum 1.3 mm continuum flux of 75 mJy). We reach here a sensitivity level (~ 0.1 $Jy\ km\ s^{-1}$) comparable to or better than that of Öberg et al. (2011), and 5 to 10 times better than that of Salter et al. (2011). Furthermore, the smaller beam size of the 30-m allows to better isolate confusion cases compared to the JCMT study of Salter et al. (2011). The improved sensitivity allows us to detect many more sources, such

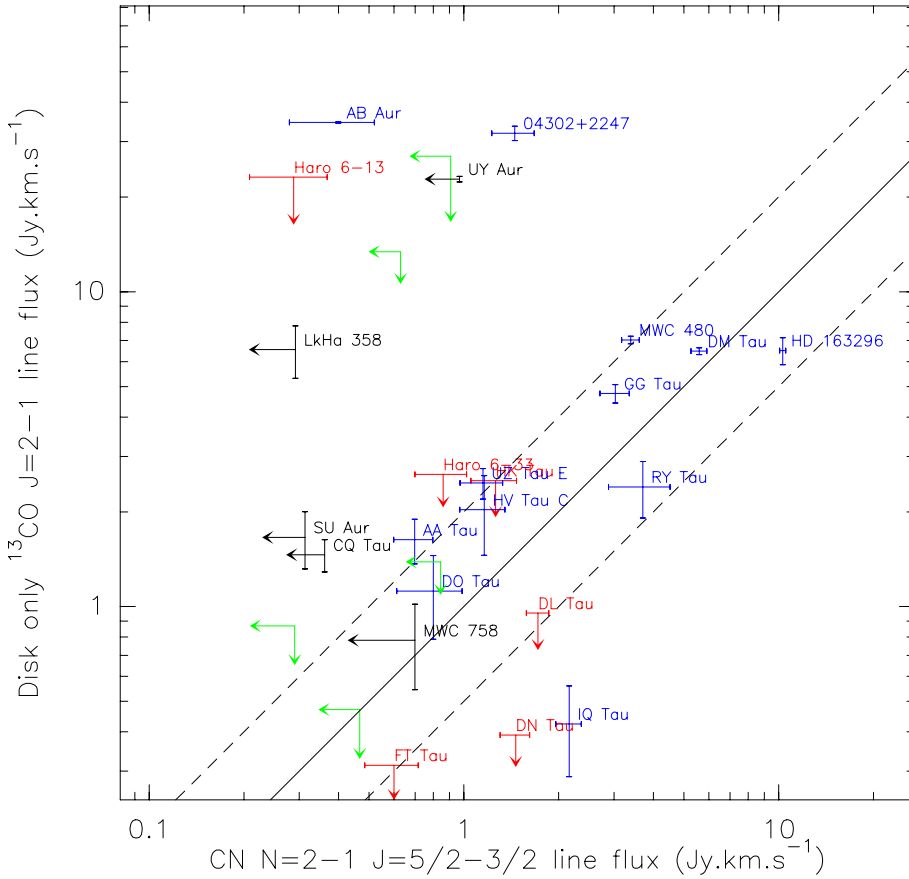


Fig. 9. As for Fig. 4 but for ^{13}CO (disk component only) vs. CN. The dashed lines indicate a factor 2 between the two line fluxes.

as FT Tau, IQ Tau, V806 Tau (Haro 6-13), UZ Tau, DN Tau, DO Tau in the Salter et al. sample. Excluding sources detected in SO which are presumably contaminated by outflows, we have a total of 32 sources⁴ (out of 47) which exhibit CN, ^{13}CO or H_2CO emission from a disk, i.e. 68% of the sample.

Figures 12 and 13 explore possible correlation of the CN intensity with spectral type of the star and 1.3 mm continuum flux of the disk respectively. Figure 14 considers the $\text{H}_2\text{CO}/\text{CN}$ intensity ratio vs. the stellar spectral type. Despite the large sample size, no correlations are apparent. This lack of correlation is also observed for other stellar parameters (mass loss, X-ray luminosity). However, a number of properties emerge from these correlation plots.

First, CN line is relatively weak (in fact undetected so far) in the hottest stars in our sample (SU Aur, CQ Tau, MWC 758, AB Aur), although MWC 480 and HD 163296 exhibit strong CN emission (Fig. 12). The rather poor molecular content of AB Aur has been shown to be a consequence of its strong UV flux by Schreyer et al. (2008). The UV flux penetration may furthermore be enhanced by the large inner cavity (radius ~ 100 AU) of AB Aur (Piétu et al. 2005). A similar situation may occur for MWC 758 due to its ~ 40 AU cavity (Isella et al. 2010b). Chapillon et al. (2008, 2010) argue that CQ Tau is gas deficient. Little is known about the gas disk of SU Aur, but the strong X-ray luminosity of SU Aur may play a role in lowering the molecular abundances. MWC 480 and HD 163296 have strong CN. Contrary to AB Aur, CQ Tau and MWC 758 which are Type I sources, these two sources are Type II according to

the classification of Meeus et al. (2001), which can indicate self-shadowed disks. Such a configuration would seriously limit the UV penetration, leading to a chemical composition much more similar to those of T Tauri disks.

Second, at the level of our sensitivity, we do not detect the CN line for spectral types cooler than M1.5 (Fig. 12). Assuming similar CN column densities than in the warmer stars, our sensitivity translates into upper limits of order 150–250 AU for the disk outer radius. Thus, our negative result may only be the consequence of smaller disk sizes for lower mass stars, rather than implying a change in chemistry at this spectral type threshold.

Third, although CN intensity does not correlate with the continuum flux at 1.3 mm (Fig. 13), which is a tracer of the dust mass, there is a clear threshold. Only 4 sources with $S_\nu(1.3 \text{ mm}) > 60$ mJy are undetected in CN (CW Tau, CQ Tau, DQ Tau, and DR Tau which has been observed with relatively limited sensitivity) while only 4 sources are detected among the 17 sources with $S_\nu(1.3 \text{ mm}) \leq 60$ mJy.

Comparing the emissions from CN and H_2CO , we find that to first order, the $\text{H}_2\text{CO}/\text{CN}$ ratio divides the sources in two categories (see Fig. 14). $[\text{H}_2\text{CO}/\text{CN}] > 0.5$ is found in warm sources (Herbig Ae stars) or outflow/envelope dominated objects, while it is below 0.3 for the disk sources. This trend is consistent with our current understanding of chemistry. In disks, H_2CO is formed in the gas phase and on grains (Semenov & Wiebe 2011). Therefore, H_2CO can be released in the gas phase at high enough temperatures, either because of large stellar flux (HAe stars) or because of shock heating (outflow sources). Enhanced abundance of H_2CO has been observed in many outflows (e.g. Bachiller et al. 2001; Tafalla et al. 2010). As a consequence, sources with weak or no H_2CO emission mostly correspond to cold objects without outflows. While CN appears as

⁴ This includes the 16 sources detected in CN that have no SO emission, plus the Butterfly star, plus 8 sources in ^{13}CO (including HH 30) and 2 sources in H_2CO (Haro 6-13 and DS Tau), to which we add the 5 sources detected in CN by other studies.

Table 5. CN outer radii and line detections.

Source	Radius (AU)	T_0 (K)	Line width km s^{-1}	Detection?		
				^{13}CO	H_2CO	SO
FN Tau	<170	15			Cloud	
CW Tau	<170	15		Disk		
CIDA-1	<170	15				
BP Tau	<250	30				
DE Tau	<250	15				
RY Tau	310	30	0.82 ± 0.27	Disk		
T Tau	1230	30	2.96 ± 0.02		Yes	Yes
Haro 6-5B	310	15	3.12 ± 1.17		Yes	
FT Tau	310	15	1.69 ± 0.34			
DG Tau-B	450	15	2.12 ± 0.30		Yes	Yes
DG Tau	700	30	2.11 ± 0.09		Yes	Yes
Haro 6-10	660	30	1.50 ± 0.04		Yes	Yes
IQ Tau	560	15	4.92 ± 0.53	Disk		
LkHa 358	<240	15		Disk	Yes	
HH 30	<270	15		(Disk)	Yes	
HL Tau	250	30	1.79 ± 0.44		Yes	Yes
HK Tau	320	30	8.56 ± 1.96			
Haro 6-13	$\lesssim 280$	15			Yes	
GG Tau	490	30	2.28 ± 0.32	Disk	Yes	
UZ Tau E	310	30	6.58 ± 1.23	Disk		
04302+2247	190	30	2.99 ± 0.47	Disk	Yes	Yes
DL Tau	560	15	1.96 ± 0.16		Yes	
DM Tau	610	15	1.44 ± 0.11	Disk	Yes	
AA Tau	300	15	0.95 ± 0.26	Disk		
DN Tau	490	15	3.21 ± 0.42		Yes	
DO Tau	310	15	0.50 ± 0.17	Disk	Yes	
HV Tau C	310	30	5.97 ± 0.87	Disk		
Haro 6-33	260	30	3.05 ± 0.68		Yes	
DQ Tau	<210	15				
DR Tau	<420	15				
DS Tau	<310	30			Yes	
UY Aur	<300	30		Disk	Yes	
AB Aur	<250	30		Disk	Yes	
SU Aur	<140	30		Disk		
MWC 480	520	30	4.54 ± 0.34	Disk		
CB 26	350	15	2.92 ± 1.00		Yes	Yes
CIDA-8	<290	15			Cloud	
CIDA-11	<540	15				
RW Aur	<280	30				
MWC 758	<450	30		Disk		
CQ Tau	<190	30		Disk	Yes	
HD 163296 ^a	760	30	4.16 ± 0.11	Disk	Yes	

Notes. The assumed distance is $D = 140$ pc, except for HD 163296 (^a, $D = 120$ pc). For ^{13}CO , sources in which the emission partially originates from a disk are indicated. For H_2CO , no distinction is made upon the origin of the emission, apart from the two likely cases of cloud confusion FN Tau and CIDA-8.

a clear disk tracer in the M1-K5 spectral type range, the situation is more complex for the HAe stars, for which H_2CO is sometimes a better probe than CN, but remains weak. Using the Baraffe et al. (1998) tracks, the M1 limit corresponds to about $0.5 M_\odot$ for stars in the 1 to 3 Myr age.

Sulfur-bearing molecules (CS, SO, H_2S and CCS) have been recently searched by Dutrey et al. (2011) and Chapillon et al. (2012) in the four disks surrounding MWC 480, LkCa 15, GO Tau and DM Tau. So far, only CS has been detected, neither SO nor H_2S . Our survey provides a much larger sample for SO, and confirms its general weakness in disks (only one source detected, 04302+2242, our results contradicting the detection in AB Aur reported by Fuente et al. 2010). On the other hand, we find SO to be ubiquitous in outflow sources. The SO chemistry

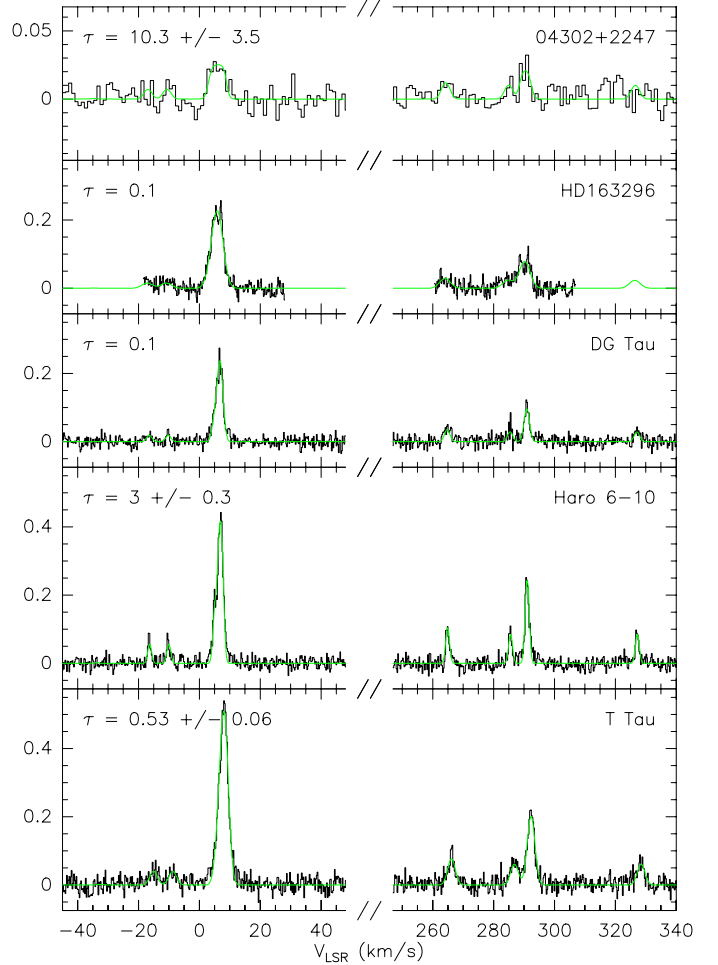


Fig. 10. Hyperfine components of CN in bright, potentially thick sources. The best fit with the hyperfine components is overlaid. The intensity scale is T_A^* (K).

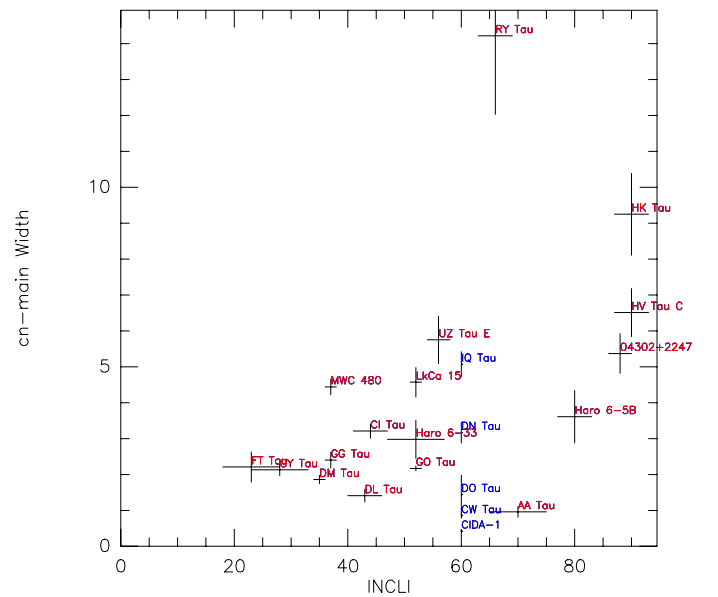


Fig. 11. CN line width (km s^{-1}) as a function of disk inclination. Sources with unknown inclinations are in blue: we used $i = 60^\circ$ as the most likely value. Sources with outflows were excluded.

in disks is not fully understood: current models predict too much SO and H_2S molecules (Dutrey et al. 2011), most likely as a

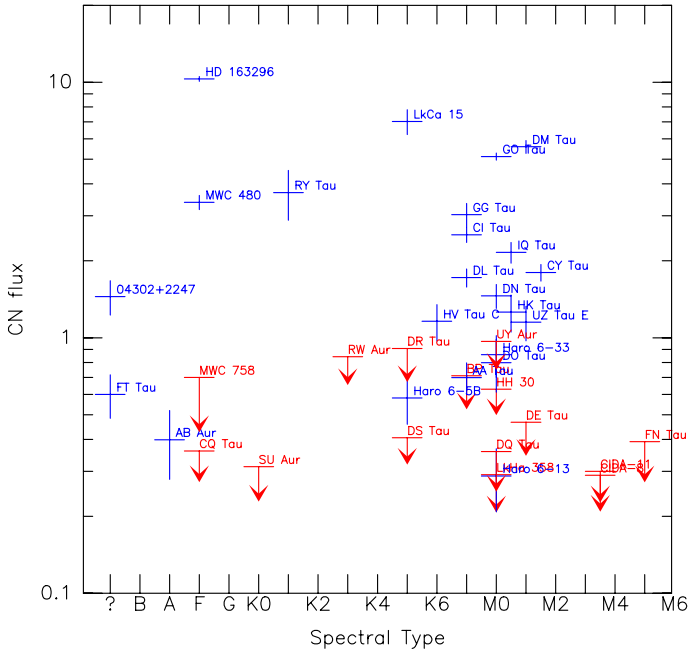


Fig. 12. Correlation between CN line flux (main fine structure group, in Jy km s^{-1}) and stellar spectral type. Blue is for detected sources, red for upper limits. Sources with outflows were excluded. Emission in AB Aur is from the envelope.

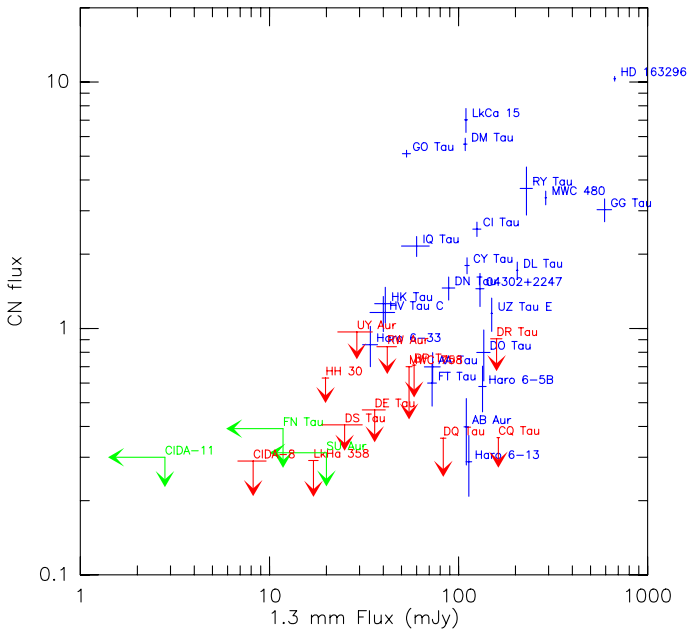


Fig. 13. As Fig. 12, but for CN line flux (main fine structure group) vs. 1.3 mm continuum flux (in mJy).

result of incomplete treatment of Sulfur chemistry on grain surfaces. However, SO is a clear tracer of shocks, with high abundances in extremely high velocity outflows (Tafalla et al. 2010).

The absence of correlations in Figs. 12, 13 justifies a posteriori our simple source-independent hypothesis (essentially constant CN surface density) to interpret the line emission. In this framework, the CN flux is a simple tracer of disk size, and our study shows that *at least 50%* of the young stars are surrounded by *large* (≥ 300 AU) disks, in our specific case of isolated star formation. The overall *disk* detection rate is displayed in Fig. 15.

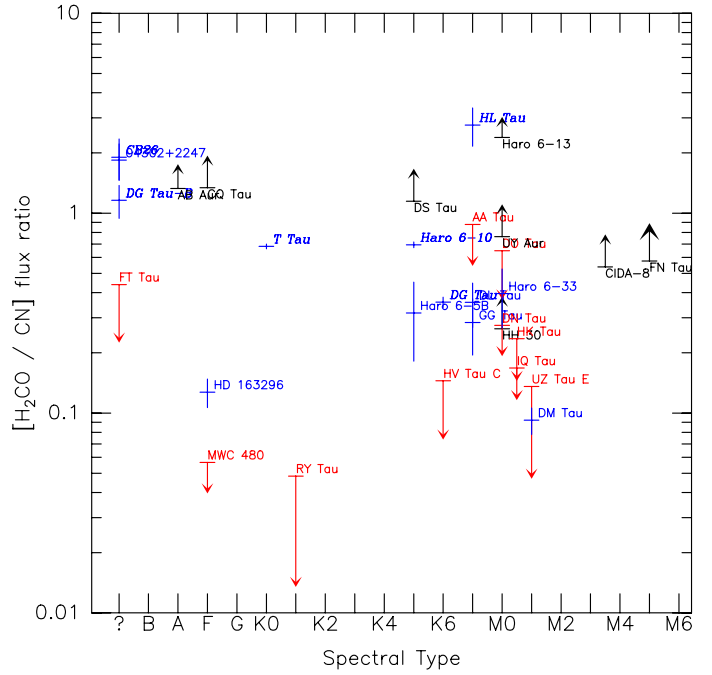


Fig. 14. Correlation between the H_2CO to CN flux ratio and stellar spectral type. Red indicates upper limits (no H_2CO), black lower limits (no CN). H_2CO in FN Tau and CIDA 8 is likely to be cloud contamination. Outflow sources are in italics.

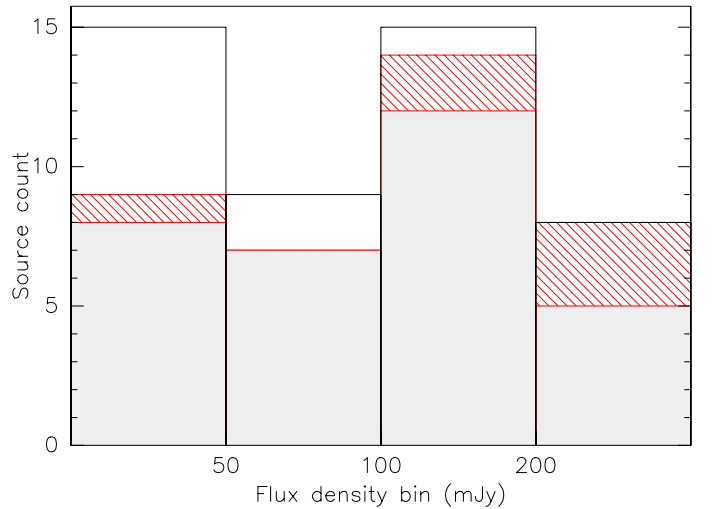


Fig. 15. Histogram of detections as a function of 1.3 mm continuum flux range. Filled: disks, hatched: outflow contaminated sources, empty: non detections.

Hatched areas are for sources with molecular outflows (traced by SO), filled areas are disks detected in CN, ^{13}CO or H_2CO , and empty histograms non detections. The distribution of disk sizes exhibits a strong peak near 300 AU; however, because of sensitivity limitations, our survey becomes incomplete for smaller disk sizes.

It is beyond the scope of our angularly unresolved data to provide detailed modeling of the disk emission for individual objects. The above considerations on the detected lines are broadly consistent with prior knowledge of disk chemistry. The large CN detection rate supports the simple idea that CN is present only in a photodissociation layer above the disk plane, with a relatively uniform surface density over a large range of source properties

(Jonkheid et al. 2007; Chapillon et al. 2012). The lower detection rate for sources with low 1.3 mm flux may be the result of a change of chemical regime for disks with low mass. However, it is also consistent with a simpler idea, namely that these faint disks are just much smaller than the others. Higher sensitivity, spatially resolved observations can solve this issue.

5. Summary

We have performed a sensitive survey of 42 young stars probing isolated star formation regions in CN, ortho-H₂CO, SO, ¹³CO and C¹⁷O rotational lines near 206–228 GHz with the IRAM 30-m telescope. It reveals that:

- ¹³CO is strongly affected by confusion, either from molecular clouds, or from outflows and envelopes.
- CN is a good, nearly confusion free, tracer of disks for stars in the M1-K5 spectral type range (i.e. stars more massive than about 0.5 M_⊙ according to the Baraffe et al. (1998) tracks).
- The warmest stars exhibit two very different behaviours: some have strong CN, but most have undetectable CN and weak H₂CO emission.
- SO is ubiquitously found in outflow-driving, embedded sources, but exceptional in disks (only 1 source). When SO is present, H₂CO is stronger than CN.
- CN *N* = 2–1 is strong enough to be a good tracer of disk kinematics in at least half of the objects.
- The disk detection rate in CN lines exceeds 50%. The detected disks are large, ≥300 AU in radius.
- The overall gas disk detection rate (by any molecular tracer) is ≈68%. However, gas disk detection is much more difficult for sources with small (≤60 mJy) 1.3 mm continuum flux. We cannot distinguish at present whether this is due to smaller disk masses or smaller disk sizes (<200 AU radius).

Our results only apply to regions of isolated star formation. In more crowded regions (e.g. ρ Oph), confusion will unavoidably be larger. The disk size distribution may also be different. It is however likely that CN will remain a better tracer of disk kinematics than the much more confused ¹²CO or ¹³CO, or the significantly weaker H₂CO emission. Looking to the advent of ALMA, with 8 times greater collecting area than the IRAM 30-m, better antenna efficiency, and expected system temperatures around 100 K at this frequency, will provide a sensitivity gain of order 16. Thus ALMA should be able to obtain, in the same integration time, a 4 times better limit on the outer radius. This may open for the first time the possibility to probe beyond the M1 limit, unless the chemistry changes to reduce drastically the CN abundances around the lower mass stars.

Acknowledgements. This work was supported by “Programme National de Physique Stellaire” (PNPS) and “Programme National de Physique Chimie du Milieu Interstellaire” (PCMI) from INSU/CNRS. The work of M.S. was supported in part by NSF grant AST 09-07745. This research has made use of the SIMBAD database, operated at CDS, Strasbourg, France.

References

Akeson, R. L., Koerner, D. W., & Jensen, E. L. N. 1998, *ApJ*, 505, 358
 Akeson, R. L., Ciardi, D. R., van Belle, G. T., & Creech-Eakman, M. J. 2002, *ApJ*, 566, 1124
 Andrews, S. M., & Williams, J. P. 2005, *ApJ*, 631, 1134
 Bachiller, R., Pérez Gutiérrez, M., Kumar, M. S. N., & Tafalla, M. 2001, *A&A*, 372, 899
 Banzatti, A., Testi, L., Isella, A., et al. 2011, *A&A*, 525, A12

Baraffe, I., Chabrier, G., Allard, F., & Hauschildt, P. H. 1998, *A&A*, 337, 403
 Beckwith, S. V. W., & Sargent, A. I. 1993, *ApJ*, 402, 280
 Bertout, C., Robichon, N., & Arenou, F. 1999, *A&A*, 352, 574
 Bertout, C., Siess, L., & Cabrit, S. 2007, *A&A*, 473, L21
 Bouvier, J., Chelli, A., Allain, S., et al. 1999, *A&A*, 349, 619
 Briceño, C., Calvet, N., Gomez, M., et al. 1993, *PASP*, 105, 686
 Briceño, C., Luhman, K. L., Hartmann, L., Stauffer, J. R., & Kirkpatrick, J. D. 2002, *ApJ*, 580, 317
 Cabrit, S., Guilloteau, S., Andre, P., et al. 1996, *A&A*, 305, 527
 Cabrit, S., Pety, J., Pesenti, N., & Dougados, C. 2006, *A&A*, 452, 897
 Chakraborty, A., & Ge, J. 2004, *AJ*, 127, 2898
 Chapillon, E., Guilloteau, S., Dutrey, A., & Piétu, V. 2008, *A&A*, 488, 565
 Chapillon, E., Parise, B., Guilloteau, S., Dutrey, A., & Wakelam, V. 2010, *A&A*, 520, A61
 Chapillon, E., Guilloteau, S., Dutrey, A., Piétu, V., & Guélin, M. 2012, *A&A*, 537, A60
 Crutcher, R. M., Churchwell, E., & Ziurys, L. M. 1984, *ApJ*, 283, 668
 Duchêne, G., McCabe, C., Pinte, C., et al. 2010, *ApJ*, 712, 112
 Dutrey, A., Guilloteau, S., Duvert, G., et al. 1996, *A&A*, 309, 493
 Dutrey, A., Guilloteau, S., & Guélin, M. 1997, *A&A*, 317, L55
 Dutrey, A., Guilloteau, S., & Simon, M. 2003, *A&A*, 402, 1003
 Dutrey, A., Wakelam, V., Boehler, Y., et al. 2011, *A&A*, 535, A104
 Duvert, G., Dutrey, A., Guilloteau, S., et al. 1998, *A&A*, 332, 867
 Duvert, G., Guilloteau, S., Ménard, F., Simon, M., & Dutrey, A. 2000, *A&A*, 355, 165
 Eislöffel, J., & Mundt, R. 1998, *AJ*, 115, 1554
 Franciosini, E., Scelsi, L., Pallavicini, R., & Audard, M. 2007, *A&A*, 471, 951
 Fuente, A., Cernicharo, J., Agúndez, M., et al. 2010, *A&A*, 524, A19
 Greaves, J. S. 2005, *MNRAS*, 364, L47
 Guilloteau, S., & Dutrey, A. 1998, *A&A*, 339, 467
 Guilloteau, S., Dutrey, A., & Simon, M. 1999, *A&A*, 348, 570
 Guilloteau, S., Piétu, V., Dutrey, A., & Guélin, M. 2006, *A&A*, 448, L5
 Guilloteau, S., Dutrey, A., Piétu, V., & Boehler, Y. 2011, *A&A*, 529, A105
 Hernández, J., Calvet, N., Briceño, C., Hartmann, L., & Berlind, P. 2004, *AJ*, 127, 1682
 Hirth, G. A., Mundt, R., & Solf, J. 1994, *A&A*, 285, 929
 Horne, K., & Marsh, T. R. 1986, *MNRAS*, 218, 761
 Hughes, A. M., Wilner, D. J., Andrews, S. M., Qi, C., & Hogerheijde, M. R. 2011, *ApJ*, 727, 85
 Isella, A., Testi, L., Natta, A., et al. 2007, *A&A*, 469, 213
 Isella, A., Carpenter, J. M., & Sargent, A. I. 2010a, *ApJ*, 714, 1746
 Isella, A., Natta, A., Wilner, D., Carpenter, J. M., & Testi, L. 2010b, *ApJ*, 725, 1735
 Jonkheid, B., Dullemond, C. P., Hogerheijde, M. R., & van Dishoeck, E. F. 2007, *A&A*, 463, 203
 Kalugina, Y., Lique, F., & Kłos, J. 2012, *MNRAS*, 422, 812
 Kenyon, S. J., & Hartmann, L. 1995, *ApJS*, 101, 117
 Kitamura, Y., Kawabe, R., & Saito, M. 1996, *ApJ*, 457, 277
 Krist, J. E., Stapelfeldt, K. R., Burrows, C. J., et al. 1998, *ApJ*, 501, 841
 Launhardt, R., Pavlyuchenkov, Y., Gueth, F., et al. 2009, *A&A*, 494, 147
 Liu, C.-F., Shang, H., Pyo, T.-S., et al. 2012, *ApJ*, 749, 62
 Luhman, K. L., Allen, P. R., Espaillat, C., Hartmann, L., & Calvet, N. 2010, *ApJS*, 186, 111
 McCabe, C., Duchêne, G., Pinte, C., et al. 2011, *ApJ*, 727, 90
 Meeus, G., Waters, L. B. F. M., Bouwman, J., et al. 2001, *A&A*, 365, 476
 Mitchell, G. F., Sargent, A. I., & Mannings, V. 1997, *ApJ*, 483, L127
 Momose, M., Ohashi, N., Kawabe, R., Hayashi, M., & Nakano, T. 1996, *ApJ*, 470, 1001
 Monin, J.-L., Pudritz, R. E., & Lazareff, B. 1996, *A&A*, 305, 572
 Müller, H. S. P., Thorwirth, S., Roth, D. A., & Winnewisser, G. 2001, *A&A*, 370, L49
 Nguyen, D. C., Brandeker, A., van Kerkwijk, M. H., & Jayawardhana, R. 2012, *ApJ*, 745, 119
 Öberg, K. I., Qi, C., Fogel, J. K. J., et al. 2010, *ApJ*, 720, 480
 Öberg, K. I., Qi, C., Fogel, J. K. J., et al. 2011, *ApJ*, 734, 98
 Osterloh, M., & Beckwith, S. V. W. 1995, *ApJ*, 439, 288
 Padgett, D. L., Brandner, W., Stapelfeldt, K. R., et al. 1999, *AJ*, 117, 1490
 Pety, J., Gueth, F., Guilloteau, S., & Dutrey, A. 2006, *A&A*, 458, 841
 Piétu, V., Guilloteau, S., & Dutrey, A. 2005, *A&A*, 443, 945
 Piétu, V., Dutrey, A., & Guilloteau, S. 2007, *A&A*, 467, 163
 Prato, L., Lockhart, K. E., Johns-Krull, C. M., & Rayner, J. T. 2009, *AJ*, 137, 3931
 Pyo, T., Kobayashi, N., Hayashi, M., et al. 2003, *ApJ*, 590, 340
 Qi, C., D’Alessio, P., Öberg, K. I., et al. 2011, *ApJ*, 740, 84
 Ratzka, T., Schegerer, A. A., Leinert, C., et al. 2009, *A&A*, 502, 623
 Roccatagliata, V., Ratzka, T., Henning, T., et al. 2011, *A&A*, 534, A33
 Salter, D. M., Hogerheijde, M. R., van der Burg, R. F. J., Kristensen, L. E., & Brinch, C. 2011, *A&A*, 536, A80

- Schaefer, G. H., Dutrey, A., Guilloteau, S., Simon, M., & White, R. J. 2009, *ApJ*, 701, 698
- Schreyer, K., Guilloteau, S., Semenov, D., et al. 2008, *A&A*, 491, 821
- Semenov, D., & Wiebe, D. 2011, *ApJS*, 196, 25
- Simon, M., Dutrey, A., & Guilloteau, S. 2000, *ApJ*, 545, 1034
- Skatrud, D. D., de Lucia, F. C., Blake, G. A., & Sastry, K. V. L. N. 1983, *J. Mol. Spectr.*, 99, 35
- Tafalla, M., Santiago-García, J., Hacar, A., & Bachiller, R. 2010, *A&A*, 522, A91
- Testi, L., Bacciotti, F., Sargent, A. I., Ray, T. P., & Eislöffel, J. 2002, *A&A*, 394, L31
- Thi, W.-F., van Zadelhoff, G.-J., & van Dishoeck, E. F. 2004, *A&A*, 425, 955
- Tilling, I., Woitke, P., Meeus, G., et al. 2012, *A&A*, 538, A20
- Troscompt, N., Faure, A., Wiesenfeld, L., Ceccarelli, C., & Valiron, P. 2009, *A&A*, 493, 687
- van den Ancker, M. E., de Winter, D., & Tjin A Djie, H. R. E. 1998, *A&A*, 330, 145
- van Leeuwen, F. 2007, *A&A*, 474, 653
- White, R. J., & Basri, G. 2003, *ApJ*, 582, 1109
- White, R. J., & Ghez, A. M. 2001, *ApJ*, 556, 265
- White, R. J., & Hillenbrand, L. A. 2004, *ApJ*, 616, 998
- Wilking, B. A., Marvel, K. B., Claussen, M. J., et al. 2012, *ApJ*, 753, 143
- Wolf, S., Padgett, D. L., & Stapelfeldt, K. R. 2003, *ApJ*, 588, 373
- Yokogawa, S., Kitamura, Y., Momose, M., & Kawabe, R. 2002, in 8th Asian-Pacific Regional Meeting, Volume II, eds. S. Ikeuchi, J. Hearnshaw, & T. Hanawa, 239

Appendix A: Comments on individual sources

FN Tau: the tentative detection of H₂CO is at an unusual velocity of -0.5 km s^{-1} .

CW Tau is dominated by confusion (see discussion in Appendix C). Despite strong confusion, line wings of ¹³CO could indicate a disk at velocity 6.2 km s^{-1} and with a line width of $3.3 \pm 0.4 \text{ km s}^{-1}$. CW Tau drives a bipolar outflow that can be traced in optical forbidden lines over $4''$ – $6''$ along both outflow directions (Hirth et al. 1994).

CIDA 1 (Briceno et al. 1993) is a late spectral type object (M5.5 White & Basri 2003), with weak 1.3 mm continuum emission (Schaefer et al. 2009). The line of sight towards CIDA 1 intercepts the same molecular cloud than that of CW Tau and is highly confused. The tentative fit of the ¹³CO line wing is not conclusive on the presence of a disk.

BP Tau harbors a small (120 AU radius) disk (Dutrey et al. 2003) and strong confusion in ¹²CO. No signal at all is detected in these new observations, but the sensitivity towards this source is lower than average.

DE Tau has relatively weak 1.3 mm continuum (36 mJy). There is some confusion in ¹³CO, but no evidence for disk emission.

RY Tau: the CN detection is marginal (3.5σ). A fit of a 3 km s^{-1} wide Gaussian to the ¹³CO spectrum also indicate a potential disk, at the 5σ level, but with a different velocity. RY Tau is a suspected close binary, with separation $>3 \text{ AU}$ (Bertout et al. 1999). Velocity measurements by Nguyen et al. (2012) indicate a possible SB1 with radial heliocentric velocity in the range 16.7 – 19.4 km s^{-1} , which is equivalent to 7.7 – 10.4 km s^{-1} in the LSR, and more consistent with the ¹³CO velocity. High resolution image at 1.3 mm by Isella et al. (2010a) indicate an inclination of 66° and a morphology consistent with a deficit of emission in the inner 15 AU.

T Tau is a triple system, with a compact ($\sim 60 \text{ AU}$) circumstellar disk around the single T Tau N (Akeson et al. 1998; Guilloteau et al. 2011). Its molecular environment is complex, and all the detected lines are most likely coming from an outflow or heated envelope, perhaps the outflowing cavity walls imaged in ¹³CO by Momose et al. (1996).

Haro 6-5 B, also known as FS Tau B, is a nearly edge-on, deeply embedded object. Confusion in ¹³CO is very strong. Previous interferometric measurements of ¹³CO $J = 1-0$ revealed a complex region (Dutrey et al. 1996). HST images indicate a 300 AU radius disk at high inclination, 70 – 80° (Krist et al. 1998; Padgett et al. 1999). FS Tau B possess a jet and a counterjet, as well as an optically visible cavity wall (Liu et al. 2012). Our combined detection of CN and H₂CO may indicate a compact, warm disk or some emission from an outflow or envelope. $5''$ resolution images in ¹³CO $J = 1-0$ with the NMA (Yokogawa et al. 2002) revealed a disk at $V_{\text{LSR}} \approx 7.0 \text{ km s}^{-1}$, with a kinematics dominated by rotation. They indicate motions compatible with Keplerian motions around a central star of $0.25 M_\odot$ only. Given the high confusion level, this value may

be unreliable. Our CN line width, though unprecise, suggests a higher stellar mass. The asymmetric H₂CO spectrum may be affected by confusion in the blueshifted part.

FT Tau is a deeply embedded, low luminosity star with unknown spectral type. A compact (60 AU) dust disk was resolved by Guilloteau et al. (2011), who also detected ¹²CO emission, suggesting a small disk at low inclination around a 0.7 – $1.0 M_\odot$ star. The clear detection of CN confirms the disk interpretation. ¹³CO emission from the disk may be present at redshifted velocities compatible with CN, but confusion makes any quantitative estimate impossible.

DG Tau is a well studied object, driving an optical microjet. The system inclination remain unclear: between 38 and 45° from the jet (Pyo et al. 2003; Eisloffel & Mundt 1998), and 20 to 32° from the dust disk (Isella et al. 2010a; Guilloteau et al. 2011). Images in ¹³CO (2–1) (Testi et al. 2002) indicate a complex morphology, a large fraction of the emission coming from a remnant envelope (see also Kitamura et al. 1996). There is no clear evidence for Keplerian rotation. The relatively narrow lines of H₂CO and SO could originate from this remnant envelope. CN(2–1) was previously detected by Salter et al. (2011)⁵, who modeled this as coming from a Keplerian disk. Our CN line width is consistent with the measurement of Salter et al. (2011), but the large derived outer radius, combined with the complex morphology, suggests CN is most likely coming from the outflow or the remnant envelope.

DG Tau B is a totally obscured object, driving a powerful one-sided molecular outflow (Mitchell et al. 1997). High inclination (64 – 75° , see Guilloteau et al. 2011; Eisloffel & Mundt 1998) however yield moderate line-of-sight velocities for the outflow. The rich spectrum may originate from the outflow, but CN lacks the narrow component detected in H₂CO and C¹⁷O, which is presumably due to the molecular cloud.

Haro 6-10 (also known as GV Tau) is a close binary, with two compact ($<30 \text{ AU}$), optically thick, circumstellar disks (Guilloteau et al. 2011), but no known circumbinary disk. The circumstellar disks are misaligned and the system is embedded in a common envelope (Roccatagliata et al. 2011). H₂O maser emission has been recently reported, and suggest that the Southern component is itself a close binary (Wilking et al. 2012). As for DG Tau B, the CN line is much wider than those of H₂CO and C¹⁷O. The prominent red wing in ¹³CO is likely to trace the outflow.

IQ Tau was observed in ¹²CO by Schaefer et al. (2009), who did not detect any significant emission with the IRAM Plateau de Bure interferometer at $5''$ resolution. The CN emission exhibits the clear signature of Keplerian rotation (although the expected double peaked aspect is reduced because of the hyperfine component blending). CN is apparently stronger than ¹³CO in this source. A tentative fit of a disk component to the ¹³CO spectrum suggest the redshifted emission may still be masked by the cloud.

⁵ Although their Figs. 10 and 12 mark it as the 3–2 transition.

LkHa 358: ^{13}CO is heavily confused. A small molecular disk was reported from interferometric measurements by [Schaefer et al. \(2009\)](#) from ^{12}CO emission. An attempt to fit a disk component to the ^{13}CO line wings is consistent with this interpretation, provided ^{13}CO has significant optical depth (>2 on average). The narrow emission from C^{17}O most likely comes from the surrounding cloud, as the $\sim 3.5\sigma$ signal from H_2CO .

HH 30: [Pety et al. \(2006\)](#) had previously imaged the ^{13}CO emission from this emblematic edge-on object. The narrow line from C^{17}O likely comes from the cloud, as the $\sim 3\sigma$ signal from H_2CO .

HL Tau is the archetype of the deeply embedded, outflow driving sources. The redshifted side of the outflow is known to be brighter ([Cabrit et al. 1996](#); [Monin et al. 1996](#)). From the line profiles, C^{17}O , H_2CO and especially SO (which is significantly redshifted), must come from the outflow. However, the CN line is much narrower and exhibit a systemic velocity of 4.7 km s^{-1} , and thus could be a pure disk tracer.

HK Tau is a binary star, with one component exhibiting an edge-on disk ([McCabe et al. 2011](#)). The relatively broad CN line is consistent with emission from this edge-on disk around HK Tau B. The blue shifted side of the disk may also have been detected in ^{13}CO .

Haro 6-13, also known as V 806 Tau, was imaged in ^{12}CO by [Schaefer et al. \(2009\)](#), who based on agreement in position angle between CO and dust emission, attributed the emission to a disk of at least 180 AU radius. $\text{HCO}^+ 3-2$ emission has been detected by [Salter et al. \(2011\)](#). The H_2CO spectra are complex, as the C^{17}O one, and perhaps result of superposition of relatively broad emission with a narrow (0.5 km s^{-1}) absorption feature.

GG Tau was included as a reference source in our sample. Our results agree with the initial detections of [Dutrey et al. \(1997\)](#). H_2CO is well detected in the combined spectrum.

UZ Tau E is a spectroscopic binary part of the UZ Tau hierarchical quadruple system. The CO disk was detected by [Simon et al. \(2000\)](#), who found an inclination of 55° and an outer radius of 300 AU. Our derived radius from CN is in excellent agreement with this value. ^{13}CO emission from the disk is also detected, in the line wings, but still exhibits confusion.

IRAS 04302+2247 (the Butterfly star [Wolf et al. 2003](#)), is an edge-on system. Recent IRAM interferometric measurements indicate a stellar mass of order $1.6 M_\odot$ and a disk radius of 260 AU ([Dutrey et al.](#), in prep.). Although this source exhibits a large $\text{H}_2\text{CO}/\text{CN}$ ratio, which we in general attribute to outflows, the H_2CO and SO emissions come from the disk. From the hyperfine ratios, CN appears potentially optically thick in this source, in which case the emission must be dominated by smaller radii. The rather large linewidth concurs with this interpretation.

DL Tau was imaged in ^{12}CO by [Simon et al. \(2000\)](#) who pointed out the strong confusion making the inclination derivation unreliable. Confusion is also large in ^{13}CO , masking all the emission

except for the red-shifted wing. Like IQ Tau, DL Tau shows strong, double peaked line profile in CN. The outer radius derived from CN is consistent with the value quoted by [Simon et al. \(2000\)](#) for CO. H_2CO is also detected.

AA Tau: CN is clearly detected, and weak emission is also visible in ^{13}CO , despite confusion. However, the disk contribution in ^{13}CO is much smaller than the intensity reported by [Greaves \(2005\)](#) (0.6 K km s^{-1} at JCMT, i.e. 12 Jy km s^{-1}), which must have included cloud emission. CN in AA Tau was discovered by [Öberg et al. \(2010\)](#). We recover only about half of their quoted flux (1.7 Jy km s^{-1}), and our derived velocity suggests that the blue-shifted part of the CN spectrum is masked by confusion, like the ^{13}CO one.

DN Tau is very similar to DL Tau and IQ Tau, with CN stronger than ^{13}CO . [Schaefer et al. \(2009\)](#) failed to detect ^{12}CO from this object with the IRAM interferometer, again presumably because of strong confusion with the cloud.

DO Tau shows clear CN detection (4σ), but the line width is poorly constrained. The line can be narrow, so (positive) contamination by the cloud is not fully excluded. Identification of a disk component in ^{13}CO is difficult, as the redshifted side is dominated by the cloud.

HV Tau C, like HK Tau B, is a compact (80 AU radius) edge on disk in a multiple system, here a hierarchical triple. ^{12}CO emission from the disk was resolved by [Duchêne et al. \(2010\)](#) with the IRAM array. The broad CN line ($\Delta V = 6 \text{ km s}^{-1}$) is consistent with an origin in a compact disk. The CN flux suggests a somewhat larger radius (300 AU in Table 5), or equivalently, non negligible optical depth. The observed hyperfine ratios are indeed compatible with substantial optical depth, $\tau = 7.0 \pm 2.7$, which would also yield a lower line width, $4.2 \pm 0.6 \text{ km s}^{-1}$. ^{13}CO emission from the disk produces the line wings visible in Fig. B.26

Haro 6-33 (also known as IRAS 04385+2550) was detected in ^{12}CO by [Schaefer et al. \(2009\)](#), who interpreted the emission as coming from a Keplerian disk, despite strong confusion. There is also substantial cloud contamination in ^{13}CO , but CN and H_2CO are detected. The derived disk radius in CN is in good agreement with the ^{12}CO result.

DQ Tau exhibits huge confusion, and no detection at all.

DR Tau was reported as tentatively detected in CN(2-1) by [Salter et al. \(2011\)](#) at a velocity of 11 km s^{-1} with an integrated flux of $3.5 \pm 1.3 \text{ Jy km s}^{-1}$. Our spectrum shows no line at all, with a 3σ upper limit on the flux of 1.4 Jy km s^{-1} . Confusion with the cloud is huge in ^{13}CO : only the red wing between 10 and 11 km s^{-1} may be attributable to a disk component.

DS Tau shows no apparent confusion. A weak (4σ) line is detected when combining both o- H_2CO transitions, with a velocity (6.0 km s^{-1}) and linewidth (3 km s^{-1}) consistent with disk emission, but no CN or ^{13}CO .

UY Aur is a 0.8'' separation binary system. The ^{13}CO line is strong, and consistent with an origin in the complex circumbinary structure imaged by Duvert et al. (2000). There is a 4σ detection of H_2CO with a compatible kinematics.

AB Aur: the strong ^{13}CO line emanates from a combination of the disk/ring structure imaged by Piétu et al. (2005) and the surrounding envelope. The clear detection of C^{17}O confirms the large CO content of this source. H_2CO is convincingly detected, confirming the result of Fuente et al. (2010) using the para- H_2CO $3_{0,3}-2_{0,2}$ line at 218.2 GHz. However, we find no evidence at all for CN or SO from the disk, which were claimed to be detected by these authors. We only have a narrow (0.4 km s^{-1}), 3.5σ feature in CN(2–1) at a velocity consistent with cloud emission. The CN (1–0) line quoted by Fuente et al. (2010) must have been residual emission from the cloud. For SO, they report a line intensity of 26 mK km s^{-1} for the 3_4-2_3 line, and 60 mK km s^{-1} for the 5_6-4_5 transitions, while we obtain a 3σ upper limit of 21 mK km s^{-1} for the 5_4-4_3 using the AB Aur velocity and line widths. Note that Fuente et al. (2010) used a larger throw ($120''$) than us in the wobbler switching, so that their results are more susceptible to residual emission from the envelope.

SU Aur: despite confusion with the cloud, the ^{13}CO spectrum exhibits a broad component compatible with emission from a disk. No other molecule is detected. SU Aur is a strong X-ray source (Franciosini et al. 2007). Near IR imaging indicates a highly inclined disk ($\approx 65^\circ$) and outflow cavity walls (Akeson et al. 2002; Chakraborty & Ge 2004).

MWC 480 was included here as a reference source in our sample. It has been extensively studied with the IRAM mm array (Piétu et al. 2007; Chapillon et al. 2012). We find the double peaked ^{13}CO profile characteristic of an isolated Keplerian disk. CN emission is in excellent agreement with the interferometric results of Chapillon et al. (2012). The detection of C^{17}O for the first time in this source confirms the significant CO abundance in this object. Note that, as expected, the C^{17}O profile is apparently larger than the ^{13}CO one.

CB26 is a deeply embedded, edge-on object driving an unusual outflow (Launhardt et al. 2009) in an isolated Bok globule. Like in HL Tau, we detect here strong H_2CO and SO emission, but only a weak CN line. If interpreted by disk emission, the CN line is consistent with a disk size about 250 AU.

CIDA 8 has weak continuum emission and no CO disk from interferometric measurements of Schaefer et al. (2009). Cloud contamination exists, but appears limited to a very narrow velocity range. There is a surprising detection of H_2CO just outside the range visibly contaminated in ^{13}CO , but with a narrow line width which suggests it originates from a cloud.

CIDA 11 shows no detection at all. It was also not detected in continuum and CO by Schaefer et al. (2009).

RW Aur is a binary system that was imaged in ^{12}CO by Cabrit et al. (2006), who find evidence for a very small (50 AU radius) disk, but did not detect ^{13}CO emission. Our negative result is consistent with their findings.

MWC 758 is a $1.8 M_\odot$ star surrounded by a disk where CO is apparently depleted and mostly optically thin (Chapillon et al. 2008), despite high temperatures (30 K). We find a relatively weak line of ^{13}CO , consistent with this interpretation. No other molecule is detected: the marginal signal in C^{17}O is not at the expected disk velocity. The limited CO opacity could be related to the large cavity detected by Isella et al. (2010b) in continuum.

CQ Tau is a “twin” of MWC 758, also exhibiting a warm ($>50 \text{ K}$) disk with optically thin CO emission (Chapillon et al. 2008), but its continuum emission is strongly centrally peaked (Banzatti et al. 2011; Guilloteau et al. 2011). Although different distances are often quoted based on Hipparcos parallax, these differences are not significant and Chapillon et al. (2008) argue that both CQ Tau and MWC 758 are also located at 140 pc. We also detect ^{13}CO with a similar intensity than in MWC 758. H_2CO is detected at the 5σ level, with kinematic parameters quite consistent with those derived from ^{13}CO . However, we find no evidence for CN. Our 3σ limit of $0.28 \text{ Jy km s}^{-1}$ is marginally consistent with the flux of $0.22 \pm 0.11 \text{ Jy km s}^{-1}$ reported by Öberg et al. (2010).

HD 163296 is an isolated Herbig Ae star located at 120 pc (van Leeuwen 2007). It harbours a large ($\sim 550 \text{ AU}$) CO disk inclined at about 45° (Isella et al. 2007), and has been extensively studied in CO isotopologues, including C^{17}O (Qi et al. 2011). CN $N = 3-2$ was detected by Thi et al. (2004). The strong CN $N = 2-1$ emission is compatible with an optically thin line. The outer radius in Table 5 is slightly larger than that measured from CO. The discrepancy may have several origins. First, as the star is very luminous, CN may be in a warmer region. Second, Hughes et al. (2011) report a rather large turbulence level ($\approx 0.3 \text{ km s}^{-1}$) from CO measurements, larger than assumed. We also report the first detection of H_2CO , through the ortho- H_2CO $3_{13}-2_{12}$ transition. Comparison of our ^{13}CO spectrum to the interferometric result of Qi et al. (2011) suggest some contamination near $2-4 \text{ km s}^{-1}$ (and also 13 km s^{-1} as in the ^{12}CO spectra of Qi et al. 2011).

Appendix B: Spectra for individual sources

This appendix displays the spectra towards the various sources. For each source, the top panel shows the ^{13}CO $J = 2-1$ spectrum. The continuous red line, if present, is a Gaussian fit obtained after masking the confused velocity range. The bottom panel displays on a common scale from top to bottom the spectra of: ^{13}CO $J = 2-1$ (with fit as in top panel), C^{17}O $J = 2-1$, CN $N = 2-1$, ortho H_2CO $3_{13}-2_{12}$, ortho H_2CO $3_{12}-2_{11}$, the average of both o- H_2CO transitions, and SO 5_4-4_3 , arbitrarily shifted in intensity to avoid overlap. The intensity scale is antenna temperature (T_A^* in K): conversion to flux density can be obtained using a factor of 9 Jy/K .

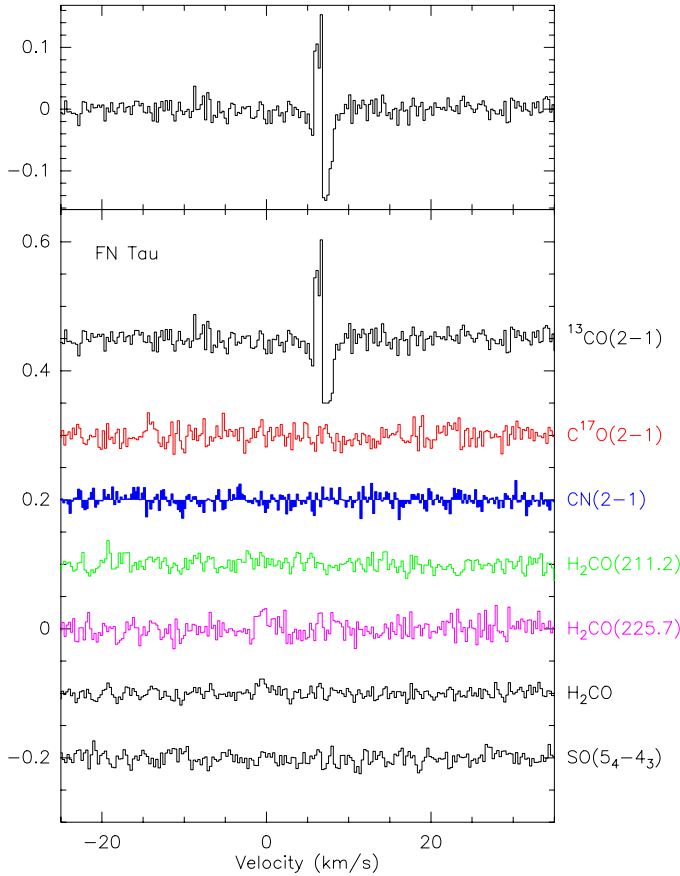


Fig. B.1. Spectra of the observed transitions towards FN Tau.

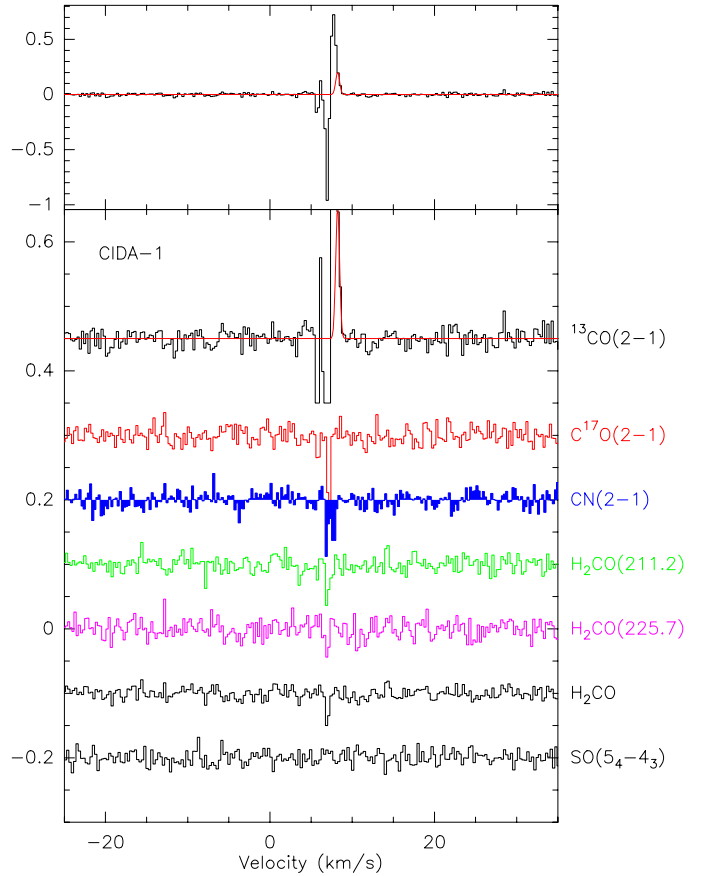


Fig. B.3. Spectra of the observed transitions towards CIDA-1.

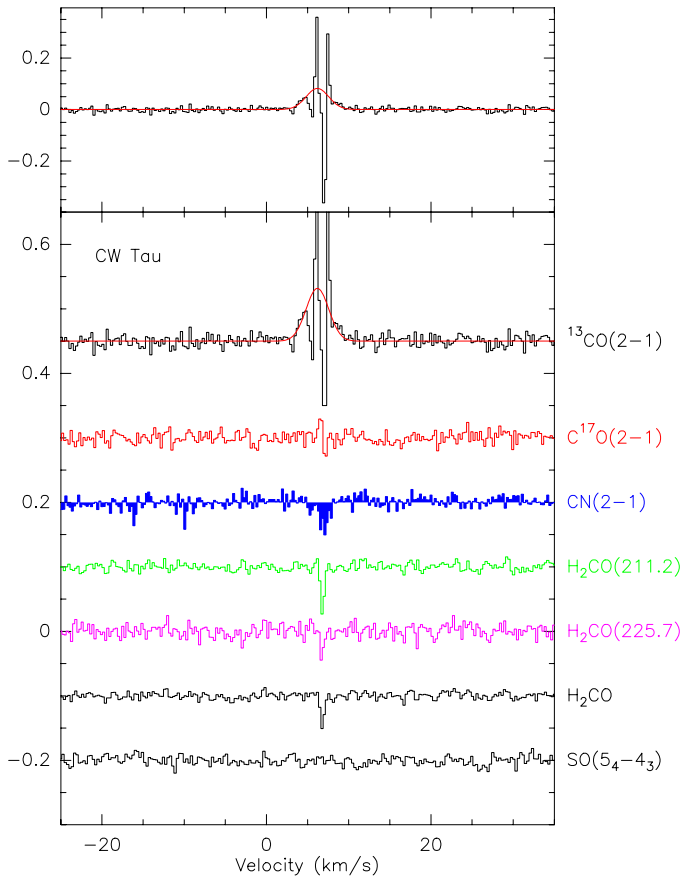


Fig. B.2. Spectra of the observed transitions towards CW Tau.

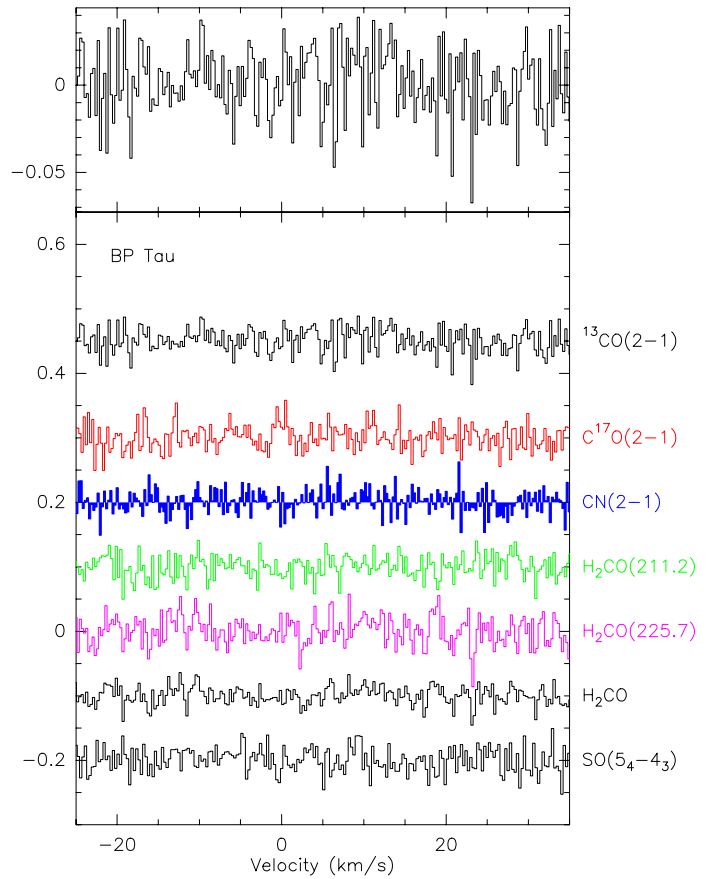


Fig. B.4. Spectra of the observed transitions towards BP Tau.

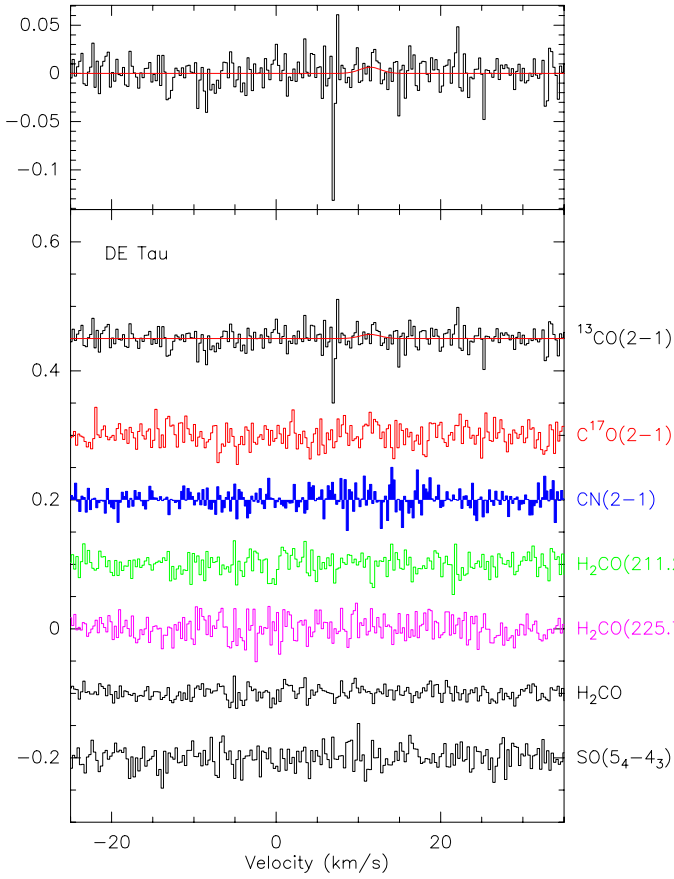


Fig. B.5. Spectra of the observed transitions towards DE Tau.

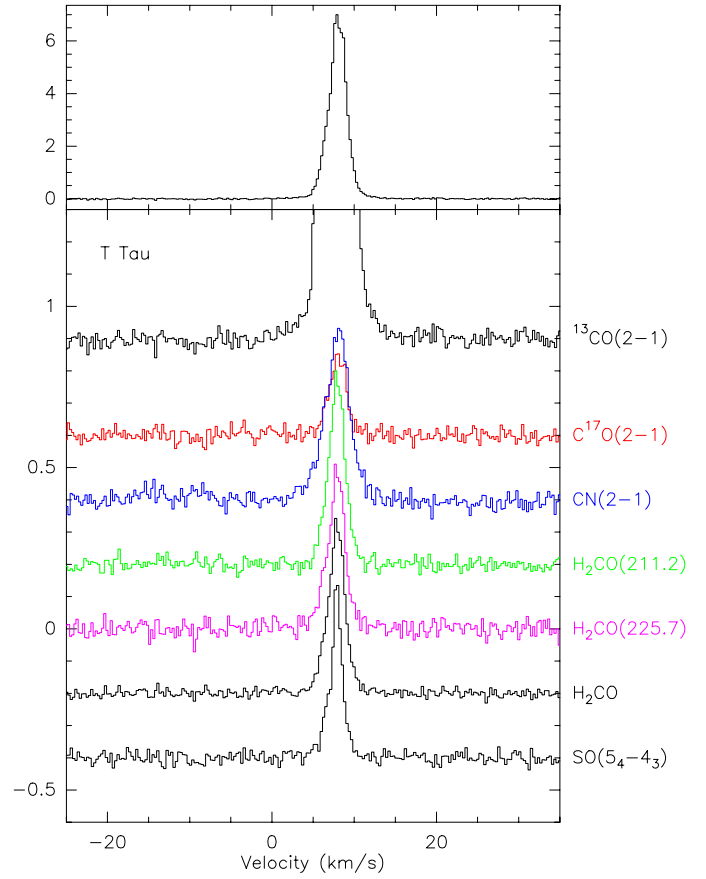


Fig. B.7. Spectra of the observed transitions towards T Tau.

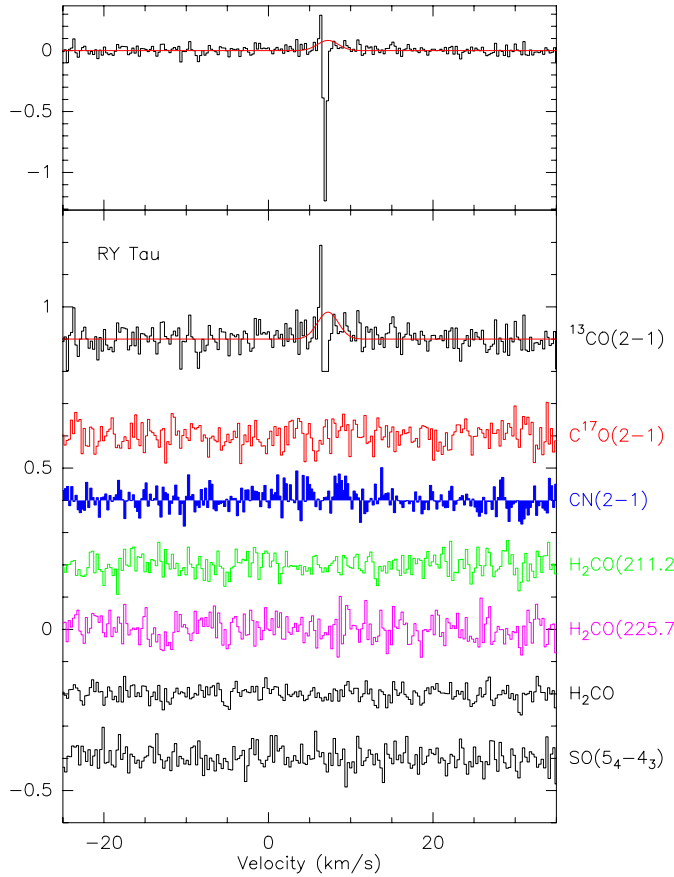


Fig. B.6. Spectra of the observed transitions towards RY Tau.

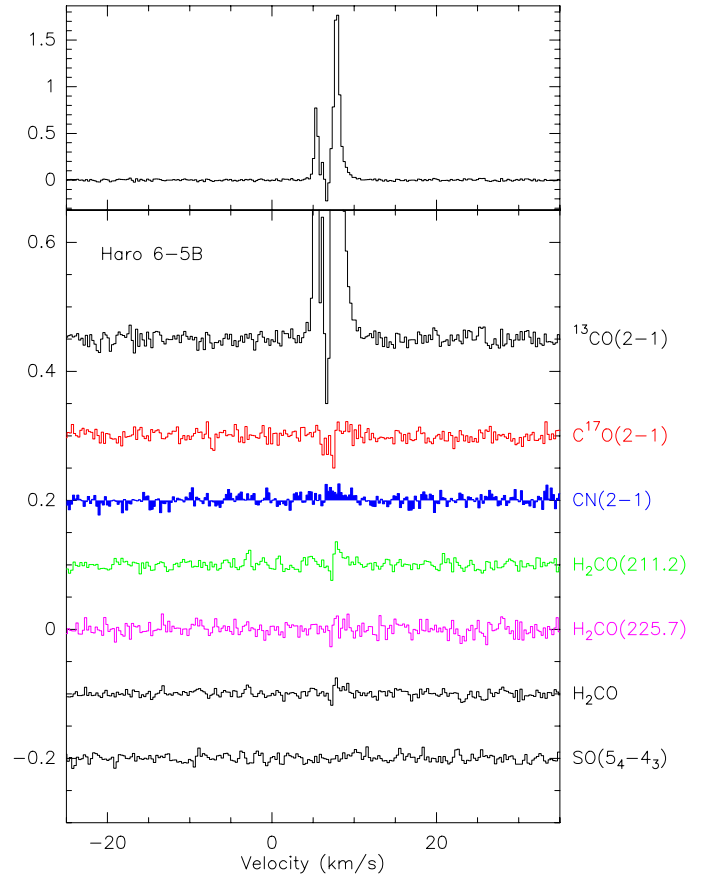


Fig. B.8. Spectra of the observed transitions towards Haro 6-5 B.

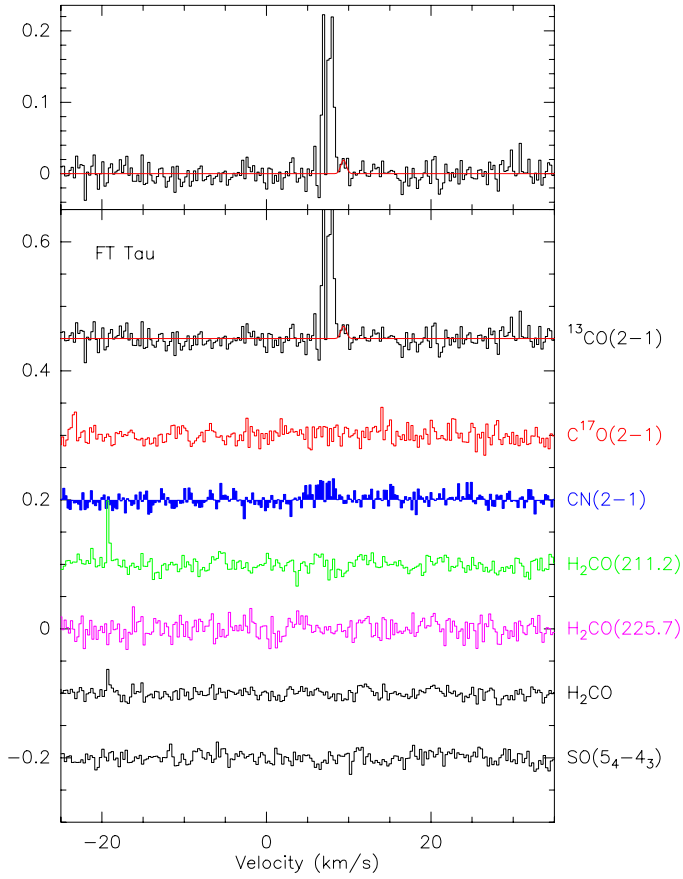


Fig. B.9. Spectra of the observed transitions towards FT Tau.

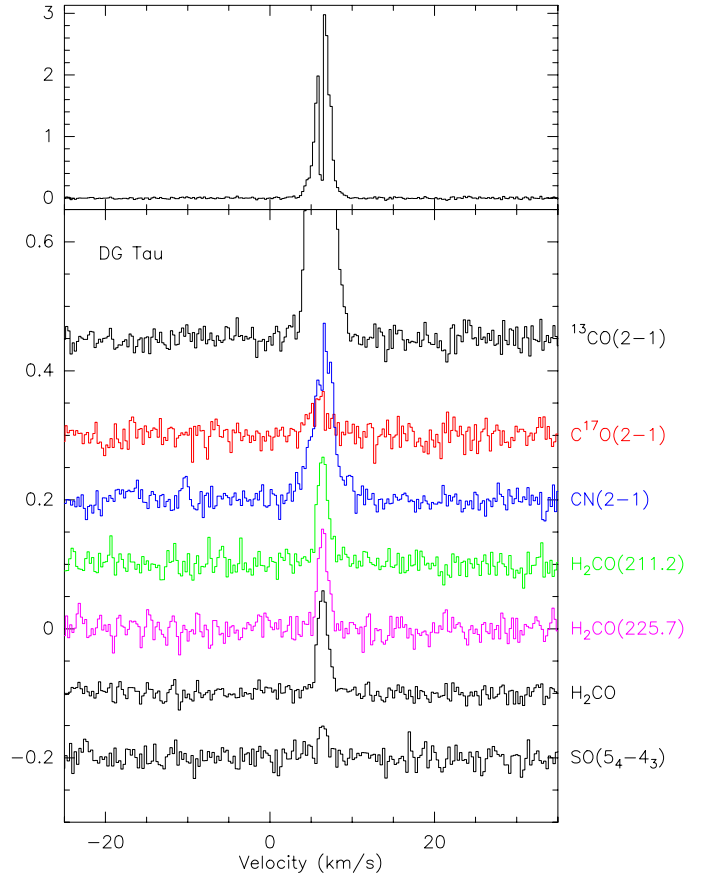


Fig. B.11. Spectra of the observed transitions towards DG Tau.

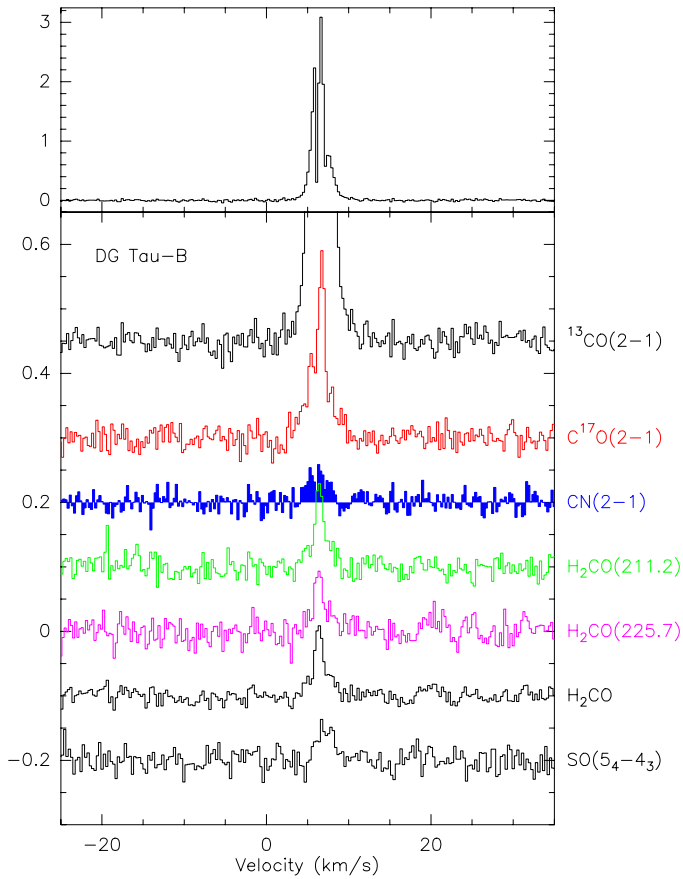


Fig. B.10. Spectra of the observed transitions towards DG Tau B.

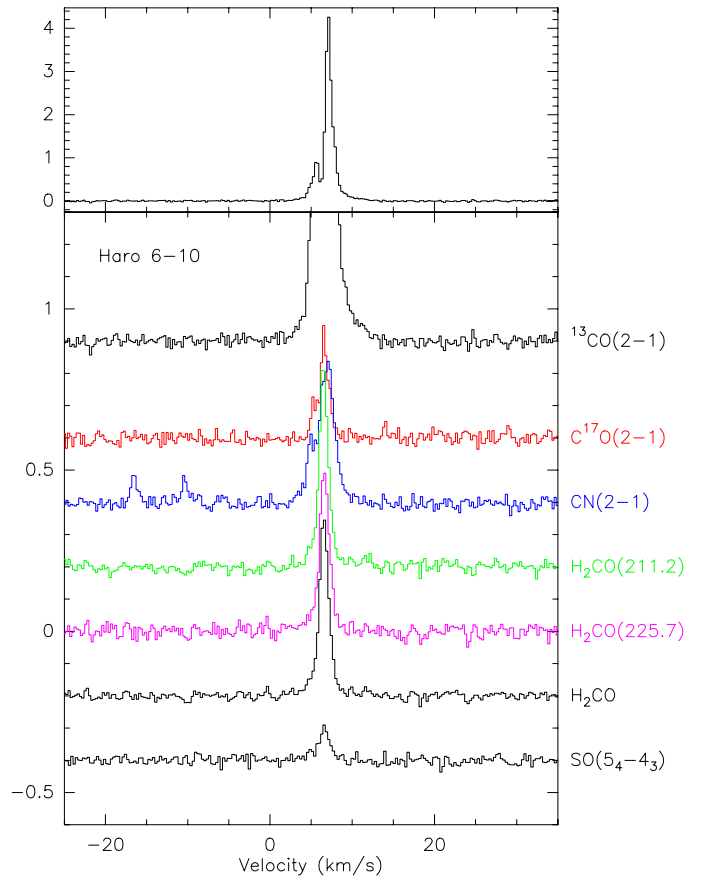


Fig. B.12. Spectra of the observed transitions towards Haro 6-10.

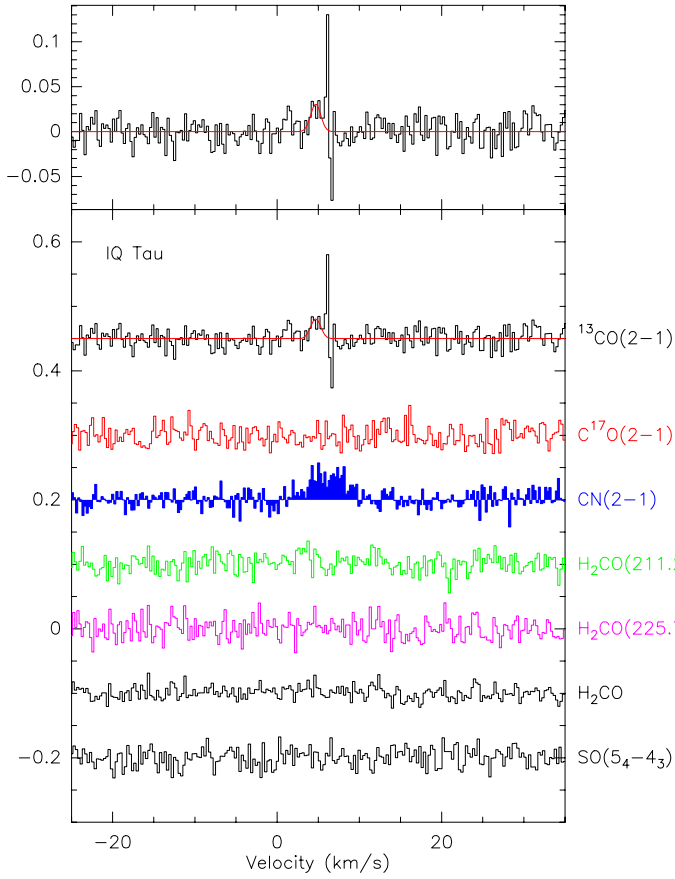


Fig. B.13. Spectra of the observed transitions towards IQ Tau.

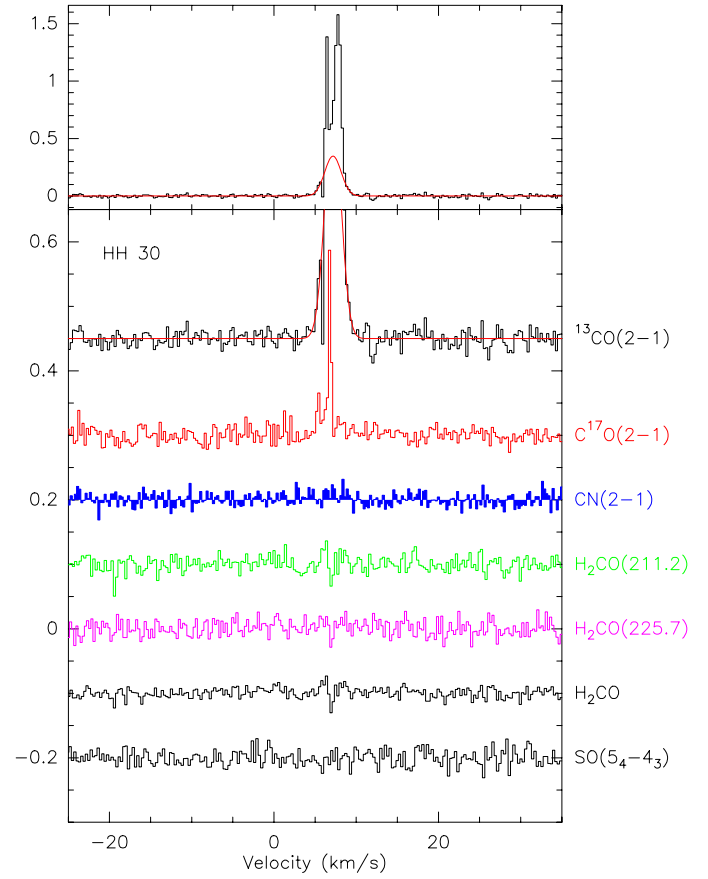


Fig. B.15. Spectra of the observed transitions towards HH 30.

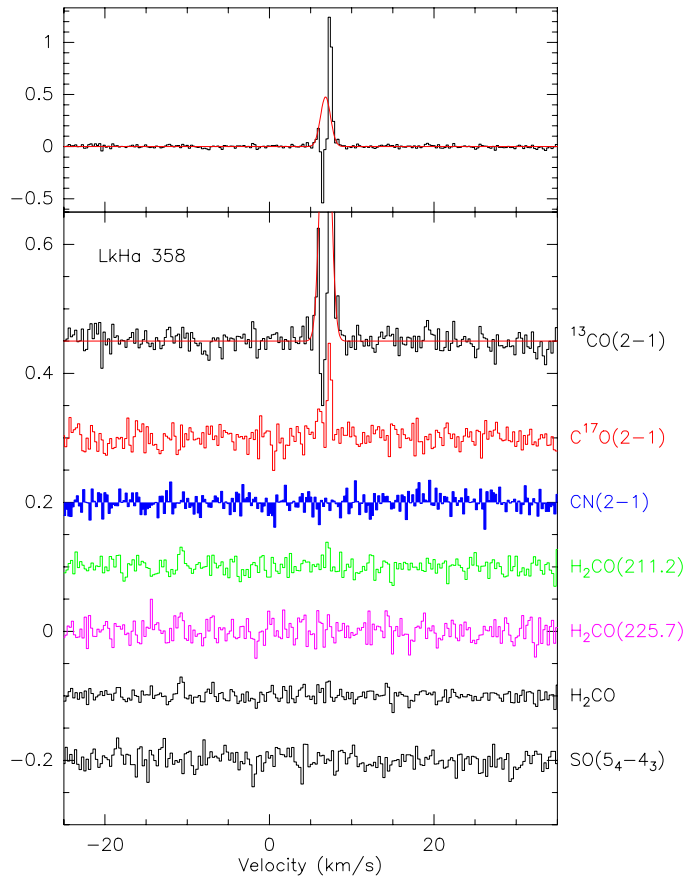


Fig. B.14. Spectra of the observed transitions towards LkHa 358.

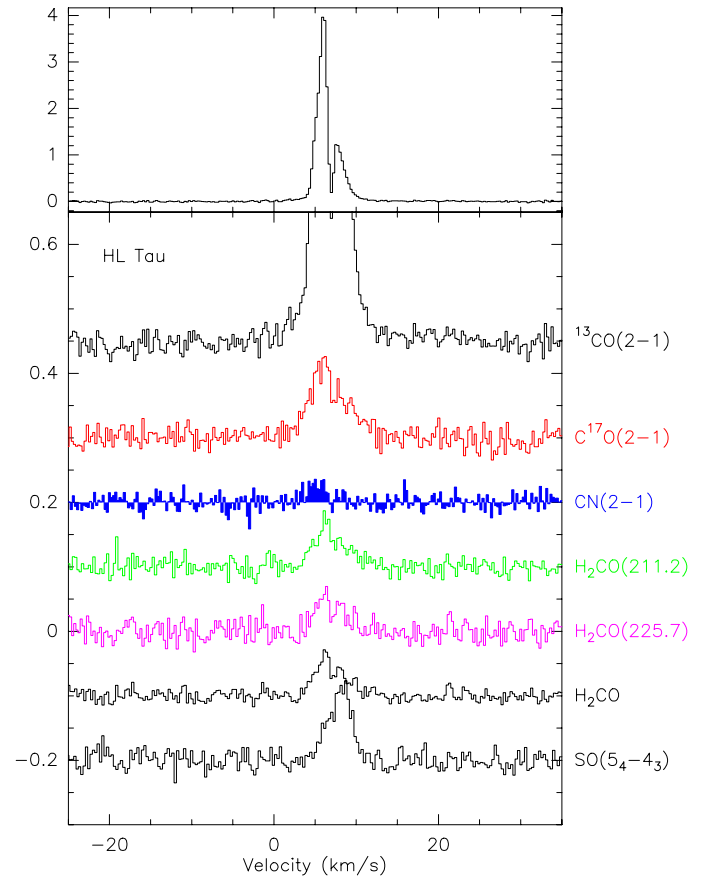


Fig. B.16. Spectra of the observed transitions towards HL Tau.

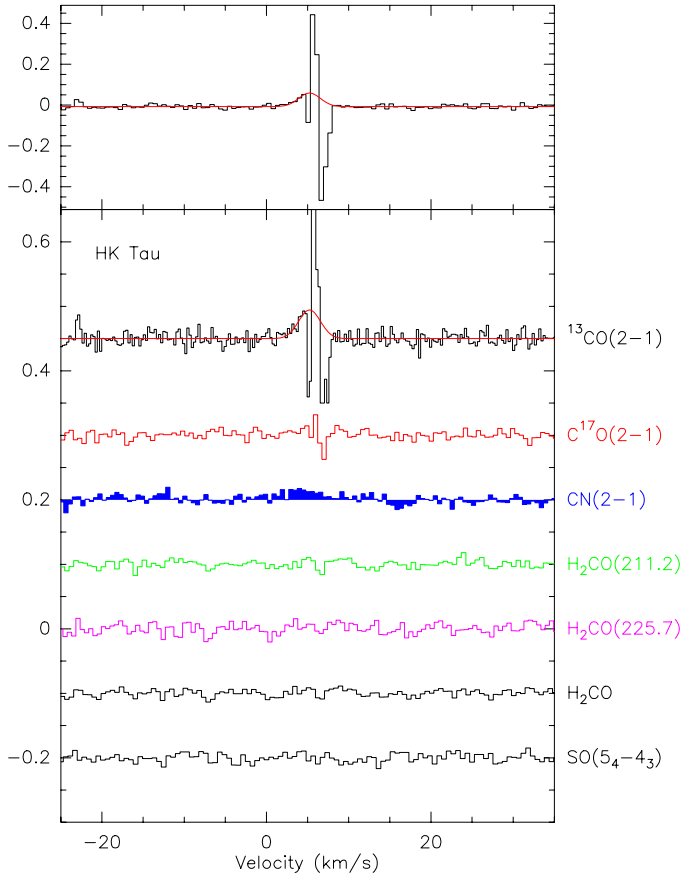


Fig. B.17. Spectra of the observed transitions towards HK Tau.

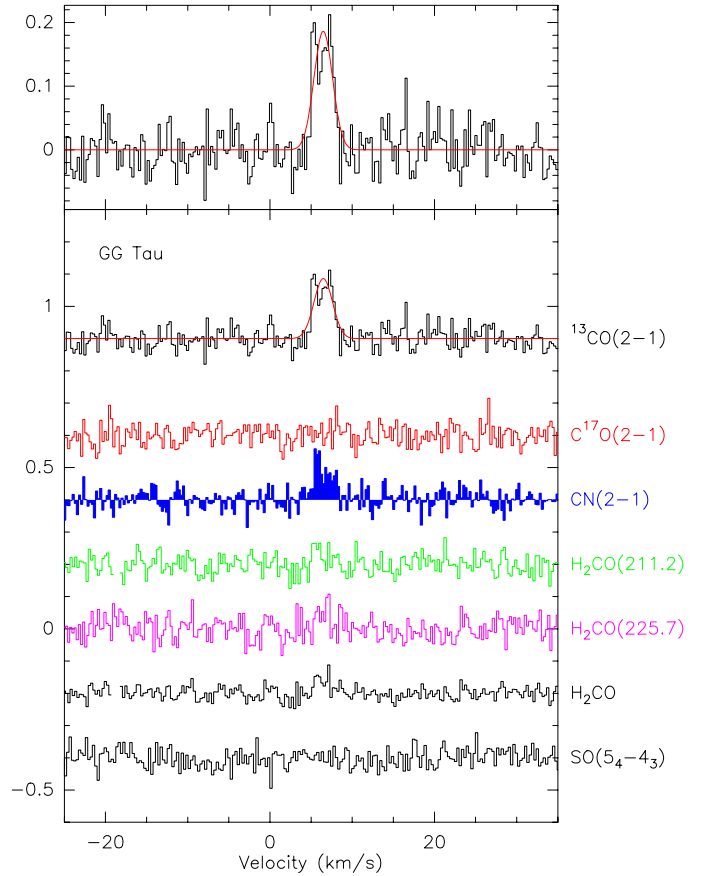


Fig. B.19. Spectra of the observed transitions towards GG Tau.

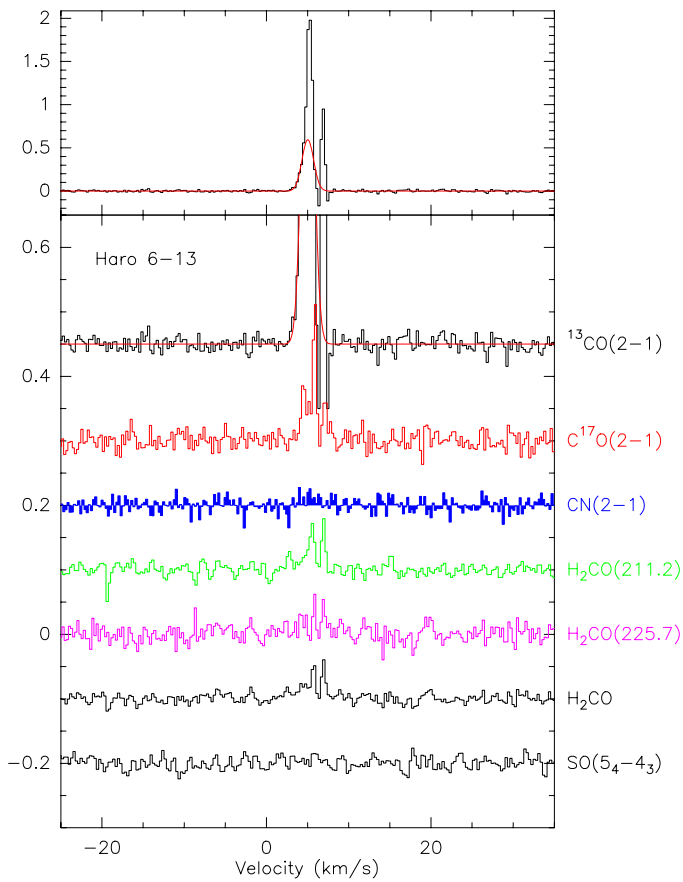


Fig. B.18. Spectra of the observed transitions towards Haro 6-13.

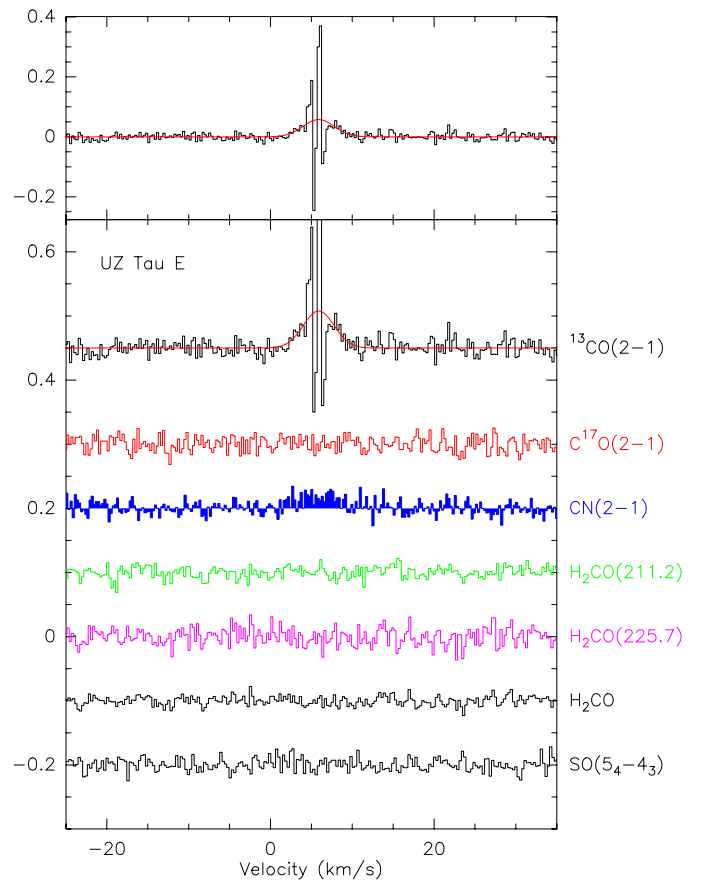


Fig. B.20. Spectra of the observed transitions towards UZ Tau E.

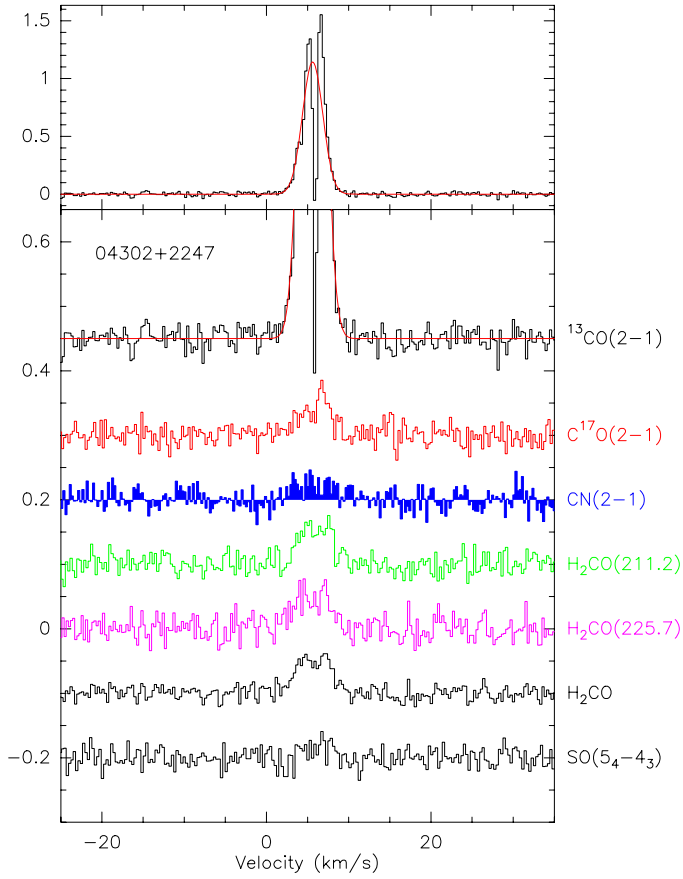


Fig. B.21. Spectra of the observed transitions towards 04302+2247.

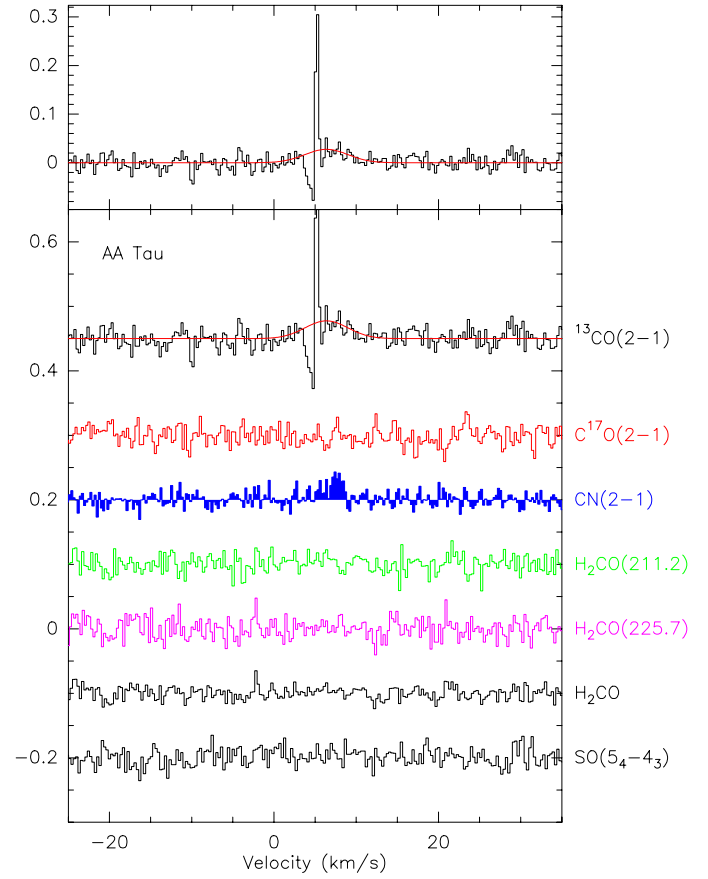


Fig. B.23. Spectra of the observed transitions towards AA Tau.

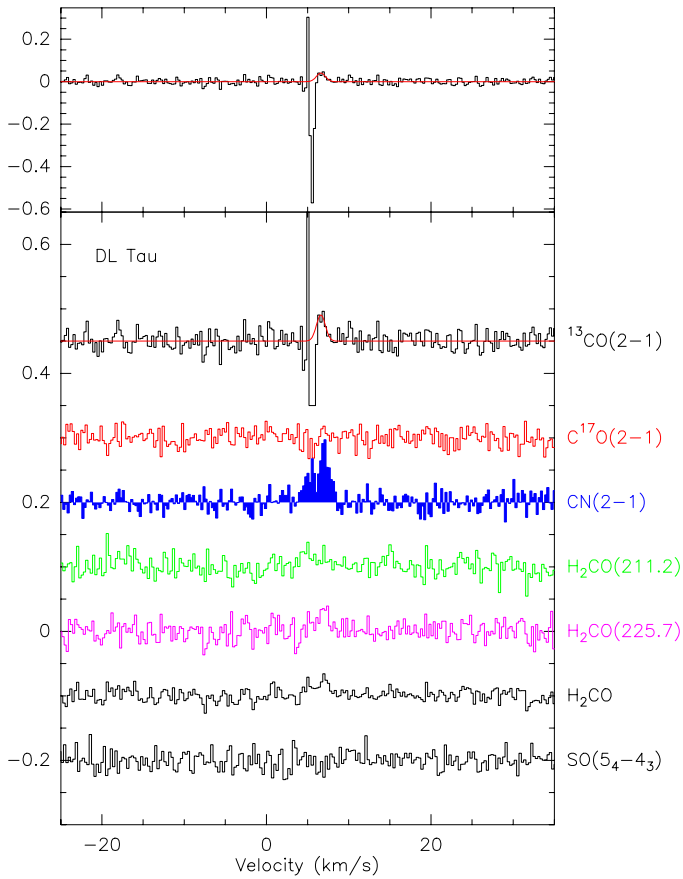


Fig. B.22. Spectra of the observed transitions towards DL Tau.

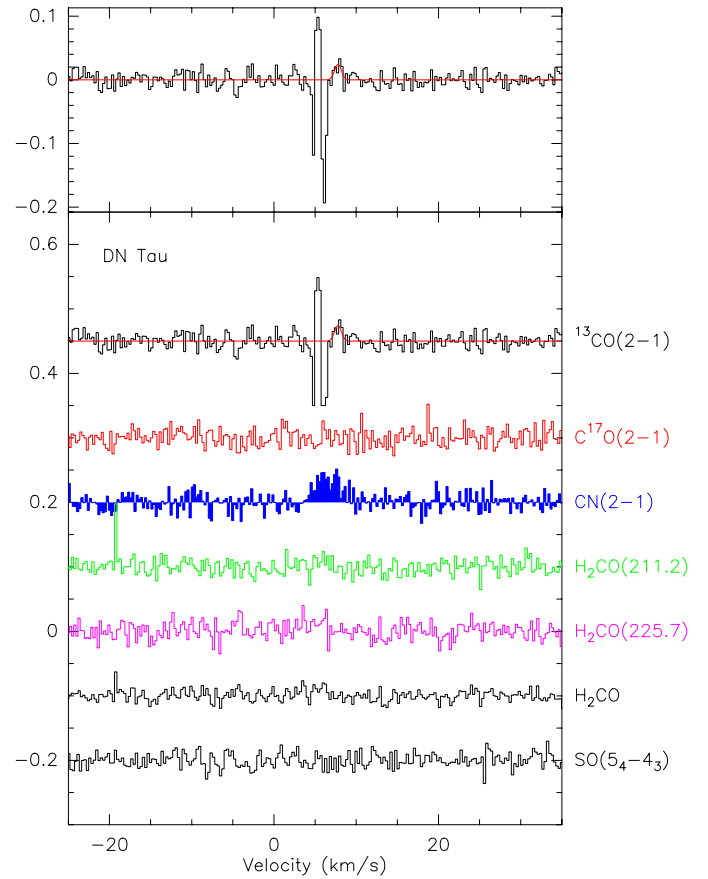


Fig. B.24. Spectra of the observed transitions towards DN Tau.

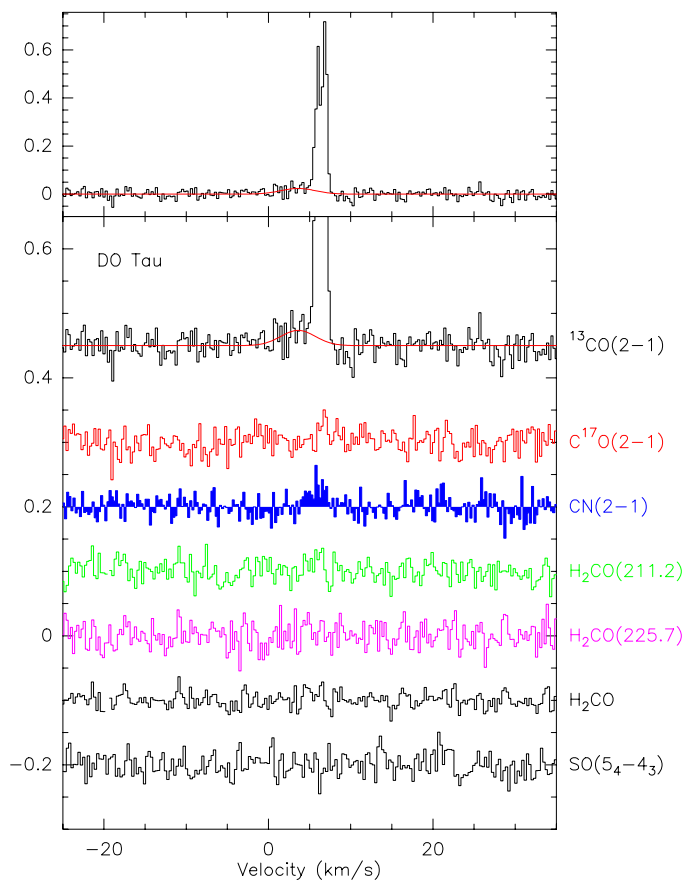


Fig. B.25. Spectra of the observed transitions towards DO Tau.

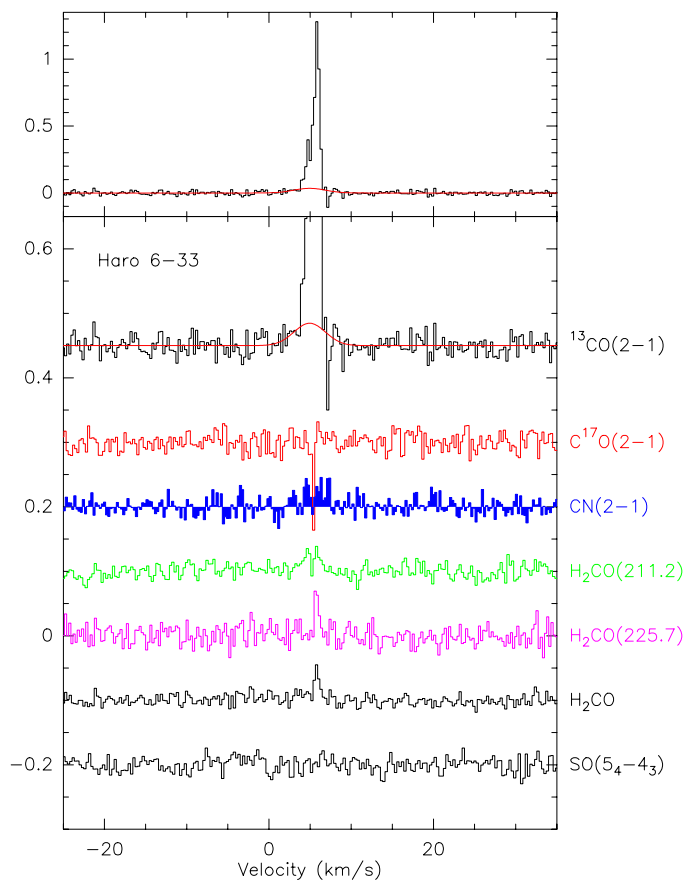


Fig. B.27. Spectra of the observed transitions towards Haro 6-33.

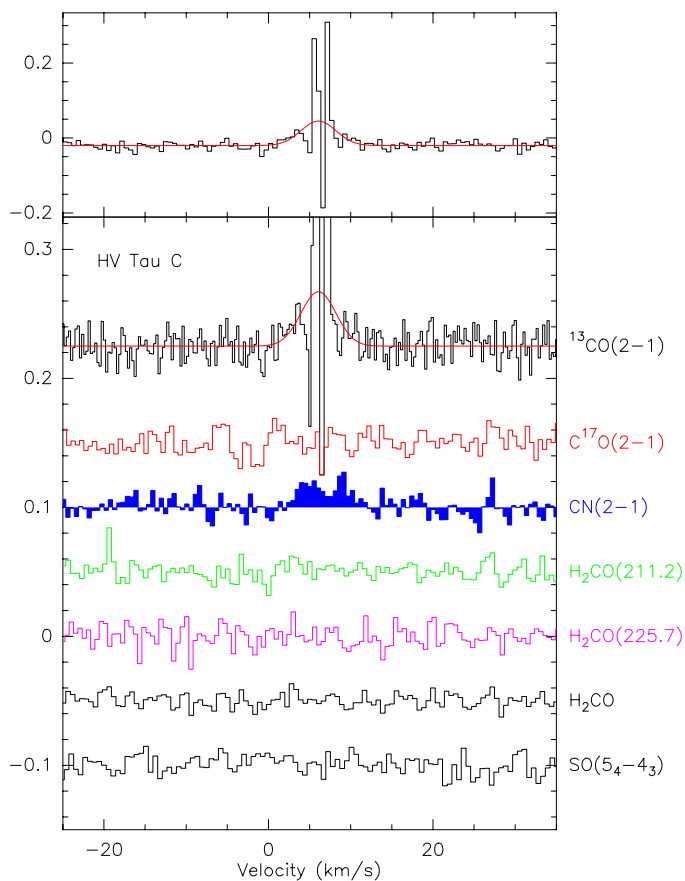


Fig. B.26. Spectra of the observed transitions towards HV Tau C.

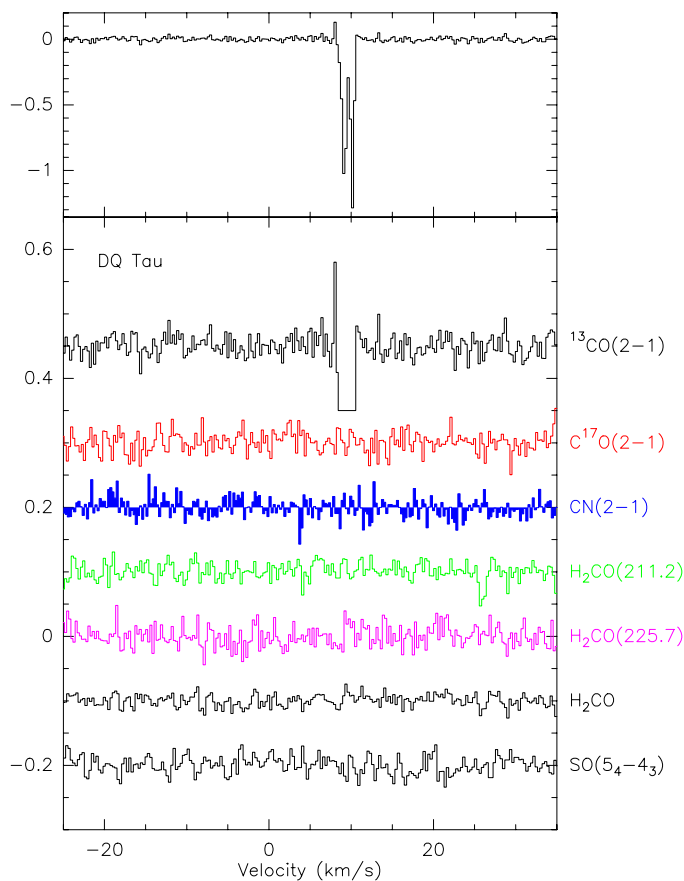


Fig. B.28. Spectra of the observed transitions towards DQ Tau.

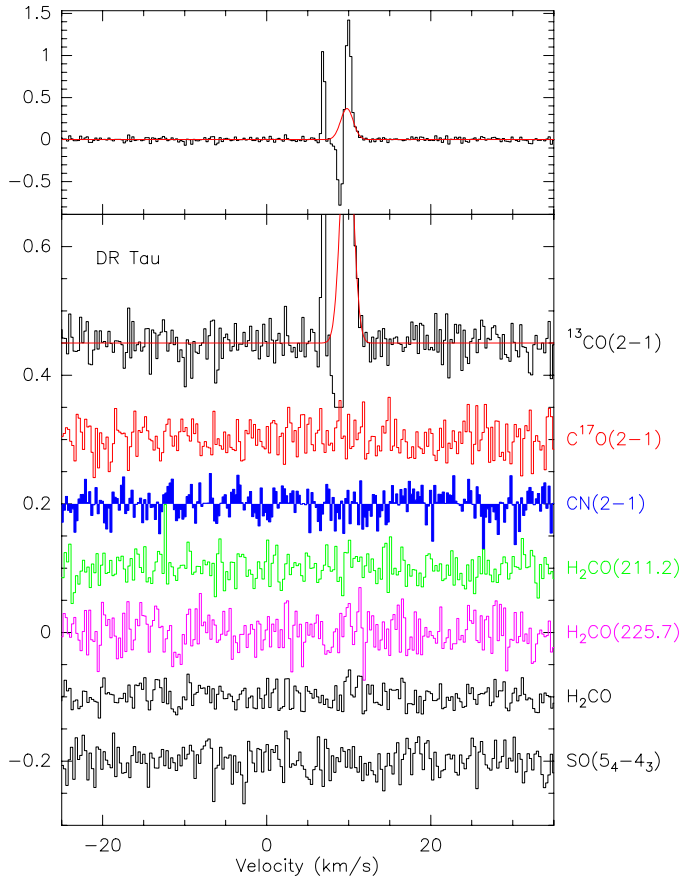


Fig. B.29. Spectra of the observed transitions towards DR Tau.

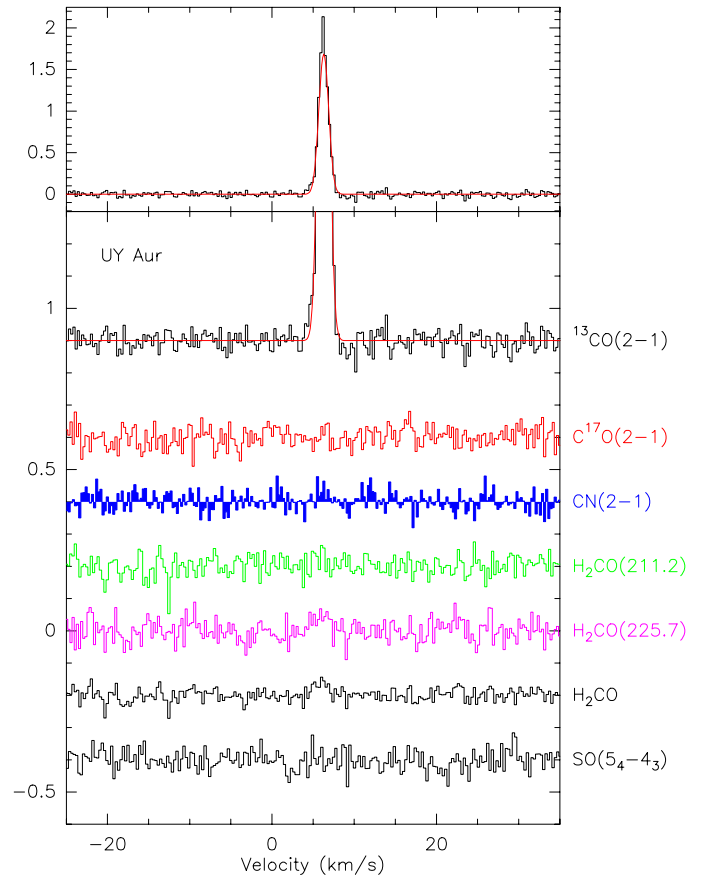


Fig. B.31. Spectra of the observed transitions towards UY Aur.

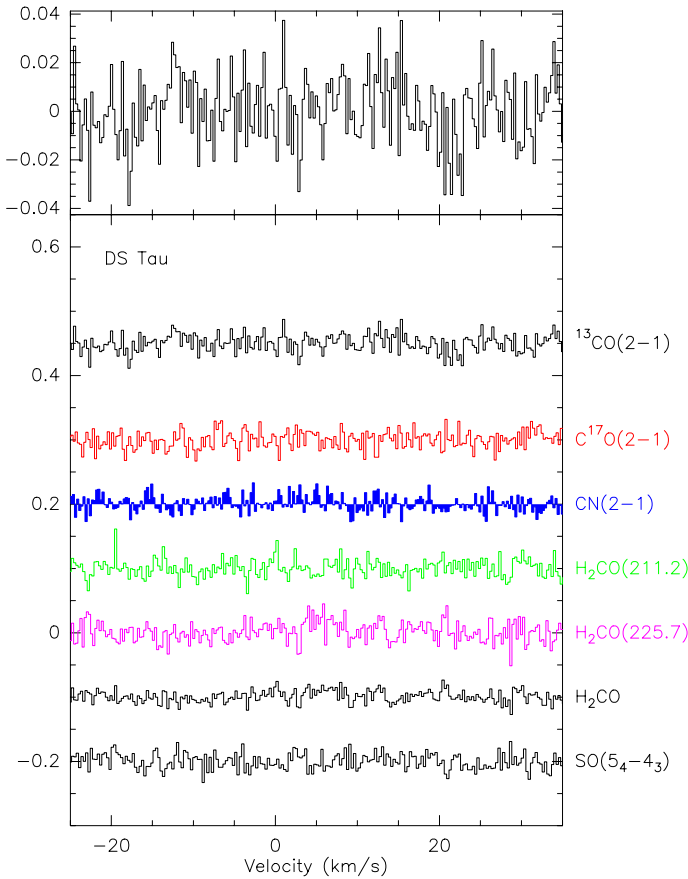


Fig. B.30. Spectra of the observed transitions towards DS Tau.

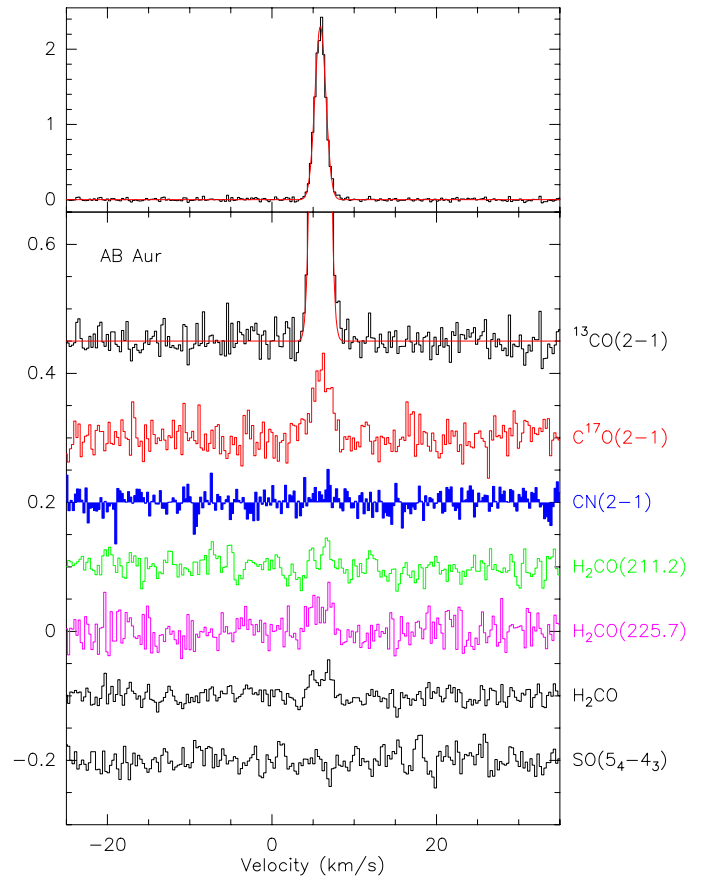


Fig. B.32. Spectra of the observed transitions towards AB Aur.

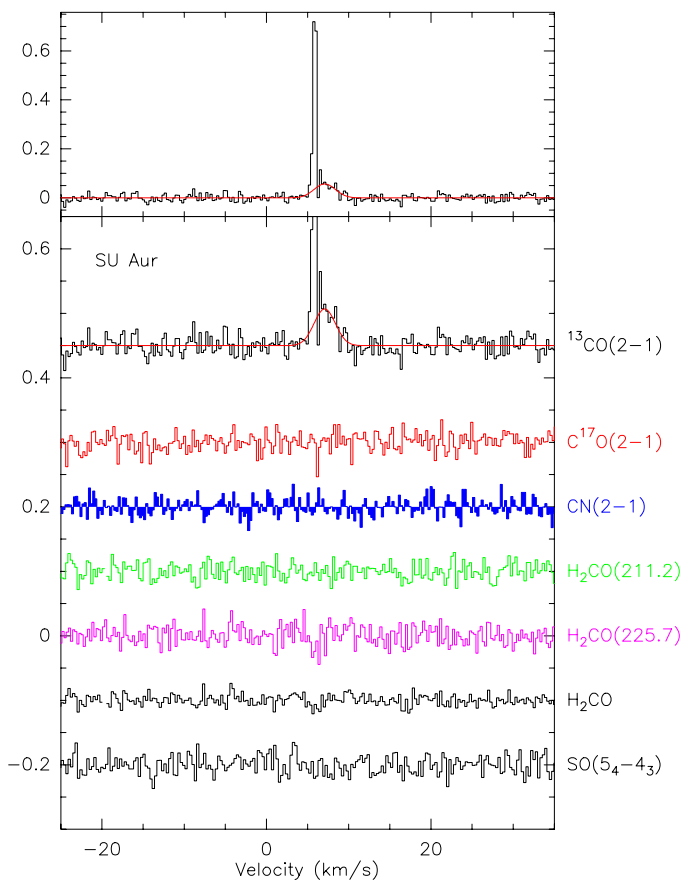


Fig. B.33. Spectra of the observed transitions towards SU Aur.

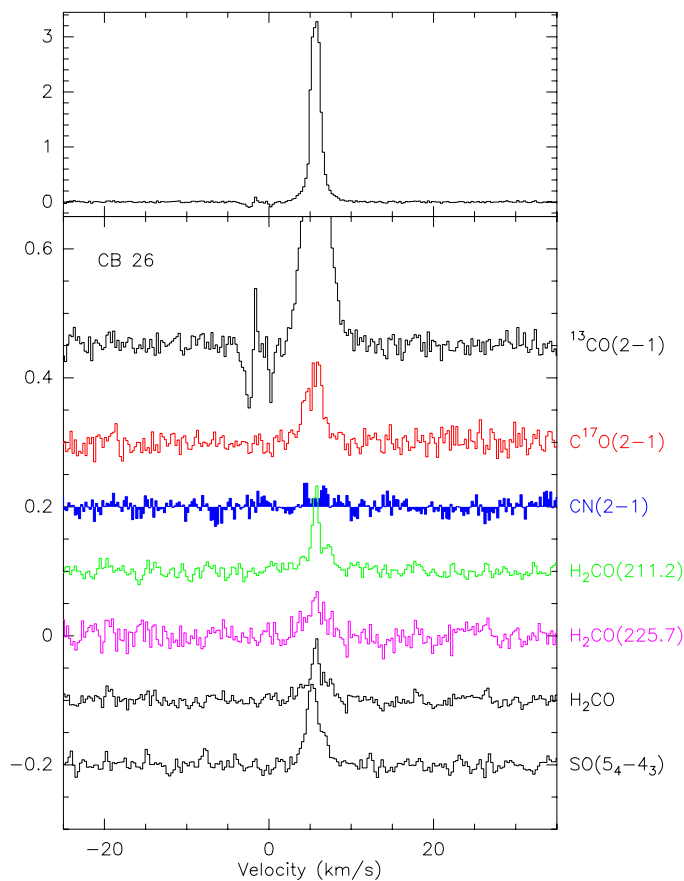


Fig. B.35. Spectra of the observed transitions towards CB 26.

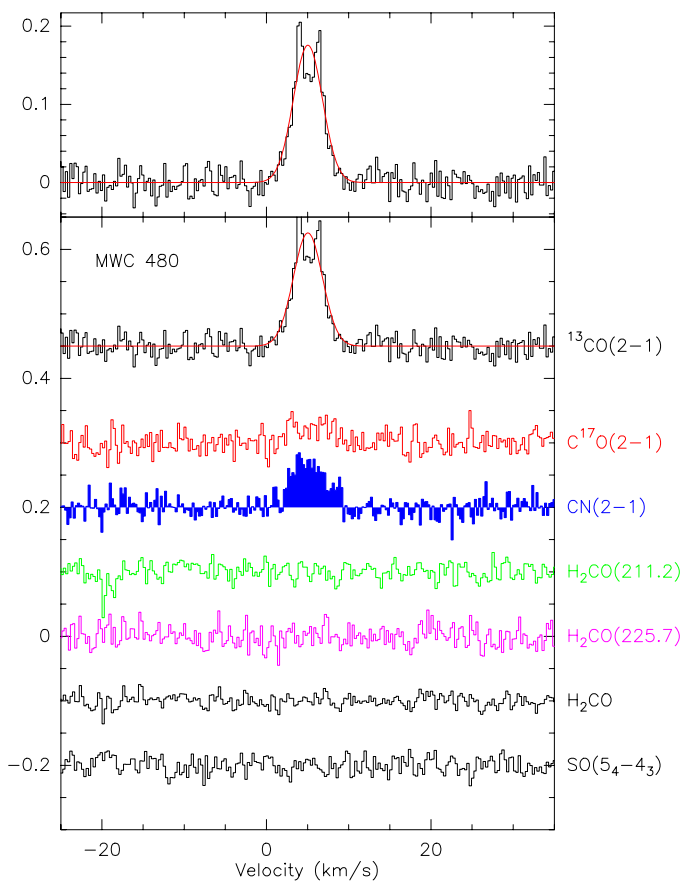


Fig. B.34. Spectra of the observed transitions towards MWC 480.

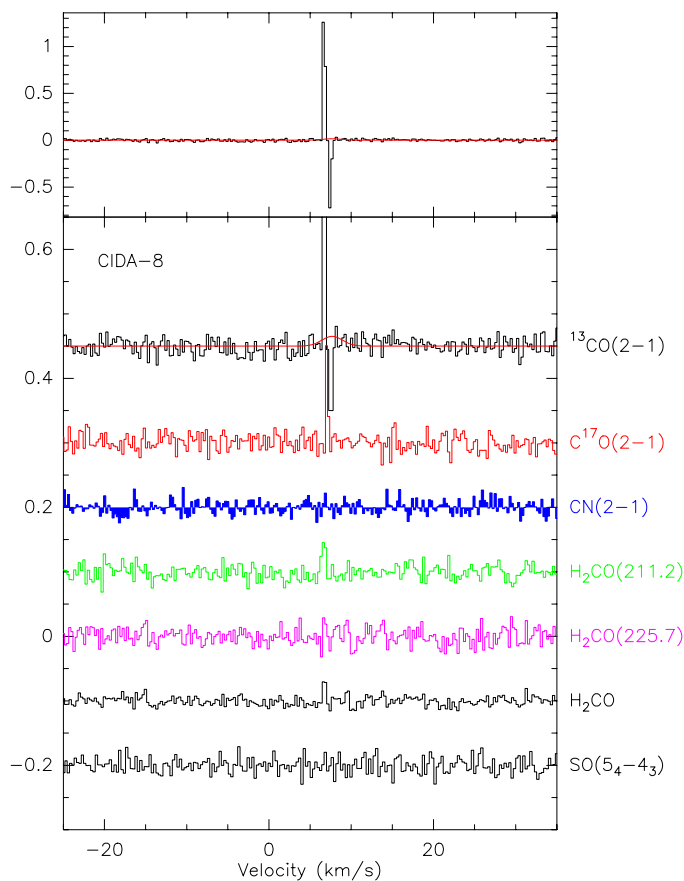


Fig. B.36. Spectra of the observed transitions towards CIDA-8.

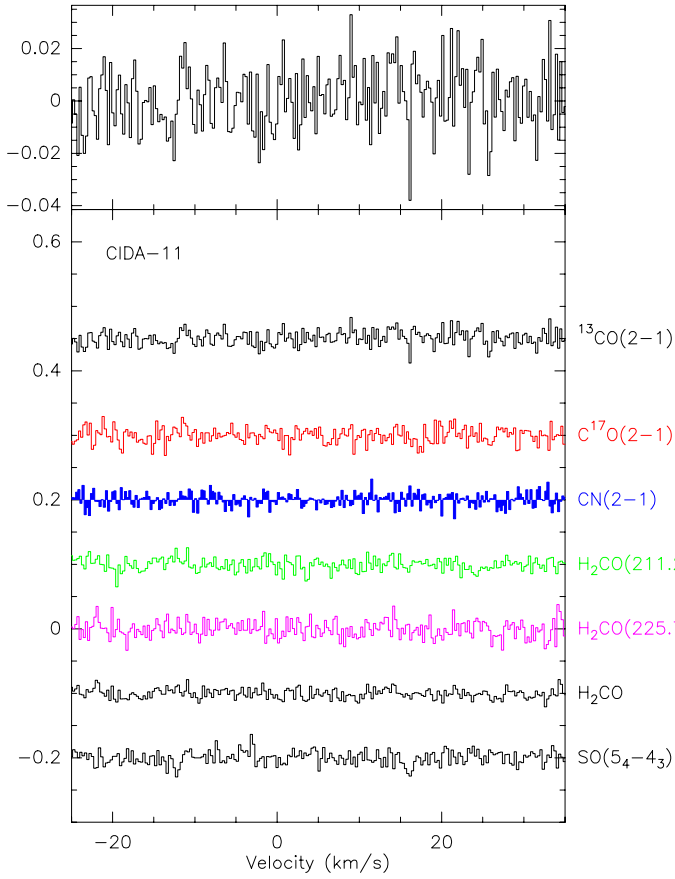


Fig. B.37. Spectra of the observed transitions towards CIDA-11.

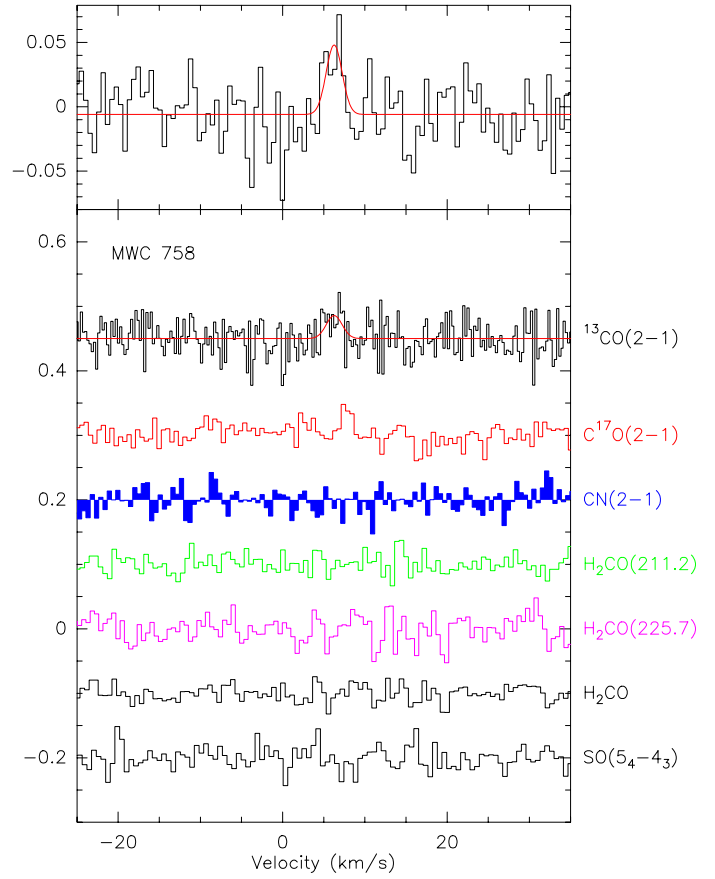


Fig. B.39. Spectra of the observed transitions towards MWC 758.

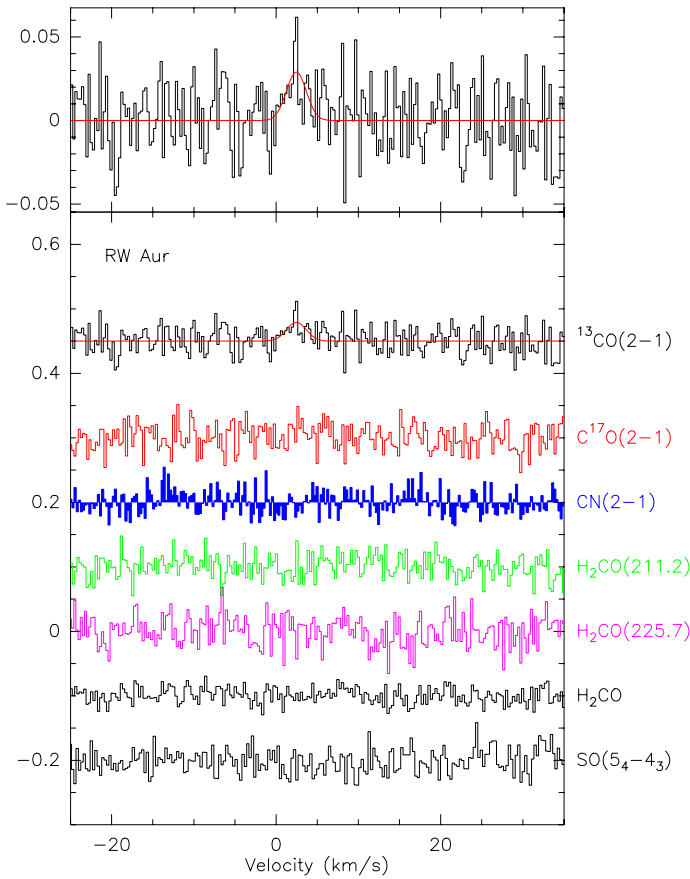


Fig. B.38. Spectra of the observed transitions towards RW Aur.

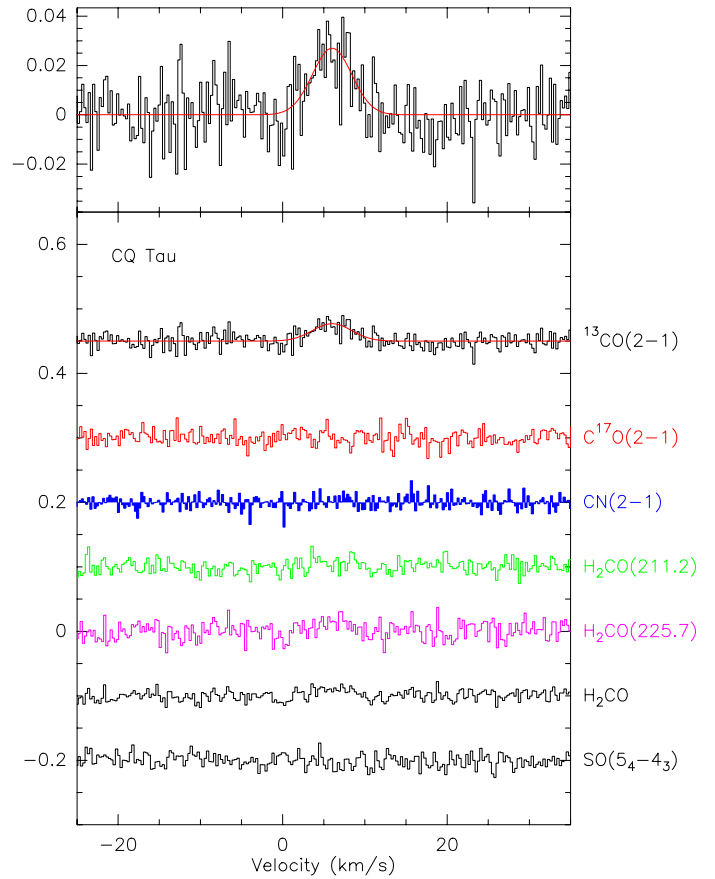


Fig. B.40. Spectra of the observed transitions towards CQ Tau.

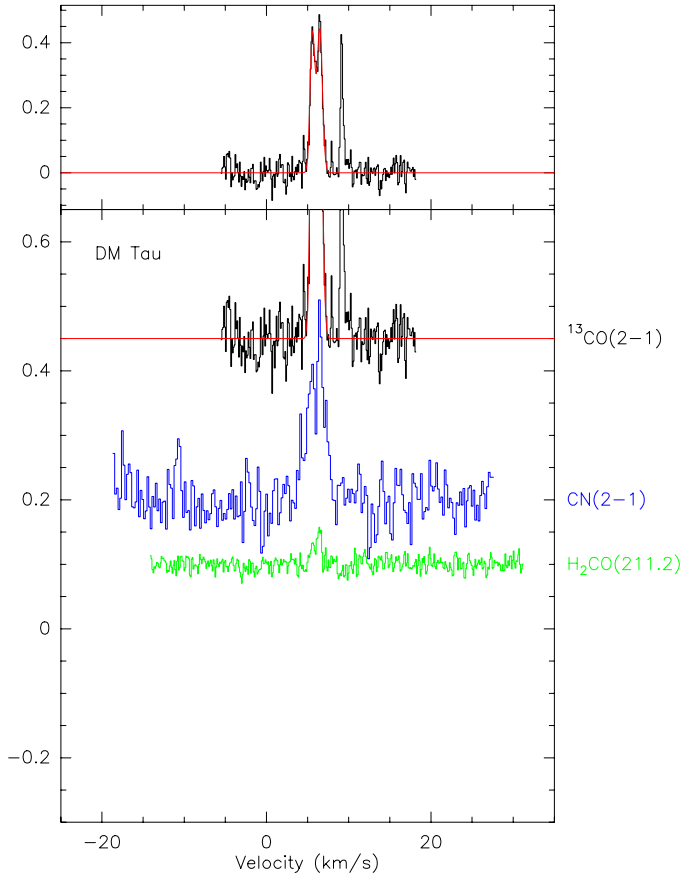


Fig. B.41. Spectra of the observed transitions towards DM Tau.

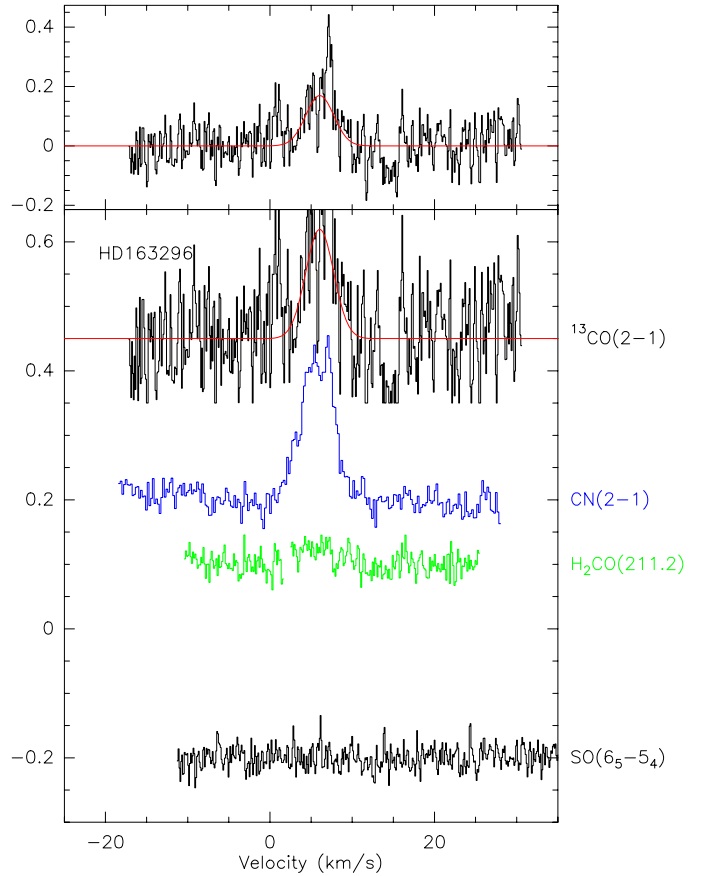


Fig. B.42. Spectra of the observed transitions towards HD 163296. The observed SO transition is not the same as in all other sources.

Appendix C: The CW Tau/CIDA-1 line of sight

CW Tau and CIDA-1, which are only separated by 1 arcmin, exhibit strong confusion in ^{13}CO , and are the only sources in which confusion in CN is obvious. Confusion is also visible in H_2CO and even C^{17}O . In addition, in the Salter et al. (2011) study, CW Tau is the source which has extended HCO^+ (3–2) emission.

In the beam-switched observations, the detection of hyperfine components of CN (Fig. C.1) suggests significant optical depth. Optically thick CN from clouds could introduce difficulties in using CN as a kinematical disk tracer, as it could absorb the disk emission. This potential problem is mitigated by several independent arguments. First, the cloud line width is small, so only a small fraction of disk kinematics will be affected. Second, CN has several hyperfine components, of very different opacities: this would help in modeling the absorption layer. Furthermore, anomalously high ($\tau \gg 1$) apparent opacities can be the result of opacity gradients in a cloud with more moderate ($\tau > 1$) average opacity, as the strongest lines saturate first. However, observations of the CW Tau line of sight in frequency switching shows a flat-topped, 2 K line of ^{13}CO , with a line width of 1.40 km s^{-1} and the same velocity than the CN signal, but no significant CN emission at a level of 50 mK (3σ). Thus, in the beam-switched observations, the detected signal probably originates from emission in one or both of the reference beams, and in the cloud, CN is most likely not much excited. Although high opacities cannot be excluded, the unusual hyperfine line ratios may also be related to weak excitation-dependent anomalies, since CN collision rates display significant dependencies on the hyperfine levels (Kalugina et al. 2012). Non negligible

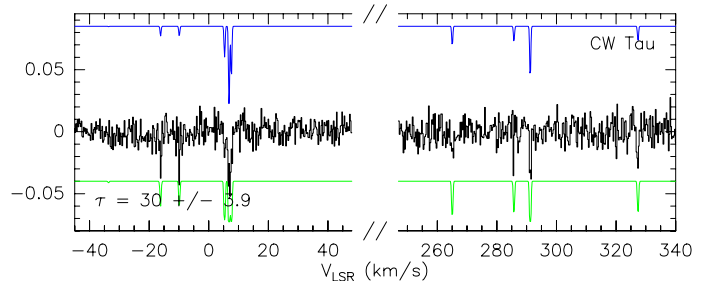


Fig. C.1. Spectra of CN towards CW Tau. The best fit with the hyperfine components is drawn below. The upper profile indicates the expected profile for an optically thin line. Detection of even weak components suggests high optical depth (~ 20 – 30). The intensity scale is T_A^* (K).

opacities, low excitation and possible hyperfine anomalies have already been reported for CN in dark clouds by Crutcher et al. (1984).

Appendix D: Formation of lines in Keplerian disks

Line formation in a Keplerian disk is strongly constrained by the velocity gradient (Horne & Marsh 1986). We use here this property to explore to what extent the detected CN lines trace the (putative) circumstellar disks. Unless the disk is seen face on, only a fraction of the disk projects at any given velocity. This fraction can be estimated with simple reasoning: we follow here the derivation presented by Guilloteau et al. (2006). r, θ being the cylindrical coordinates in the disk plane, the line of sight

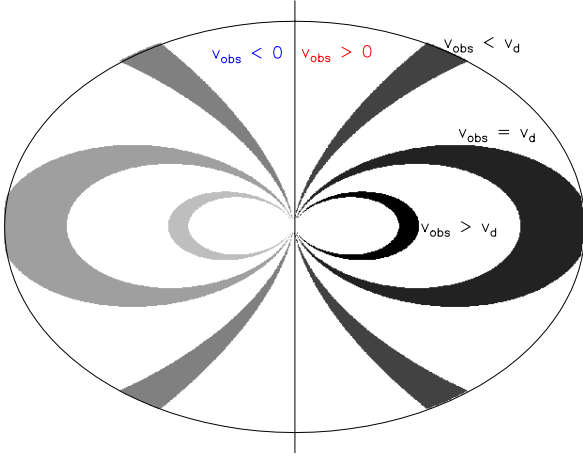


Fig. D.1. Regions of the disk which yield equal projected velocities v_{obs} . The ellipse is the projection of the disk outer edge observed with an inclination of 45° .

velocity (in the system rest frame) is

$$V_{\text{obs}}(r, \theta) = \sqrt{GM_*/r} \sin i \cos \theta. \quad (\text{D.1})$$

The locii of isovelocity are given by

$$r(\theta) = (GM_*/V_{\text{obs}}^2) \sin^2 i \cos^2 \theta \quad (\text{D.2})$$

with a finite local line width Δv (assuming rectangular line shape for simplification), the line at a given velocity V_{obs} originates from a region included between $r_i(\theta)$ and $r_s(\theta)$:

$$r_i(\theta) = \frac{GM_*}{(V_{\text{obs}} + \Delta v/2)^2} \sin^2 i \cos^2 \theta \quad (\text{D.3})$$

$$r_s(\theta) = \min \left[R_{\text{out}}, \frac{GM_*}{(V_{\text{obs}} - \Delta v/2)^2} \sin^2 i \cos^2 \theta \right]. \quad (\text{D.4})$$

Figure D.1 indicates the regions of equal projected velocities for 6 different values: $V_{\text{obs}} > v_d$, $V_{\text{obs}} = v_d$, $V_{\text{obs}} < v_d$, and their symmetric counterpart at negative velocities, where v_d :

$$v_d = \sqrt{GM_*/R_{\text{out}}} \sin i \quad (\text{D.5})$$

is the projected velocity at the outer disk radius R_{out} . Figure D.1 shows that the fraction of the disk covered by the gas at velocities $V_{\text{obs}} \approx v_d$ is of order $\Delta v/v_d$, and drops very rapidly for larger velocities. The larger area covered for $V_{\text{obs}} \approx v_d$ explains the classical double peaked line profiles emerging from Keplerian disks.

For moderately inclined ($i < 70^\circ$) disks in Keplerian rotation, the integrated line flux is given by

$$\int S_\nu dv = B_\nu(T_0)(\rho \Delta V) \pi R_{\text{out}}^2 / D^2 \cos(i) \quad (\text{D.6})$$

where T_0 is the disk temperature (assumed uniform for simplicity), ΔV the local linewidth, R_{out} the disk outer radius, D is the source distance and i the disk inclination. ρ is a factor of order of the line of sight τ_1 for optically thin lines, saturating as $\propto \log(\tau_1)$ for large optical depths (see Guilloteau & Dutrey 1998, their Fig. 4). The optically thick limit is obtained because of the Keplerian shears which, as demonstrated above, limits the maximum fraction of the disk covered at any velocity to $\delta V/v_d$. δV is the local linewidth including opacity broadening, so $\delta V \sim \log(\tau_1) \Delta V$ for large opacities.

Note that as $\tau_1 \approx \tau_p / \cos(i)$, where τ_p is the line opacity perpendicular to the disk plane, and since $\tau_p \propto \Sigma / \Delta V$, where σ is the molecule surface density, the (apparent) dependence on inclination and line width disappears for optically thin lines: the integrated line flux scales as the number of molecules.

From Eq. (D.6), we can derive the outer radius of the molecule distribution provided with have an estimate of ρ

$$R_{\text{out}} = D \left(\frac{\int S_\nu dv}{B_\nu(T_0)(\rho \Delta V) \pi \cos(i)} \right)^{1/2}. \quad (\text{D.7})$$

Equation (D.7) is valid for single lines. For molecules with hyperfine structure like CN, line blending must be accounted for. We do so in taking into account the relative weight of the hyperfine components: the integrated flux of the $J = 5/2-3/2$ fine structure group presented in Table 3 is multiplied by 0.45 to obtain the flux in the strongest hyperfine component, which then used in Eq. (D.7) to derive the outer radius. The fitted opacity, if available, is used to provide an estimate of ρ ($\rho = \tau$, τ being the sum of the opacities of all hyperfine components), which is otherwise set to 0.3.